RICE UNIVERSITY

Expansion and Electron Temperature Evolution in an Ultracold Neutral Plasma

by

Priya Gupta

A THESIS SUBMITTED
IN PARTIAL FULFILLMENT OF THE
REQUIREMENTS FOR THE DEGREE

Doctor of Philosophy

Approved, Thesis Committee:

Thomas C. Killian, Chair
Associate Professor of Physics and Astronomy

F. Barry Dunning
Sam and Helen Worden Professor of
Physics and Astronomy

Philip R. Brooks
Professor of Chemistry

Houston, Texas

May 2007

Abstract

Expansion and Electron Temperature Evolution in an Ultracold Neutral Plasma

by

Priya Gupta

This work describes the evolution of an ultracold neutral plasma as it expands freely in vacuum. It presents a comprehensive study of the electron temperature evolution under different initial conditions. Ultracold neutral plasmas are created by photoionizing laser-cooled neutral atoms in ultrahigh vacuum. The ions are typically at a temperature of $\sim 1\,\mathrm{K}$ while the electron temperature can be set from 1 - 1000 K. After photoionization, some of the highly energetic electrons escape from the cloud, leaving a net positive charge in the cloud. This creates a Coulomb well which traps the rest of the electrons, and a plasma is formed. Since the electrons have a lot of kinetic energy, they tend to leave the cloud, however, the Coulomb force from the ion pulls the electrons back into the cloud. This exerts a recoil force on the ions, and the whole plasma starts expanding radially outwards.

Since the expansion is caused by the thermal pressure of the electrons, a study of the plasma expansion unravels the complicated electron temperature evolution, under different initial conditions. Many collisional processes become significant as a plasma expands. These physical processes tend to heat or cool the ions and electrons, leading to very different kinds of evolution depending on the initial conditions of the plasma.

This work demonstrates three different regions of parameter space where the degree of significance of these physical processes is different during the ultracold neutral plasma evolution. The experimental results are verified by theoretical simulations, performed by Thomas Pohl, which untangle the complicated electron temperature evolution.

Acknowledgements

The last few years have been some of the best years of my life. It was a wise man who once said "the journey is more important than the destination"; these last few years have taught me to believe that, for I have met great people on the way. I think it is befitting to start by thanking the person who has been most instrumental in helping me not only complete this journey but also learn a lot along the way, my advisor Prof. Thomas Killian. Under his guidance, I learnt not only how to become a good researcher but also a good human being. His patience with, and compassion towards students never ceased to amaze me. I would also like to thank my committee members, Prof. Barry Dunning and Prof. Phil Brooks. The encouragement they provided helped me tremendously during the last stages of my PhD.

This PhD would have been an impossible task without the help and support of my labmates. Sarah, Sampad, Clayton, Jose, Hong, Yenny, Pascal and Dan have been a big part of my life during my stay at Rice. They have all influenced my life in some way or the other and helped me become a better person. We all come from different parts of the world and my lab was like a small version of the world.

Needless to say, my parents have a very big role in the completion, in fact, even the beginning of my PhD. Without their support and encouragement, I would not have been able to come to USA and begin my study at Rice University. My parents have always supported all my decisions and allowed me to follow my dreams. With their love and affection, I was able to overcome any difficulties in my path and reached

my destination with ease.

My brother never ceases to amaze me with his intelligence and his inability to get stressed over anything. From him, I have tried to learn how to avoid being tensed about anything, however, I am still in the early stages of that lesson. I am indebted to him for his love and support and the importance of his presence in my life is immeasurable. I also want to thank my sister whose encouraging words kept me motivated. She always made me feel strong and confident which was undeniably the key to surviving far from family while completing a task as Herculean as a PhD.

My life (and acknowledgement) is incomplete without Ben. His love and support was the most important factor in my progress towards the completion of my degree at Rice. His ability to always put a smile on my face helped me overcome any difficult situations I faced during my study. I look forward to spending the rest of my life with such a wonderful person.

There are so many more people who have made my stay at Rice one of the best times of my life. Naming them all would make a thesis in itself so I shall be content with naming just a few of them: Adria baker, Louma Ghandour, Ramsey Kamar, Sushant Dutta... a big and heartfelt thank you to all my friends.

Contents

List of Figures

Chapter 1

Introduction

1.1 Background

This thesis describes a detailed study of ultracold neutral plasma (UNP) expansion and electron temperature evolution for a wide range of initial conditions. It presents the first comprehensive study of the various physical processes that occur in an ultracold neutral plasma during its evolution. Ultracold neutral plasmas have opened up a new regime of plasma physics. The ions and electrons are at much colder temperatures than traditional plasmas. Typically the ions are at 1 K and electrons are at 1-1000 K temperatures. The low temperature pushes the UNPs into an exotic regime of plasma physics in which we can potentially observe many-body phenomena and phase transitions such as Coulomb crystallization [1]. However, many physical processes tend to increase the ion and electron kinetic energy, thus decreasing the ion-ion correlations and preventing any collective effects. One such process is plasma expansion. An unconfined UNP in vacuum, expands radially outwards due to the thermal pressure of the electrons. During the expansion, various physical processes heat the ions and electrons. A detailed study of the plasma expansion is critical to

understand the ion and electron behavior and identify these heating processes. Since the expansion is driven by the thermal energy of the electrons, a study of the electron temperature evolution is crucial in understanding and controlling the expansion. Equipped with the complete understanding of the ion and electron evolution in a UNP, a parameter space in which we can achieve strong coupling can be identified.

One of the most interesting features of UNPs is that the ions are strongly coupled. Strong coupling is achieved when the Coulomb interaction energy between particles exceeds their average kinetic energy. The Coulomb coupling parameter

$$\Gamma = \frac{e^2}{4\pi\epsilon_0 a k_B T} \tag{1.1}$$

determines the extent to which the ions and electrons are strongly coupled in a plasma, where $a = (3/4\pi n)^{1/3}$ is the Wigner Seitz radius, n is the density of the particles, e is the electronic charge and T is the temperature of the ensemble of particles. The ions in a UNP are strongly coupled, but the electrons are typically not in the strongly coupled regime after they thermalize among themselves. Strong coupling connects UNPs to plasmas that exist in dense astrophysical systems [2], matter irradiated with intense laser fields [3–6], colloidal or dusty plasmas [7, 8] and non-neutral trapped ion plasmas [9]. Strong coupling affects characteristics of a UNP on a short time scale of the order of $1\,\mu s$. It does not however, have a significant effect on the plasma expansion which happens on a tens of microsecond timescale. Regardless, equipped with the findings from this thesis, we can identify a region in UNP parameter space

where strong coupling of the ions can be achieved.

UNPs provide an ideal experimental system with excellent control over the initial conditions and a widely accessible parameter space. The study of UNPs began at NIST in Maryland where S. L. Rolston ionized a laser-cooled gas of xenon atoms to make an ultracold neutral xenon plasma [10]. Since then, many experimental groups started working with UNPs of different elements. T. C. Killian at Rice University is exploring ultracold neutral strontium plasmas [11, 12]; S. Bergeson at Brigham Young University is studying ultracold neutral calcium plasmas [13, 14]; T. F. Gallagher at University of Virginia and P. Pillet at CNRS, France are working with rubidium and cesium plasmas [15]; and G. Raithel at University of Michigan is studying rubidium ion plasmas [16].

There has been much experimental study on the evolution, and the various processes that are significant during the evolution of UNPs. A charged particle, in the presence of other charged particles, oscillates about its mean position. A study of such ion plasma oscillations in a UNP was done by Chen *et al.* [12]. They identified the initial heating of the ions due to disorder; and the damping of the ion oscillations due to density variation within the plasma. Since the electron plasma oscillations also depend on the density, Bergeson *et al.* [17] and Kulin *et al.* [18] did a study in which they used these electron oscillations to determine the evolution of the density of the plasma.

There has also been some experimental study on the various physical processes

that heat the electrons during plasma expansion. Kulin *et al.* [18] measured the terminal velocity of the ions at $t > 5 - 20\,\mu s$ and related it to the initial electron temperature of the plasma. Roberts *et al.* [19] observed the response of the plasma to an electric field using a charged particle detection mechanism to study the electron temperature evolution. They had to make certain assumptions to calibrate their probe, thereby introducing uncertainties in their results.

UNPs can also be created by exciting a dense Rydberg gas which spontaneously evolves into a plasma due to collisional processes. Several groups have done experimental studies of UNPs created from a dense Rydberg gas [15, 20–22] in which they explored the exact mechanism of ionization of the atoms to form a plasma. A clear and detailed understanding of the process is still unknown.

UNPs have been studied by theorists as well. Theoretical and numerical simulations of UNPs are challenging since the ions and electrons evolve on a different time scale. The ions, being heavier, evolve on a microsecond time scale, while the electrons thermalize within a few nanoseconds. The initial ion equilibration has been a topic of much interest. The ions heat up rapidly due to ion-ion correlations [23–27]. The electron temperature evolution also makes an interesting study since the evolution is complicated by many competing processes which heat and cool the electrons [26, 28–32]. Mazevet *et al.* [33] did the first large-scale simulations of an ultracold neutral plasma and studied the various processes that are significant during plasma evolution. They reproduced many of the results from the first experimental study

on UNPs [10, 18]. Kuzmin *et al.* [28] simulated the evolution of ultracold plasmas with special emphasis on the electron temperature evolution. They reported that the various electron heating effects prevent electron-electron correlations from developing in an expanding ultracold plasma. Robicheaux *et al.* [26, 27] studied in detail, the effect of recombination on the electron temperature evolution during plasma expansion. They probed certain plasma processes such as ion acoustic waves, density spike formation, and electron evaporation; and simulated the evolution of a cold Rydberg gas into a plasma. Pohl *et al.* [34] did a theoretical study of the Rydberg to plasma transition as well. They suggest that the ionization process begins with some seed charges produced by black-body radiation which then collide with the Rydberg atoms to initiate an avalanche-like ionization process.

With no external forces, a UNP expands radially outwards due to the thermal pressure of the electrons. Under conditions of high initial electron energy and low plasma density, UNP expansion is similar to plasmas that are created by an intense laser field irradiating a solid [35, 36], thin film target [37–45], rare gas cluster [46] and gas jets [47, 48]. These hot plasmas have much higher densities than UNPs, and the ions and electrons are at MeV temperatures. High densities and temperatures makes it challenging to observe the plasma dynamics which happen on the scale of the inverse plasma frequency, $\omega_p^{-1} = \sqrt{m\epsilon_0/(e^2 n)}$, which is on the order of attoseconds for electrons and femtoseconds for ions.

UNPs have an edge over these hot plasmas. The advantage of UNPs over the

traditional laser-produced plasmas is that due to their much colder temperature and lower density, the ions and electrons expand on a time scale which is easily observable using optical probes [11] and charged-particle detection techniques [18]. UNPs, therefore, provide a simple and clean system to study and test basic plasma theory and to understand the plasmas that exist in certain astrophysical systems.

This thesis focusses on the UNP expansion and electron temperature evolution as the plasma expands. The remainder of Chapter 1 discusses how UNPs can be created from a gas of laser-cooled and trapped atoms. Chapter 2 describes the various physical processes in a UNP. Chapter 3 discusses the theory behind plasma expansion, the detection methods and the experimental concerns in studying UNP expansion. The detection method used in this study, absorption spectroscopy, is a very powerful technique and it was developed in this laboratory. Chapter 4 focusses on the self-similar Gaussian expansion which connects UNPs to other laser-produced hot plasmas. Chapter 5 discusses the electron temperature evolution in a UNP for different initial conditions. Chapter 6 summarizes the conclusions from the thesis and suggests future work.

1.2 Creation of a UNP

UNPs were first created at NIST by Killian *et al.* [10]. They laser cooled and trapped xenon atoms and photoionized them just above the ionization threshold to create ions at 100 μK and electrons at 100 mK temperatures. The density of the UNP

was on the order of $10^{15}\,m^{-3}$. Robinson *et al.* [15] took a different approach and created UNPs of cesium as well as rubidium atoms by exciting them just below the threshold. The cold Rydberg atoms spontaneously evolved into a plasma. This thesis focusses on plasma created by exciting the electron above the ionization threshold; however, a short discussion on plasma created by a cold Rydberg gas is also presented.

1.2.1 Laser cooling and trapping of Strontium

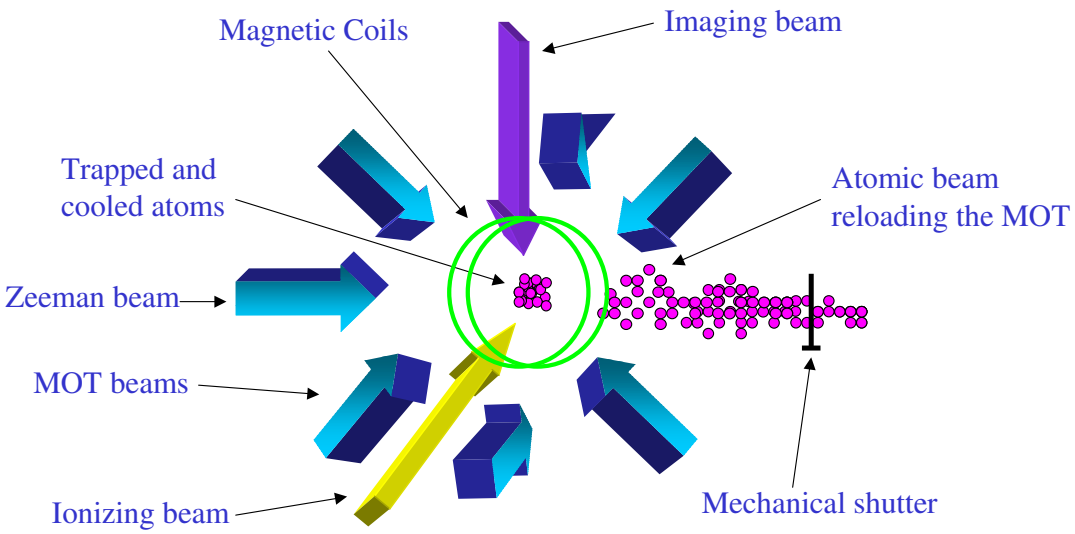

Figure 1.1: Experimental set up for laser cooling and trapping Sr atoms. The atoms are cooled to millikelvin temperatures in a MOT with the help of a counter propagating Zeeman beam, six MOT beams and magnetic coils. The mechanical shutter blocks the atomic beam while the ionizing beam photoionizes the laser-cooled Sr atoms to create a UNP.

Ultracold neutral Strontium plasmas are produced by photoionizing laser-cooled and trapped neutral ^{88}Sr atoms in a magneto-optical trap (MOT) [49] as shown in Fig. 1.1. A MOT consists of six laser cooling beams (MOT beams) and magnetic fields. The Sr atom has a resonant transition from $^1S_0$ to $^1P_1$ at 461 nm as shown in Fig. 1.2. This transition is used for laser cooling the atoms. The linewidth of the transition is 32 MHz and the saturation intensity, $I_{sat} = 45\, mW/cm^2$. To generate 461 nm light, the 922 nm output of a Ti:Sapph laser is frequency doubled through second harmonic generation. The details of the MOT are described in [50].

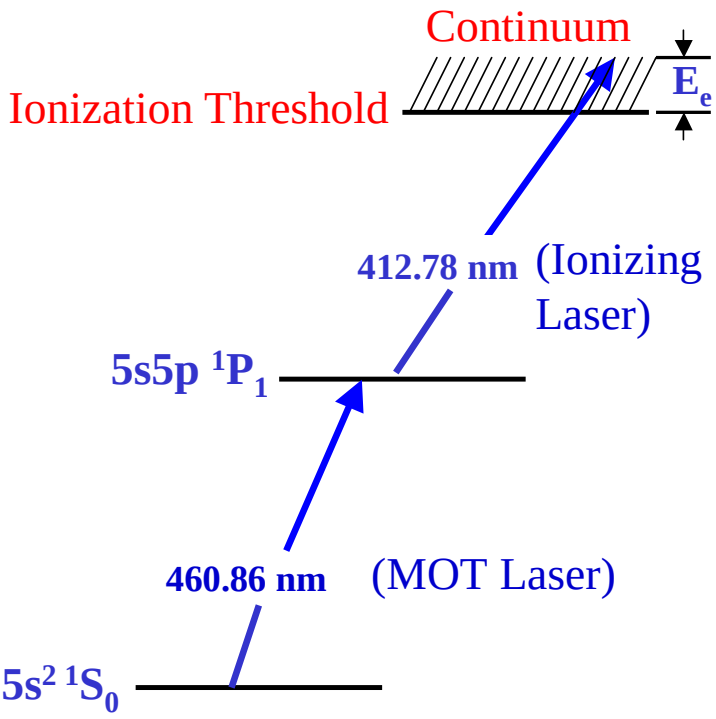

Figure 1.2: Energy Levels of Strontium. The photoionization of Sr to create a UNP is a two photon process. The MOT laser excites the atoms to the $^1P_1$ state and a pulsed dye laser beam ionizes it from the excited state. The extra energy (E_e) in the ionizing photon, above the ionization threshold, is taken up by the electrons due to their light mass.

The Sr atoms, heated to ∼800 K, are slowed down to ∼2 K with the help of a Zee-

man cooling beam and magnetic fields. The Zeeman beam is detuned by ∼500 MHz from atomic resonance. The magnetic fields produce a Zeeman shift in the atom energy levels to bring the Zeeman beam on resonance with the atoms. Once the atoms are slowed enough to be able to absorb the MOT beam, the MOT cooling beams, along with magnetic fields produced by anti-Helmholtz coils, cool the atoms down to a few millikelvin temperature. As many as 10^9 atoms can be trapped in the MOT. The atom cloud is spherically symmetric with a Gaussian density distribution $n(r) = n_0 e^{-r^2/2\sigma^2}$, where n_0 is the peak density and σ is the rms width of the cloud. The density of the atom cloud is on the order of $10^{16}\, m^{-3}$. The typical initial size of the cloud (σ_0) is on the order of 1 mm.

1.2.2 Photoionization

The laser-cooled and trapped Strontium atoms are photoionized by a pulsed dye laser (PDL) to create a UNP. A schematic of the PDL is shown in Fig. 1.3. The PDL is pumped by 355 nm light from a pulsed Nd:YAG laser. The Nd:YAG laser has an output of 240 mJ with a repetition rate of 10 Hz and a pulse width of 10 ns. The PDL uses "Exalite 411" dye from Exciton, Inc mixed in p-dioxane and outputs 40 mJ of light tunable from 395-420 nm. Due to various optical elements in the path of the beam, only 50% of the photoionizing beam power reaches the atoms. The beam is 1 cm in diameter with an instantaneous intensity of $\sim 350\, kW/cm^2$. For more details on the pulsed dye laser, please refer to my Master's thesis [51].

The laser-cooled atoms are photoionized from the excited $^1P_1$ state of the Sr atom

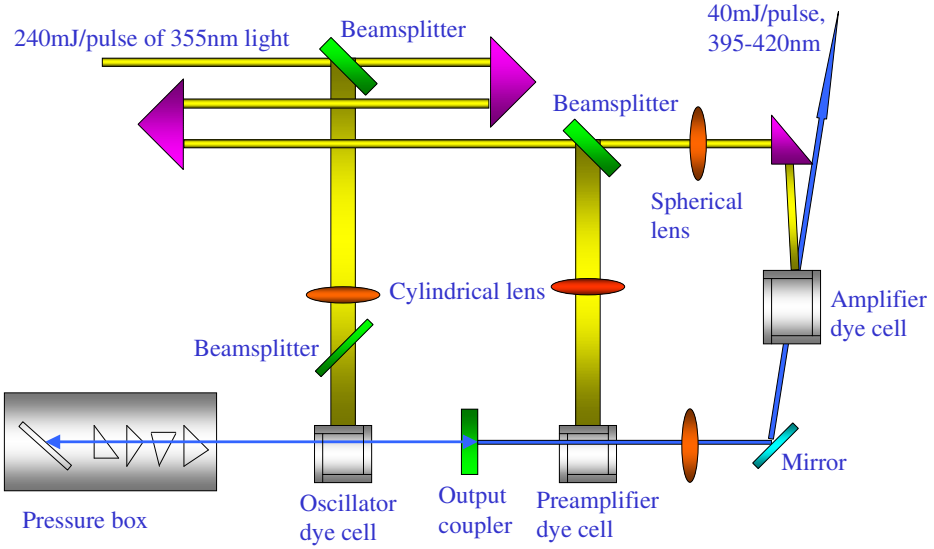

Figure 1.3: Dye Laser Layout. The pulsed dye laser which generates the photoionizing beam is pumped by the 355 nm output of a pulsed Nd:YAG laser with 10 Hz repetition rate. With an input of 240 mJ/pulse of pump power, the PDL generates ~40 mJ/pulse of light tunable from 395 - 420 nm. The oscillator and preamplifier stage dye cells of the PDL are transversely pumped and the amplifier stage is longitudinally pumped to improve beam quality.

as shown in Fig. 1.2. The ionization threshold from the excited state is at 412.777 nm. The MOT lasers are turned off before the dye laser pulse ionizes the atoms; so all the atoms de-excite to the ground state. A high intensity, $\sim 30\,mW/cm^2$, optical pumping beam at 461 nm is used to excite $\sim 25\%$ of the atoms to the excited state just before the PDL beam ionizes them. Fig. 1.4 shows the timing sequence for creation of the Strontium plasma.

The absolute photoionization cross-section of Sr in the near-threshold-ionization region is $\beta \sim 300 * 10^{-18}\,cm^2$ [52]. The fraction of the excited state atoms ($N_{^1P_1}$) photoionized is given by

$$\frac{N_i}{N_{^1P_1}} = 1 - exp(-\beta\phi_{ph}) \tag{1.2}$$

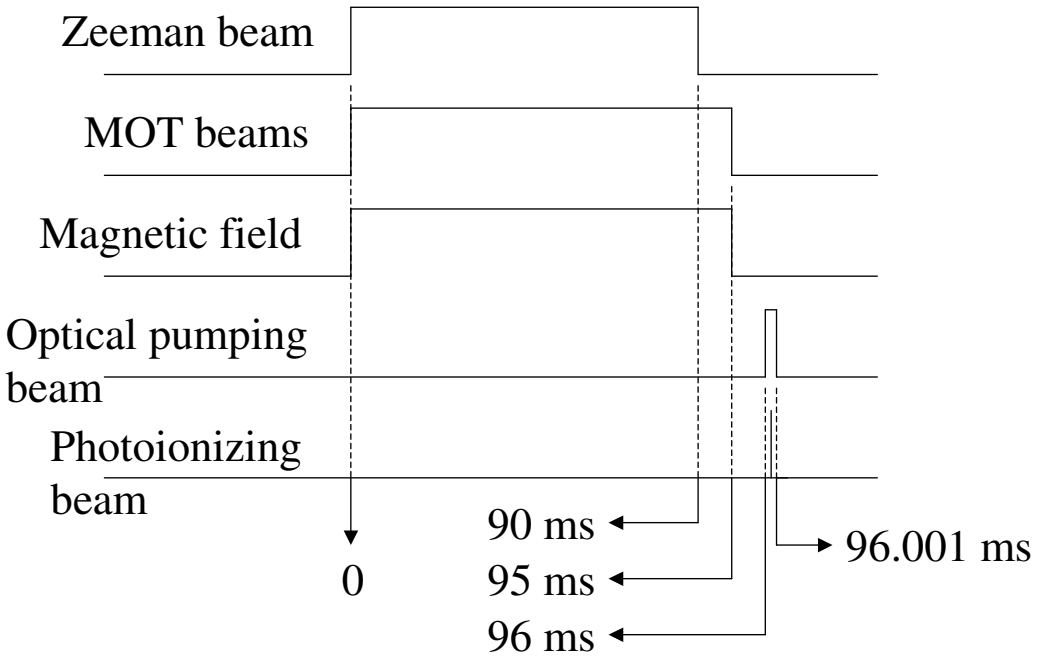

Figure 1.4: The timing sequence for UNP creation. The Zeeman and MOT beams, along with the magnetic field, cool and trap neutral Sr atoms and then they are turned off. A delay is introduced to allow the MOT to equilibrate and also obtain the desired cloud size and density. Then an optical pumping beam excites the atoms to the excited state and the photoionizing beam, which overlaps with the time of arrival of the optical pumping beam, ionizes these excited atoms.

where N_i is the number of ions and ϕ_{ph} is the photons per unit area in the photoionizing beam. With $20\,mJ/cm^2$, ideally more than 95% of the excited state atoms can be photoionized. In practice, though, the dye laser pulse typically ionizes only about 25% of the ground state atoms in the system because the optical pumping beam excites only $\sim 25\%$ of the atoms to the excited $^1P_1$ state. The ionizing laser has enough power to ionize the excited state atoms with $\sim 100\%$ efficiency.

1.2.3 UNP creation

Strontium UNPs are created by photoionizing laser-cooled atoms. The photoionization laser provides enough energy to excite the electron into the continuum, thus creating a cloud of free ions and electrons. The ionizing laser can be tuned to provide more energy than is required just to photoionize the atom. Due to the huge mass difference between the ions and electrons, the electrons take up the extra energy (E_e) above the ionization threshold in the ionizing photon. This transfer of energy to the electrons leaves the ions at the same temperature as the laser-cooled atoms. Therefore immediately after photoionization, the ions created are at millikelvin temperatures. Since the initial electron energy is set by the tunable laser, it can be as low as the linewidth of the photoionizing laser, which is $\sim 1\,\mathrm{K}$. Typically the initial energy of the electrons in this study of UNPs is set from 1-100 K. The ions and electrons are not in thermal equilibrium immediately after creation. Various process heat the two species before they reach local equilibrium. A discussion on these processes will be presented later in the text.

Just after photoionization, some of the highly energetic electrons escape from the edge of the cloud. This loss of electrons leaves a net positive charge in the cloud which creates a Coulomb potential energy well that traps $> 95\%$ of the electrons [10]. In order to trap any electrons, the Coulomb well needs to be deeper than the kinetic energy of the electrons. The threshold number of ions, N^*, required to trap electrons

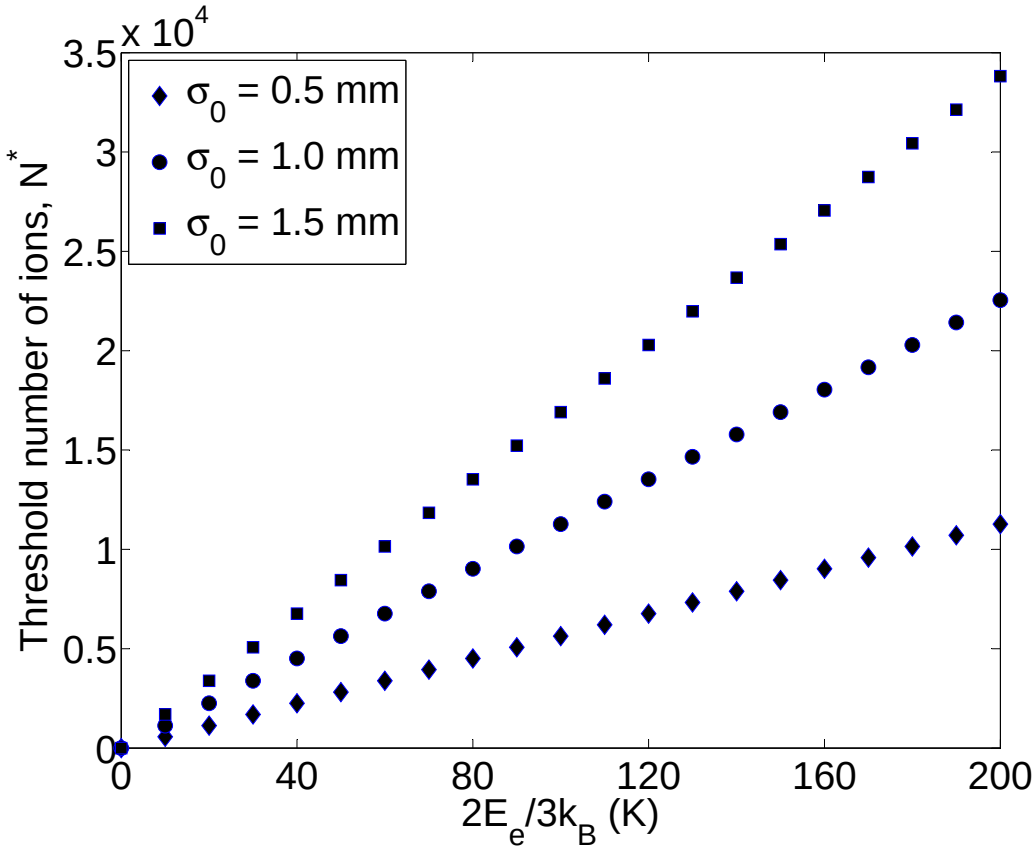

Figure 1.5: Threshold number of ions. The number of ions required to trap the electrons in a Coulomb well to create a UNP increases with increasing electron temperature and cloud size. Typically, there are ∼50 million ions in the plasma cloud with a 1 mm cloud size, so we are well above the threshold.

to form a plasma can be calculated using [10],

$$E_e = \frac{N^* e^2}{4\pi\epsilon_0 \sigma}\sqrt{\frac{2}{\pi}} \tag{1.3}$$

Fig. 1.5 shows the threshold number of ions as a function of initial electron energy for different initial plasma cloud sizes. A larger fraction of electrons are trapped when the UNP cloud contains a greater number of ions and electrons initially, lower initial electron energy and smaller cloud size. The electrons escape mostly from the edge of

the cloud; hence, the core of the plasma cloud is essentially neutral. The plasma cloud has the same density distribution as the neutral atoms; hence, it has a spherically symmetric Gaussian profile.

The threshold condition in Eq. 1.3 is equivalent to $\lambda_D = \sigma$ where $\lambda_D = \sqrt{\epsilon_0 k_B T_e / e^2 n_e}$ is the Debye screening length, where $T_e = 2E_e/3k_B$, and n_e is the electron density. The Debye screening length is the characteristic length scale in which the Coulomb force of an ion is screened by the surrounding electrons. Therefore, for a system to be considered a plasma, $\sigma >> \lambda_D$. In this system, $\lambda_D = 1 - 20\,\mu m$ while σ is on the order of 1 mm, so the requirement for a plasma to exist is fulfilled.

1.2.4 Spontaneous ionization of a Rydberg gas

UNPs can also be created by exciting a dense cloud of Rydberg atoms which spontaneously evolves into a plasma. Robinson *et al.* [15] did some of the initial experiments on creating a plasma from a Rydberg gas. A clear understanding of the processes that cause spontaneous ionization of the Rydberg atoms is not established. However, Li *et al.* [22] and Amthor *et al.* [53] demonstrate that Rydberg-Rydberg collisions initiate plasma formation and that the electrons thus created also collide with the atoms resulting in their ionization. This doubled ionization process results in an avalanche-like conversion. Pohl *et al.* [34] used molecular-dynamics simulations to describe the process of formation of a UNP from a highly excited Rydberg gas. An interesting feature of a plasma created from a dense Rydberg gas is that the plasma expands non-adiabatically. This type of expansion will be discussed in section 5.3.

Chapter 2

Physical Processes in UNP

To facilitate understanding, the UNP evolution can be divided into three phases. The first phase occurs when the electrons thermalize among themselves in a few nanoseconds. Then the ions reach local thermal equilibrium on a timescale of the inverse ion plasma oscillation frequency. Third, the plasma expands on a microsecond timescale. Many processes either heat or cool the ions and electrons during the evolution. This chapter gives a brief description of all these significant processes and is divided into two sections: the first section gives an overview of the processes which are significant for ion temperature evolution and the second describes in detail the processes important for the electron temperature evolution.

2.1 Ion temperature evolution

The ions in strontium UNPs are created at millikelvin temperatures. Although they have a spherically symmetric Gaussian distribution, they are located randomly with respect to the neighboring ions. Due to their disorderly state, they undergo disorder-induced heating and kinetic energy oscillations. A detailed discussion of

these physical processes can be found in Sampad Laha's dissertation [54]. A brief discussion of the physical processes that the ions undergo in the first few microseconds after plasma creation is presented in the following section.

2.1.1 Disorder-induced heating

As the name suggests, disorder-induced heating (DIH) stems from the fact that the plasma is created in an uncorrelated state. Immediately after photoionization, the ions are not in thermal equilibrium. Due to their heavy mass, they are at the same temperature as the laser-cooled atoms and have little kinetic energy. However, they are spatially uncorrelated and so possess a lot of potential energy. As the ion correlations develop, their potential energy is converted into (thermal) kinetic energy leading to equilibration. This increase in kinetic energy corresponds to a rapid increase in the ion temperature, as is evident in Fig. 2.1.

The ion heating happens on a time scale of the inverse ionic plasma frequency, $\omega_{p,i}^{-1} = \sqrt{m_i \epsilon_0/(n_i e^2)}$. For Sr^+ ions with $n_i = 10^{15}\, m^{-3}$, $\omega_{p,i}^{-1} \sim 200\, ns$ which is the timescale over which the rapid ion heating is observed. Assuming complete initial disorder, and incorporating the electron screening effects (section 2.1.2), the ions would equilibrate at a temperature of [23]

$$T_i = \frac{2}{3k_B} U_a \mid \tilde{U} + \frac{\kappa}{2} \mid, \tag{2.1}$$

where $\kappa = a/\lambda_D$, $U_a = e^2/(4\pi\epsilon_0 a)$ is the Coulomb interaction energy between neigh-

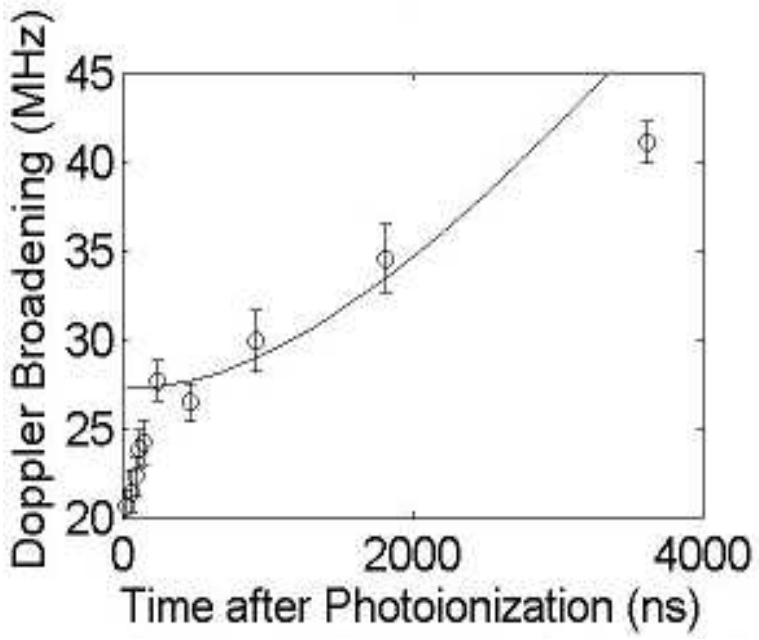

Figure 2.1: Disorder-induced Heating. The ions are created in a disordered state and have high potential energy. They develop correlations and reach their lowest potential energy state, thus increasing their kinetic energy. This increase is reflected in the rapid increase in the linewidth of the ion spectrum in the first few hundred nanoseconds in the figure. After the ions reach local thermal equilibrium, the pressure from the electrons causes a slow increase in the linewidth due to expansion. The solid line is a preliminary fit to the increase in Doppler broadening due to expansion. This figure is taken from [11].

boring ions with Wigner-Seitz radius $a = (3/4\pi n_i)^{1/3}$ and $\tilde{U}$ is the excess potential energy per ion [55] in units of U_a. $\tilde{U}$ itself depends on T_i, so an iterative numerical method is required to solve Eq. 2.1 as used by Chen *et al.* [12]. Usually the ions heat up to $\sim$1 K due to disorder-induced heating which gives a Coulomb coupling parameter, Γ_i, in the range of 2 - 6 for the typical range of initial peak plasma densities. Therefore, although the ions heat up rapidly due to disorder-induced heating, they still border the strongly coupled regime [11, 12]. Note: typically a plasma is called strongly coupled when $\Gamma >> 1$. Pohl *et al.* [56] show that the ion-ion correlations do not have a significant effect on the electron temperature evolution, and on the

macroscopic plasma expansion dynamics. Hence, we can use the plasma expansion theories that have been developed for a weakly coupled system (see section 3.2.1), to explain the behavior of UNP expansion.

2.1.2 Electron screening

The electrons in a UNP screen the effects of ion-ion interactions. The effects of electron screening [23] are quantified by $\kappa/2$ in the factor $\mid \tilde{U} + \kappa/2 \mid$ in Eq. 2.1. When the electrons shield the ion-ion interactions the coupling between the ions is represented by an effective coupling parameter $\Gamma_i^* = \Gamma_i^{-\kappa}$ [28, 57]. A higher density of electrons or a colder electron temperature tends to screen the ions more effectively and leads to a smaller Debye length. The screening decreases the potential energy of the ions in the initial system, resulting in a lower equilibration temperature as compared to a system in which there is no screening.

2.1.3 Kinetic energy oscillations

The ion temperature undergoes damped oscillations [12] after the disorder-induced heating phase. The ion temperature oscillates because the ions do not move to their lowest potential energy state in one step. They overshoot the lowest potential energy state and oscillate in a harmonic well with an exchange between the potential and kinetic energy until they settle at the bottom of the potential well. The oscillations happen at a frequency of $2\omega_{p,i}$.

The variation of density in cloud causes the ions to oscillate at different frequen-

cies. The inner region has a higher density, resulting in a higher plasma oscillation frequency; similarly, the outer region has a lower plasma oscillation frequency. Hence, averaging over the entire cloud dephases the oscillations because of the variation in $\omega_{p,i}$. However, the oscillations are clearly visible through an annular analysis of the system [12].

2.2 Electron heating and cooling mechanisms

A plasma expands due to the thermal pressure of the electrons. During the expansion, the thermal energy of the electrons is converted into the expansion energy of the ions. At any instant of time during the plasma expansion, the rate of expansion depends on the electron temperature until essentially all the electron thermal energy is transferred and the ions reach a terminal velocity. Hence, the evolution of electron temperature is critical in the understanding of UNP expansion. As the plasma evolves, apart from the adiabatic cooling of the electrons due to the expansion, the following processes heat or cool the electrons in addition to the energy provided by the ionizing photon:

1. Threshold lowering (TL)
2. Disorder-induced heating (DIH)
3. Electron thermalization
4. Dielectronic recombination + Radiative recombination
5. Three-body recombination (TBR)

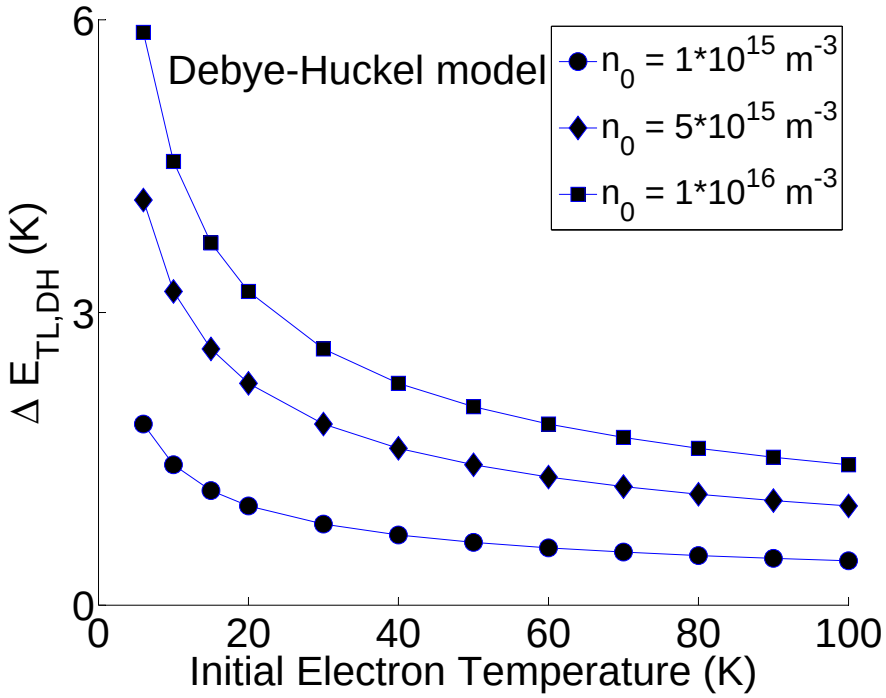

Figure 2.2: Threshold Lowering (TL). During photoionization, the electrons heat up by a few kelvin due to the TL effect. The figure shows the dependence of the TL effect on electron temperature for three different plasma densities. TL effect depends strongly on the electron temperature for colder temperatures <20 K. At higher electron temperatures, the heat from the TL effect becomes less significant in comparison to the initial electron temperature set by the ionizing photon energy.

6. Rydberg-electron collisions (R-e)

7. Radiative decay of Rydberg atoms (RD)

8. Equilibration (EQ).

A detailed explanation of each of these processes is presented in this section.

2.2.1 Threshold lowering

The photoionization pulse is 10 ns long. The ions created in the first few nanoseconds of the 10 ns long photoionizing pulse lower the ionization threshold of the neutral

atoms such that the electrons created by the rest of the ionizing pulse have greater kinetic energy. This shift occurs because the fields generated by the ions overlap with each other and produce a repulsive potential which can change the ionization threshold of the neutral atoms. This is the threshold lowering effect [30, 33, 58, 59], which, for electron Coulomb coupling parameter $\Gamma_e \leq 0.5$, is given by the Debye-Huckel model [60]:

$$\Delta E_{TL,DH} = \sqrt{3}\, T_e \Gamma_e^{3/2}. \tag{2.2}$$

This model is applicable to the plasma in this study since typically the initial electron temperatures are set at $> 10\,K$ and so $\Gamma_e < 0.5$. Fig. 2.2 shows the heating due to threshold lowering as a function of initial electron temperature for different initial plasma density. A strong dependence of ΔE_{TL} on T_e is evident in the figure. For $\Gamma_e > 0.5$, TL is given by the Stewart-Pyatt model [58]:

$$\Delta E_{TL,SP} = \frac{e^2}{a k_B} [2\Gamma_e]^{-1} [(1 + 3^{3/2}(\Gamma_e)^{3/2})^{2/3} - 1]. \tag{2.3}$$

2.2.2 Disorder-induced heating

As explained in section 2.1.1, the ions heat up rapidly after photoionization due to DIH. The electrons develop correlations among themselves and undergo DIH as well, which heats them typically by a few kelvin. The correlations develop on inverse electron plasma frequency, $\omega_{p,e}^{-1}$, time scale which is on the order of a few nanoseconds. Kuzmin *et al.* [28] show that after photoionization, correlations develop in electrons

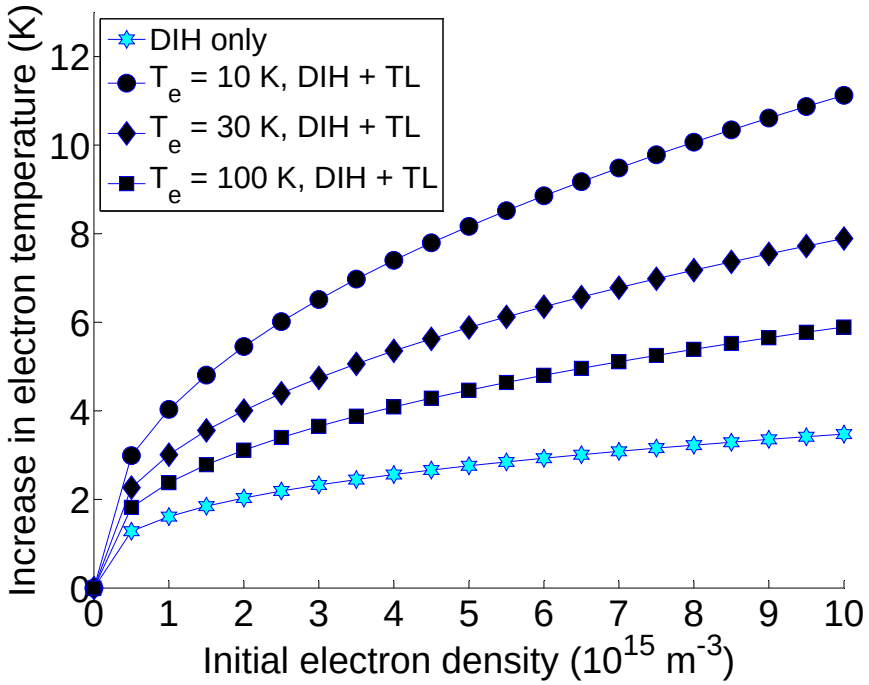

Figure 2.3: Disorder-induced heating and threshold lowering. The curve with the star symbols in the figure shows the heating of the electrons at different densities due to disorder-induced heating. The rest of the curves show an upper limit on the total heat ($\Delta E_{TL} + \Delta E_{DIH}$) given to the electrons due to DIH and TL effects at different densities for different initial electron temperatures.

which increases their kinetic energy until the Coulomb coupling parameter, $\Gamma_e \sim 1$, when further development of correlation ceases. Hence, the heating due to these correlations can be estimated using

$$\Delta E_{DIH} = \frac{e^2}{4\pi\epsilon_0 a k_B}. \tag{2.4}$$

which implies that the electrons heat up until the Coulomb coupling parameter $\Gamma_e = 1$. While the electrons can be created with low kinetic energy such that they are strongly coupled, the rapid increase in the electron kinetic energy due to TL and DIH pushes

the electrons out of the strong coupling regime. It has been suggested [61] that the processes of DIH and TL are not completely independent of each other. The two effects overlap in the first few nanoseconds. Hence, the total heat provided by the two processes ($\Delta E_{DIH} + \Delta E_{TL}$) might be an overestimation of the actual total energy that heats the electrons. This is an open question, but the sum provides a good upper limit on the total increase in the electron temperature due to the two physical effects. Fig. 2.3 shows the increase in electron temperature due to DIH only and also due to the combined effects of DIH and TL for a typical set of plasma parameters.

2.2.3 Electron thermalization

Following the effects of TL and DIH, the electrons thermalize among themselves within a few nanoseconds. Schmidt [62] and Robicheaux *et al.* [27] show that the thermalization time for electrons is given by

$$\tau_{ee} \sim \frac{1.2 * 10^{-6} s^4 m^{-6} v_e^3}{n_e ln(\Lambda)}, \tag{2.5}$$

where v_e is the electron velocity and $\Lambda = 4\pi\epsilon_0.3k_BT_e\lambda_D/e^2$. For $T_e = 40\,\mathrm{K}$ and $n_e = 10^{15}\,m^{-3}$, $\tau_{ee} \sim 20\,\mathrm{ns}$. After thermalization, they can be described with a Maxwell-Boltzmann distribution and a well-defined local temperature [26, 56].

2.2.4 Dielectronic recombination + Radiative recombination

The dominant recombination processes in a plasma at temperatures on the order of 1000 K or more are radiative recombination (RR), dielectronic recombination (DR) and three body recombination (TBR) [63]. RR [64] refers to the process in which an electron is captured and a photon is released. It is dominant at densities below $10^{20}\, m^{-3}$. DR [63] is similar to RR except that an intermediate excited electronic state is formed before radiative decay occurs.

2.2.5 Three-body recombination

TBR [65] refers to the process in which an ion and electron recombine to form highly excited Rydberg atoms and the energy released in this process is taken up by a second electron which conserves the energy and momentum. Hence, this process heats the electrons in the plasma. The TBR rate varies with electron temperature as $T_e^{-9/2}$. Such strong dependence on electron temperature makes TBR the dominant recombination mechanism in UNPs [66].

The rate of TBR, in units of number of recombination events in the whole cloud per second, is given by [26] as

$$R = \frac{e}{k_B T_e} q^7 2.8 \times 10^{-42} \frac{m^6}{s} \int n_e^2(r) n_i(r) 4\pi r^2 dr, \tag{2.6}$$

where $q = \sqrt{13.6eV/2k_BT_e}$ is the characteristic principal quantum number for recombination. The maximum principal quantum number for recombination increases

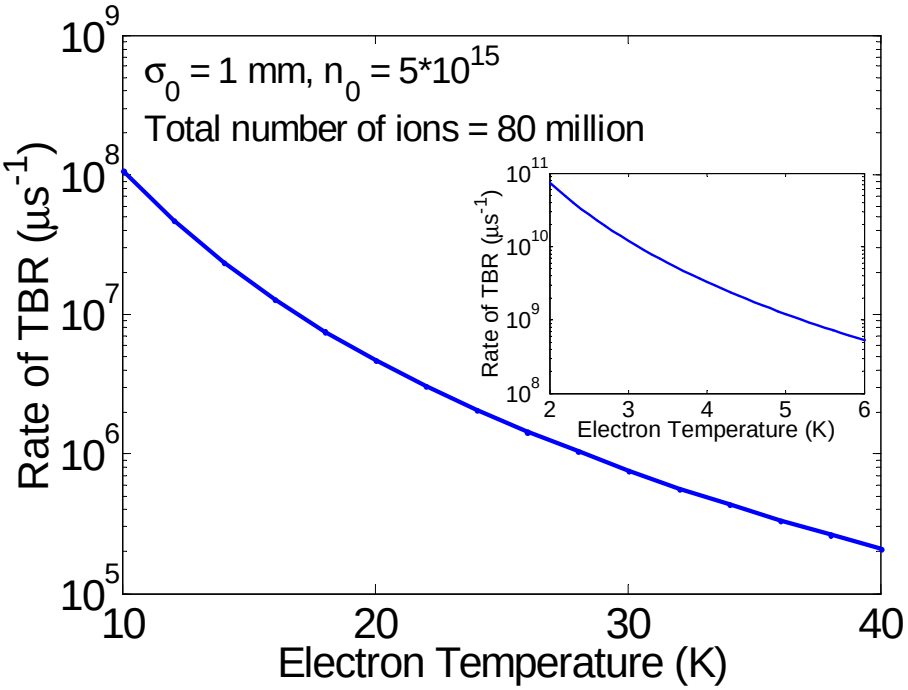

Figure 2.4: The figure shows the rate of TBR as a function of electron temperature for a typical set of plasma conditions. The rate decreases rapidly with increasing electron temperature. The inset shows the rate for electron temperatures colder than 6 K. The rate is plotted in units of μs^{-1} to facilitate estimating the number of ions and electrons that would recombine on the plasma expansion timescale.

as the electron temperature drops. TBR becomes more significant at higher plasma density and lower electron temperatures. Fig. 2.4 shows the strong dependence of the TBR rate on the electron temperature. The rate is plotted in units of μs^{-1} to facilitate estimating the number of ions and electrons that would recombine on the plasma expansion timescale.

As shown in the inset of Fig. 2.4, at low temperatures ($< 10K$), the recombination rate is tremendously high, which brings in a lot of heat to the electrons such that the electrons are pushed out of the strongly coupled regime. Typically, there are 50 - 100 million ions in the UNP cloud. According to Fig. 2.4, the entire UNP cloud should

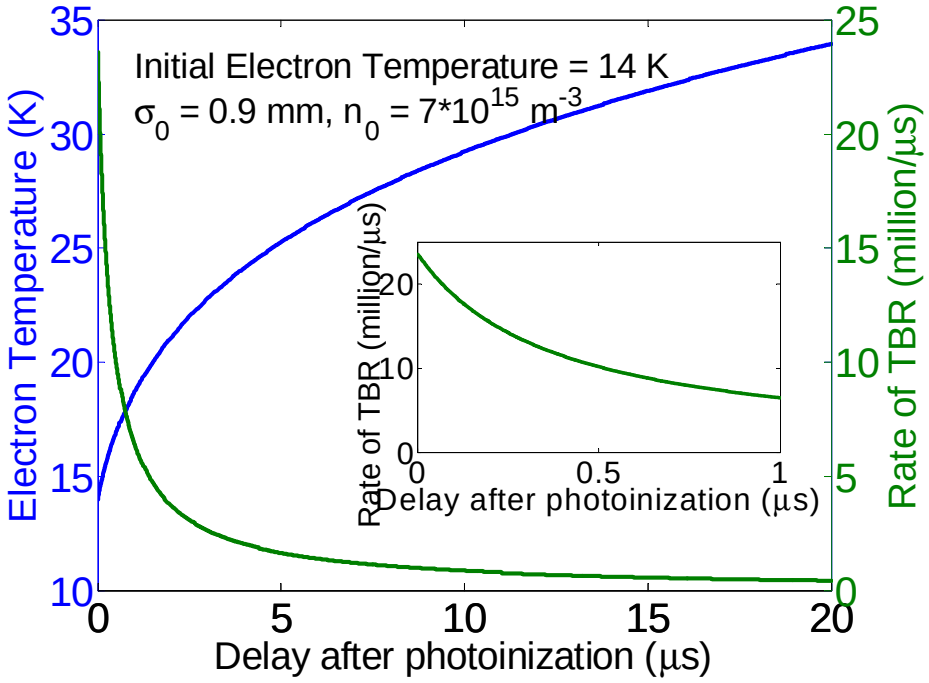

Figure 2.5: The rate of TBR decreases with delay after photoionization since TBR is a negative feedback effect. So as the electrons heat due to energy released during TBR, the rate of TBR decreases. The rate also decreases due to decreasing density as the plasma expands. This decrease in density with time is included in the calculations estimating the electron temperature shown in the figure. The inset gives an estimate of how many ions recombine within the first microsecond after photoionization; however, this is not an exact calculation since other electron heating effects are not taken into account.

recombine within a microsecond for very low initial electron temperatures. However, due to its dependence on $T_e^{-9/2}$, as the electrons heat up due to recombination, the rate of TBR decreases. So within a few nanoseconds after TBR begins, the electrons are at a higher temperature, which leads to a lower TBR rate. Hence, a UNP cloud does not spontaneously evolve into a cloud of Rydberg atoms when we start with low initial electron temperatures. Fig. 2.5 shows the variation of the rate of TBR with delay after photoionization, incorporating the fact that the electrons heat up by $2k_BT_e$ per recombination event. So at each instant of time, the rate is calculated with the

new (higher) electron temperature, but effects of plasma expansion are not taken into account. TBR rate decreases as the plasma expands and the density drops. Note that the calculations shown in the figure are not the result of a theoretical simulation of the electron temperature evolution taking into account the various physical processes in detail. The results shown are from a simple, preliminary calculation using Eq. 2.6. Hence, that equation should be used only to view the general trend of the effects of TBR. The rate of TBR in UNPs is greatly suppressed by the subsequent de-excitation of the Rydberg atoms formed because the de-excitation process also heats the electrons, as explained in the next section.

There is an ongoing debate on the validity of the TBR expression, Eq. 2.6, for ultracold plasmas in which the electron temperatures are very low, resulting in an exceptionally large rate of recombination. At such low electron temperatures, the electron Coulomb coupling parameter, $\Gamma_e > 1$, while, Eq. 2.6 has been derived for the case in which $\Gamma_e < 1$ meaning that the electrons are not strongly coupled. Hahn [67] modified the TBR theory to include the effects corresponding to $\Gamma_e > 1$. Kuzmin *et al.* [28] discuss this topic and explain that due to effects such as threshold lowering and disorder-induced heating, the electrons are rapidly pushed out of the strongly coupled regime in a matter of a few nanoseconds after plasma creation. Therefore, it is acceptable to use the traditional expression given by Eq. 2.6 to describe the rate of TBR in a UNP.

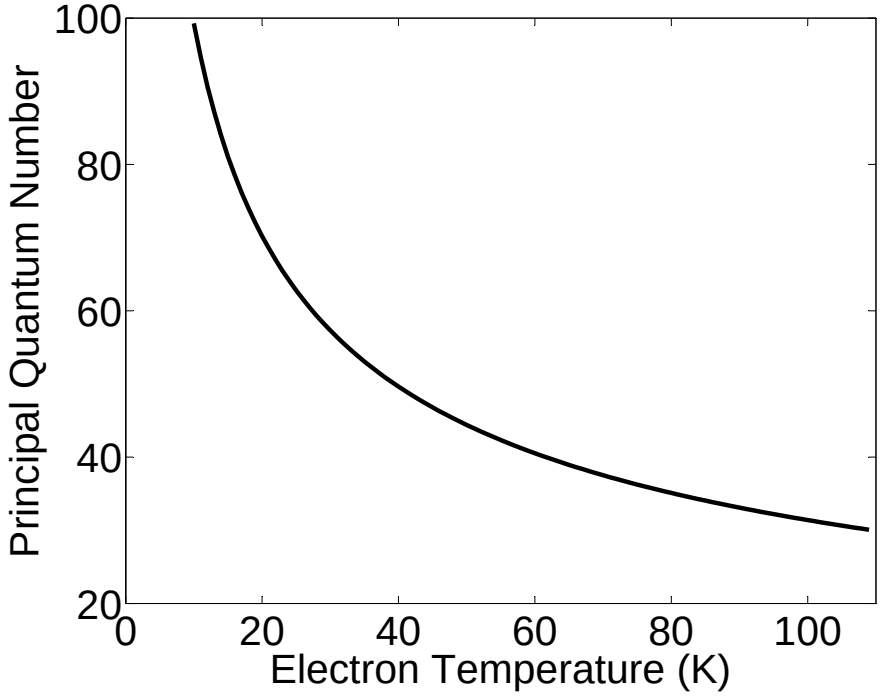

Figure 2.6: The principal quantum number into which an atom recombines due to TBR is plotted as a function of electron temperature. For colder electrons, the plasma recombines into higher lying Rydberg states which then undergo collisions with electrons to either de-excite to lower levels or be excited to higher levels.

2.2.6 Rydberg-electron collisions

Rydberg atoms play a large role in the evolution of UNPs. The formation of Rydberg atoms heats the electrons, thereby accelerating the expansion of UNP. Another dominant process that heats the electrons is Rydberg-electron collisions [26, 56]. When electrons collide with Rydberg atoms, the Rydberg atom can be de-excited to a lower energy level and the energy released is taken up by the electron. Since collisions with Rydberg atoms can heat up the electrons tremendously, it can suppress the rate of TBR.

Robicheaux *et al.* [26] show that the rate of de-excitation of Rydberg atoms (with

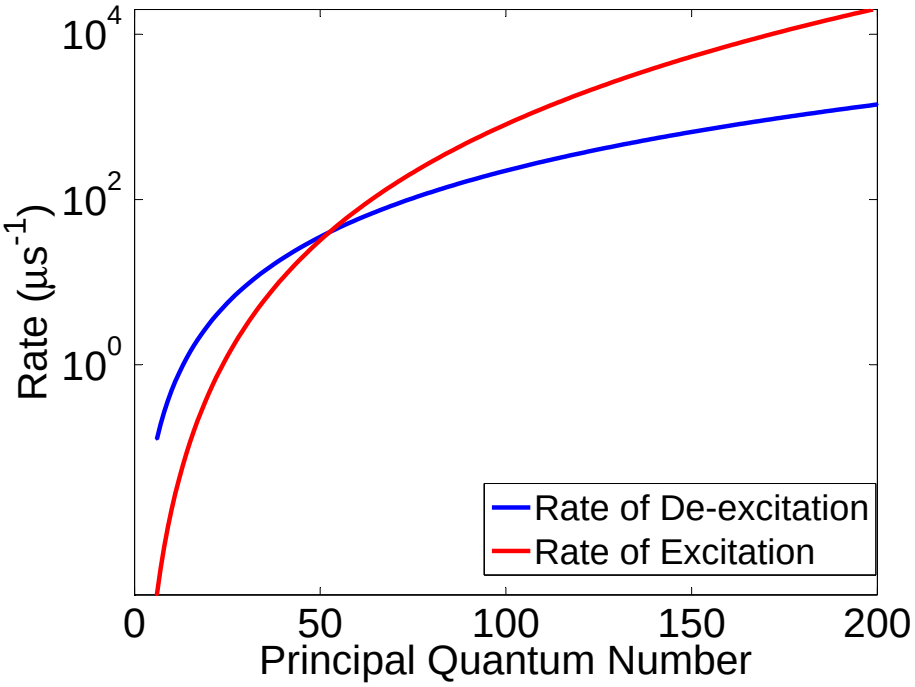

Figure 2.7: The figure shows the rate of excitation and de-excitation of Rydberg atoms due to collisions with electrons as a function of the principal quantum number of the Rydberg atoms. The rate of de-excitation is greater for lower lying Rydberg levels. The rate of excitation is tremendously higher than the rate of de-excitation as we go to higher lying Rydberg levels. The two rates become equal at principal quantum number ~ 53.

principal quantum number ν), due to collisions with electrons is given by

$$A_d = n_e(r)7.2\left\{\frac{27.2eV}{k_B T_e}\right\}^{0.17}\nu^{2.66}a_0^2\alpha_f c, \tag{2.7}$$

and total excitation rate is given by

$$A_e = n_e(r)55\left\{\frac{27.2eV}{k_B T_e}\right\}^{-0.83}\nu^{4.66}a_0^2\alpha_f c, \tag{2.8}$$

where a_0 is the Bohr length, c is the speed of light, $\nu = \sqrt{-13.6eV/E_R}$ is the principal

quantum number of a Rydberg atom with internal energy E_R and α_f is the fine structure constant.

Fig. 2.6 shows the variation of the principal quantum number, $q = \sqrt{13.6e/2k_BT_e}$, of the typical Rydberg atoms formed due to TBR as a function of the typical initial electron temperatures of the UNP. Fig. 2.7 shows the rate of excitation and de-excitation of Rydberg atoms due to collisions with electrons as a function of the principal quantum number of the Rydberg atoms undergoing the collisions. The rate of excitation, A_e, is almost the same as the rate of de-excitation, A_d, for Rydberg atoms in principal quantum numbers less than $q = 53$. However, $A_e >> A_d$ for $q > 60$ which corresponds to electron temperatures less than $T_e \sim 30\,K$ as shown in Fig. 2.6. This implies that there is much more excitation of Rydberg atoms due to collisions with electrons than de-excitation for higher lying Rydberg atoms. Since excitation of Rydberg atoms takes away energy from the electrons, this high rate of Rydberg atoms excitation should lead to tremendous cooling of the electrons. However, at such low electron temperatures of a few Kelvin, the rate of recombination is tremendously high, as shown in Fig. 2.4, which more than balances the cooling effect due to excitation resulting in a net heating of the electrons. When we start with electron temperatures greater than $T_e \sim 40\,K$, the rate of TBR is low; however, $A_d \geq A_e$ leading to a net heating of the electrons. If electron temperature is high, then the rate of TBR and Rydberg-electrons collisions is negligible. Chapter 5 will discuss experimental data displaying such behavior.

2.2.7 Radiative decay of Rydberg atoms

A Rydberg atom can also decay radiatively such that the atom decays to a lower energy level and a photon(s) is released. Once a Rydberg atom decays to a lower energy level, it does not heat the electrons due to collisions since the rate of Rydberg-electron collisions decreases considerably. Hence, due to radiative decay of Rydberg atoms, there are fewer Rydberg-electron collisions which would otherwise lead to electron heating. Therefore, radiative decay of Rydberg atoms in a UNP is significant since it leads to less heating of electrons because of Rydberg-electron collisions during plasma expansion. Robicheaux *et al.* [26] show that the rate of radiative decay of a Rydberg atom from a level ν_i to ν_f is given by

$$A_{\nu_i \to \nu_f} = \frac{8\alpha_f^4 c}{3\sqrt{3}\pi a_0} \frac{1}{\nu_i^5 \nu_f} \frac{1}{1 - (\nu_f^2/\nu_i^2)} \tag{2.9}$$

and the total radiative decay rate is

$$A_{\nu_i} = \sum_{\nu_f=\nu_0}^{\nu_i - 1} A_{\nu_i \to \nu_f}, \tag{2.10}$$

where ν_0 is the lowest possible state that the atom can decay into.

Pohl *et al.* [56] discussed the distribution of the population of Rydberg atoms in different principal quantum numbers at different delays after photoionization. They

give an overall rate of change of density of Rydberg atoms in a quantum level ν_f as

$$\dot{n}_a(\nu_f) = n_e \Sigma_{\nu_i}[K(\nu_i, \nu_f) n_a(\nu_i) - K(\nu_f, \nu_i) n_a(\nu_f)] + n_e[R(\nu_f) n_e n_i - I(\nu_f) n_a(\nu_f)], \tag{2.11}$$

where $K(\nu_i, \nu_f)$ is the rate coefficient for electron impact de-excitation from level ν_i to level ν_f, $R(\nu_f)$ and $I(\nu_f)$ respectively are the rates of TBR into ν_f and ionization from ν_f. The rate coefficients K, R and I are taken from [65]. Pohl *et al.* [56] explain that at early delay times, due to the relatively higher electron energy, more deeply bound Rydberg states are formed. During the expansion of the UNP, electrons cool down such that at later delay times, higher level Rydberg states are formed which undergo collisions and radiative decay to form deeply bound Rydberg states.

2.2.8 Equilibration

Equilibration refers to the thermalization between the ions and electrons in a UNP. The various heating effects mentioned above become insignificant at high initial electron temperature. At low initial electron temperature, though, the effect of TBR, Rydberg-electron collisions and radiative decay is highly significant. So if we start with low initial electron temperature, the electrons rapidly heat up to a much higher temperature. In effect, the electrons in a UNP are always at a relatively higher temperature as compared to the ions which are at $\sim 1\,K$.

According to Spitzer [68], the ions and electrons would reach thermal equilibrium

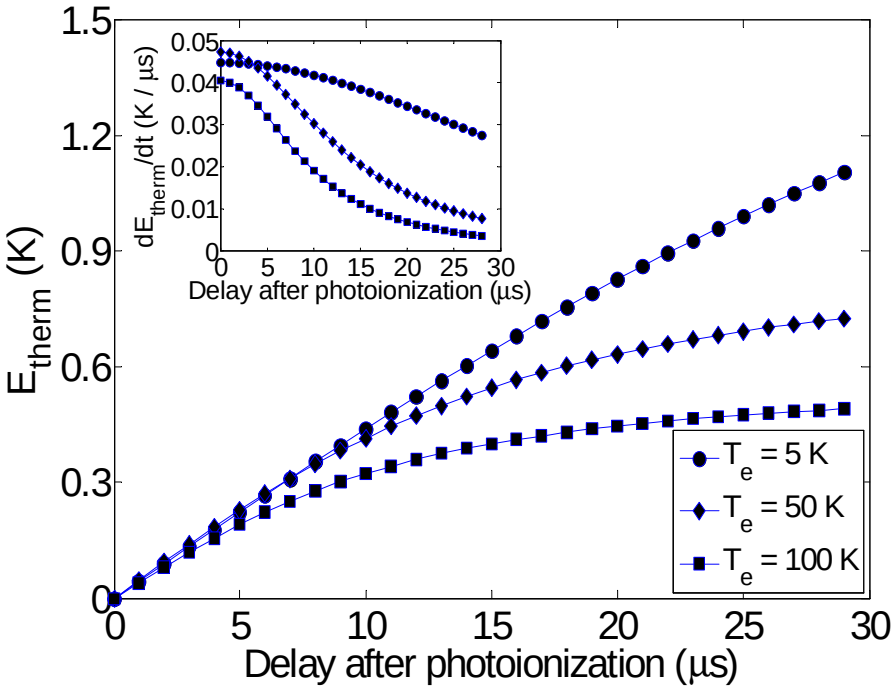

Figure 2.8: Ion-electron equilibration. Since the electrons have much higher thermal energy than the ions, there is some exchange of energy between the two in order to reach thermal equilibrium as the plasma evolves. The figure shows the amount of heat, integrated over time, given to the ions by the electrons for different initial electron temperatures for plasma cloud size = 1 mm and plasma density of $10^{15}\, m^{-3}$. The plasma density and electron temperature are propagated according to Eqs. 4.2 and 4.4 respectively. The inset shows the rate at which heat is exchanged between the ions and electrons. As is evident from the inset, the heat exchange is negligible during the observable time of plasma expansion.

in time given by

$$t_{eq} = \frac{5.87 A_e A_i}{n_i Z_e^2 Z_i^2 ln\Lambda} \left\{ \frac{T_e}{A_e} + \frac{T_i}{A_i} \right\}^{3/2}, \tag{2.12}$$

where A is the atomic mass in atomic mass units, Z is the charge in units of electronic charge 'e', the subscripts e and i refer to electrons and ions respectively and $ln\Lambda$ is the 'Coulomb Logarithm', given by

$$\Lambda = \frac{3}{2 Z_e Z_i e^3} \left\{ \frac{k_B^3 T_e^3}{\pi n_e} \right\}^{1/2}. \tag{2.13}$$

For $T_e = 30\,K$, $T_i = 1\,K$ and $n_i = n_e = 10^9\,cm^{-3}$, we get $t_{eq} = 160\,\mu s$. Hence, as the plasma evolves, there is some exchange of thermal energy between the ions and electrons. The rate at which the electrons heat the ions collisionally can be estimated using [32]

$$\begin{aligned} \frac{dE_{therm}}{dt} &= \sqrt{32\pi}\frac{e^4 n(t)}{(4\pi\epsilon_0)^2\sqrt{m_e k_B T_e(t)}}\frac{m_e}{m_i} ln\left\{\frac{\sqrt{3}}{\Gamma_e^{3/2}(t)}\right\} \\ E_{therm} &= \int dt\,\sqrt{32\pi}\frac{e^4 n(t)}{(4\pi\epsilon_0)^2\sqrt{m_e k_B T_e(t)}}\frac{m_e}{m_i} ln\left\{\frac{\sqrt{3}}{\Gamma_e^{3/2}(t)}\right\} \end{aligned} \tag{2.14}$$

Fig. 2.8 shows the total heat exchanged between the ions and electrons with delay after photoionization for three different initial electron temperatures. The heat exchanged is greater for lower electron temperature. The inset of Fig. 2.8 shows the rate at which heat is exchanged between the ions and electrons. The rate of heat exchange depends on the density of the plasma. For higher initial electron temperature, the rate of plasma expansion is higher such that the density of the plasma decreases rapidly. This decrease in density causes a lower rate of heat exchange at later delay times for higher initial electron temperature plasmas. Hence, in Fig. 2.8, the E_{therm} curve for $T_e = 100\,K$ tends to plateau, while the curve for $T_e = 5\,K$ still looks fairly linear.

2.2.9 Previous work

Electron temperature in a UNP has been studied by several theorists and experimentalists. For low initial electron energies, Kulin *et al.* [18] observe that the ion

terminal velocity, which is a measure of the initial electron energy, was much higher than what was provided to the electrons by the ionizing photon. They explain that the heating of electrons due to only threshold lowering could not explain the results. They followed up their work with [66] in which they show that TBR causes tremendous heating of the electrons. Robicheaux *et al.* [26, 27] simulated the expansion of UNPs and confirmed that TBR is indeed a significant process which heats the electrons tremendously. Due to the various electron heating processes, the electron Coulomb coupling parameter remains < 1 during the entire plasma expansion such that strong coupling among electrons does not develop during the UNP evolution [19, 27, 28]. Mazevet *et al.* [33] simulated the first few nanoseconds of plasma evolution and show that TBR occurs rapidly on the order of nanoseconds after plasma formation. Pohl *et al.* [56] also simulated the UNP evolution using a kinetic theory approach and a hybrid molecular dynamics approach. They studied the formation of Rydberg atoms in UNPs and the adiabatic cooling of electrons during the expansion. They also show that ion-ion correlations do not play a significant role in the evolution of the electron temperature.

An experimental study of the electron temperature evolution was done by [19]. They saw that due to the various competing heating and cooling mechanisms during the UNP expansion, the electron temperature was driven to a relatively narrow range over time no matter what the initial electron temperature was. It is these heating and cooling mechanisms that make the evolution of electron temperature a

complicated process. A clear understanding of each of these processes is critical to decipher the electron temperature evolution process. This thesis describes a study of the electron temperature evolution under various initial conditions (see Chapter 5), including exciting Rydberg atoms and letting them evolve into a plasma. With the help of simulations, the electron temperature evolution for the various initial conditions is determined and processes which are more significant than the others under different conditions are identified.

Chapter 3

Study of Plasma Expansion

3.1 Background

UNPs expand due to the thermal pressure of the electrons. Since the electrons have high kinetic energy, they tend to leave the plasma cloud. As the electrons leave, the Coulomb force due to the net positive charge in the cloud, pulls the electrons back into the cloud. In this process, the ions face a recoil force in a direction directed radially outwards. Hence, as the plasma expands, the thermal energy of the electrons gets converted into expansion energy of the ions and causes the whole cloud to expand radially outwards over time. Fig. 3.1 shows a schematic of UNP expansion. As the

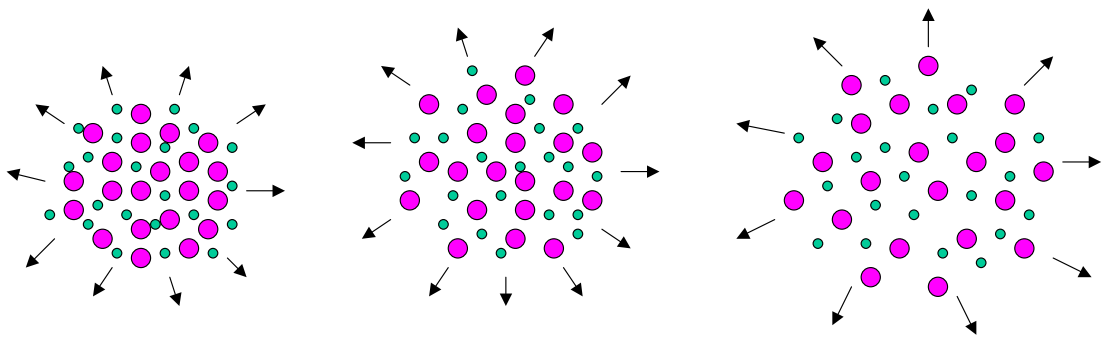

Figure 3.1: The thermal pressure of the electrons exerts a force on the ions directed radially outwards. This force causes the plasma to expand radially outwards with time.

delay increases, plasma expansion directed radially outwards is depicted in the figure.

Within a few microseconds after photoionization, the thermal energy of the ions becomes negligible compared to their expansion energy. When essentially all the electron thermal energy has been transferred, the ions attain terminal velocity. Kulin *et al.* [18] show that during the expansion, the ions obtain terminal velocity when essentially all electron thermal energy is converted into ion expansion energy. As the electrons cool down during the adiabatic expansion, their thermal energy also becomes insignificant compared to the expansion energy in the plasma within a few tens of microseconds.

UNP expansion is similar to expansion of other plasmas produced by an intense laser field irradiating solid targets [35, 36], thin foils [37–45], rare gas clusters [46], and gas jets [47, 48]. Gurevich *et al.* [69] did the pioneering work on expansion of plasmas in vacuum, and were the first to show that the electric field produced by the plasma accelerates the ions. They used the Vlasov kinetic equations which describe the distribution function of ions and electrons to obtain a numerical solution to the evolution of the density and velocity of the ions. Although the plasma expansion described in [69] was isothermal, it motivated studies on the problem of an adiabatic plasma expansion.

An exact solution to the problem of a plasma expanding into a vacuum, when adiabatic cooling of the electrons dominates, was identified for a 1-dimensional [70] system describable with the Vlasov equations. This solution was extended to 3-

dimensions by Dorozhkina *et al.* [71]. Mora *et al.* [72] describe an exact solution to the self-similar plasma expansion for a Gaussian quasineutral (see section 3.4.3) plasma.

The ions and electrons created in hot plasma experiments have energies on the order of MeV which makes it challenging to study their motion with good time resolution. UNPs have an advantage over these plasmas since the ions and electrons have energy on the order of meV or even μeV and so their motion can be studied using standard optical techniques. With the excellent control we have over the experimental conditions, UNPs provide a great experimental source to study plasma expansion and compare experimental results with theory. They satisfy the criteria for a self-similar plasma expansion since they are quasineutral and have a Gaussian density distribution. Realizing systems which can be studied experimentally as well as simulated theoretically is critical in establishing fundamental models which might then help in understanding more complex systems.

Robicheaux *et al.* [26, 27] have developed a theory for the expansion of UNPs. Using a molecular dynamics approach, they discuss the role of the various physical processes that take place as the UNP evolves, and their effect on the ion and electron temperature evolution. They especially studied the role of three body recombination and electron-Rydberg scattering in an expanding UNP. Pohl *et al.* [56] also developed a theory for UNP expansion; most of their simulations used a kinetic theory model. They show that the effect of ion-ion correlations resulting from strong coupling plays

an insignificant role in plasma expansion studies. This is because the correlation energy is negligible compared to the expansion energy of the ions. Hence the effect of the ion-ion correlations are neglected in this study. Experimentally, Cummings *et al.* [13, 14] studied the expansion of a cylindrical plasma; however, they found significant deviations from theory which probably arose since their plasma was not spherically symmetrical.

3.2 Theoretical description

UNPs have an advantage over traditional hot plasmas in that due to their low temperatures, they evolve over a timescale which can be studied with great temporal resolution using optical probes. Since the system can be studied experimentally, the experimental results can be compared with theory and verify one with the other. Many theorists have simulated the ion and electron temperature evolution during the expansion of a UNP. Following the work of Killian *et al.* [10], Mazevet *et al.* [33] simulated and verified the threshold condition on the number of ions for creation of UNPs. They also showed that the timescale for certain electron heating mechanisms can be as small as a few nanoseconds after photoionization. Robicheaux *et al.* [26, 27] simulated the expansion of UNPs and studied the various processes that heat and cool the electrons. They also simulated the profile of the ion radial acceleration due to the thermal pressure of the electrons. Kuzmin *et al.* [28] show that various rapid electron heating processes suppress the development of strong electron correlations

in a UNP. Pohl *et al.* [1, 25, 31, 56] have studied various aspects of the evolution of ions and electrons using a hybrid molecular dynamics model. Different theorists have used different models to simulate UNP evolution based on their treatment of the ions and electrons either as particles which are propagated individually or as a fluid.

What makes these simulations challenging is the different timescales over which the ions and electrons evolve. Due to their light mass, the electrons thermalize over a nanosecond timescale while the local ion thermalization and plasma expansion occur on a microsecond timescale. If the time step in the simulations is set at a nanosecond level then it is tough to evolve the plasma over many microseconds, while if the time step is set at a microsecond scale then some of the physical processes that occur on a nanosecond scale are not resolved. Hence, different treatments are used to look at different effects in a UNP depending on whether the process of concern occurs on a rapid timescale or on the plasma expansion timescale.

3.2.1 Kinetic theory

Pohl *et al.* [56] have developed the kinetic approach to simulate the evolution of UNPs. A summary of their work in that paper is presented in this subsection. This work is critical to the picture we will use to understand of the ion and electron temperature evolution during the plasma expansion. The results of this work will be used to analyze and explain the data in Chapters 4 and 5.

Under the assumption that the ions and electrons in a UNP are not strongly coupled, and neglecting any collisional processes, the evolution of the one particle

distribution function, $f_\alpha(\mathbf{r}_\alpha, \mathbf{v}_\alpha)$, of a charged particle at position $\mathbf{r}$ with velocity $\mathbf{v}$, is described by the Vlasov equation

$$\frac{\partial f_\alpha}{\partial t} + \mathbf{v}_\alpha \frac{\partial f_\alpha}{\partial \mathbf{r}_\alpha} - m_\alpha^{-1} \frac{\partial f_\alpha}{\partial \mathbf{v}_\alpha} q_\alpha \frac{\partial \phi(\mathbf{r}_\alpha)}{\partial \mathbf{r}_\alpha} = 0. \tag{3.1}$$

Here, $\alpha =$ e, i for electrons and ions respectively, m_α and q_α are the mass and charge of the species α, and ϕ is the total mean-field potential determined by the Poisson equation

$$\nabla^2 \phi = \frac{e}{\epsilon_0}(n_e - n_i), \tag{3.2}$$

where $n_\alpha = \int f_\alpha d\mathbf{v}_\alpha$. Due to the different timescales of evolution of the ions and electrons, it would be computationally intensive to propagate both charged species individually through the evolution.

Since the electrons thermalize among themselves within a few nanoseconds which is much faster than the ion thermalization timescale, using the adiabatic approximation, we can assume a Maxwellian distribution for the electrons

$$f_e(\mathbf{r}, \mathbf{v}, t) \propto exp\left\{\frac{\phi(\mathbf{r})}{k_B T_e(t)}\right\} exp\left\{-\frac{m_e v^2}{2k_B T_e(t)}\right\}. \tag{3.3}$$

The adiabatic approximation implies that the electrons re-thermalize rapidly with any change in the Coulomb potential in the system. Substituting Eq. 3.3 into 3.1 and using the quasineutrality assumption ($n_e \approx n_i$), we can express the mean-field

potential in terms of the ion density as [73]

$$e\frac{\partial\phi}{\partial\mathbf{r}} = k_B T_e n_i^{-1}\frac{\partial n_i}{\partial\mathbf{r}}. \tag{3.4}$$

Note: $n_e \approx n_i$ does not imply $(\partial\phi/\partial\mathbf{r}) = 0$. For more information on quasineutrality in UNP, see section 3.4.3. The UNP has a spherically symmetric Gaussian density distribution for which Eq. 3.4 yields a linear force on an ion given by

$$\vec{F}(\vec{r},t) = e\vec{E} = e\frac{\partial\phi}{\partial\mathbf{r}} = \frac{k_B T_e(t)\vec{r}}{\sigma(t)^2}. \tag{3.5}$$

Fig. 3.1 illustrates the effect of a force on the ions directed radially outwards.

Substituting Eq. 3.4 for a Gaussian distribution into 3.1, for a self-similar expansion of ions (ignoring ion-ion correlations), Eq. 3.1 can be solved exactly to obtain,

$$f_i \propto exp\left\{-\frac{r^2}{2\sigma^2}\right\} exp\left\{-\frac{m_i(\vec{u}-\vec{v})^2}{2k_B T_i}\right\}, \tag{3.6}$$

$$\vec{v} = \gamma\vec{r}. \tag{3.7}$$

Integrating Eq. 3.6 over space and velocity, Pohl *et al.* arrive at the following set of equations which describe the plasma evolution:

$$\partial_t\sigma^2 = 2\gamma\sigma^2, \tag{3.8}$$

$$\partial_t\gamma = \frac{k_B T_e + k_B T_i}{m_i\sigma^2} - \gamma^2, \tag{3.9}$$

$$\partial_t(k_B T_i) = -2\gamma k_B T_i, \tag{3.10}$$

$$\partial_t(k_B T_e) = -2\gamma k_B T_e. \tag{3.11}$$

where ∂_t represents the time derivative. Eq. 3.10 and 3.11 reflect the cooling of the ions and electrons as the plasma evolves. Combining Eqs. 3.8-3.11, implies that the total energy of the plasma,

$$E_{tot} = N_i \left\{ \frac{3}{2}(k_B T_e + k_B T_i) + \frac{3}{2} m_i \gamma^2 \sigma^2 \right\} \tag{3.12}$$

is conserved. Solving Eqs. 3.8-3.11 determines the evolution of the size of the plasma cloud, the expansion velocity, $\mathbf{v}(\mathbf{r}, t) = \gamma(t)\mathbf{r}$, and the ion and electron temperatures:

$$\sigma^2(t) = \sigma^2(0)(1 + \frac{t^2}{\tau_{exp}^2}), \tag{3.13}$$

$$\gamma(t) = \frac{t/\tau_{exp}^2}{1 + t^2/\tau_{exp}^2}, \tag{3.14}$$

$$T_i(t) = \frac{T_i(0)}{1 + t^2/\tau_{exp}^2}, \tag{3.15}$$

$$T_e(t) = \frac{T_e(0)}{1 + t^2/\tau_{exp}^2}, \tag{3.16}$$

where the characteristic plasma expansion time is given by

$$\tau_{exp} = \sqrt{\frac{m_i \sigma^2(0)}{k_B[T_e(0) + T_i(0)]}}. \tag{3.17}$$

The above theory did not include any collisional processes that occur in UNPs.

However, in this thesis, the UNP expansion has been studied for various initial conditions (see Chapter 5) when two-body and three-body collisions are significant. In particular, three-body recombination is a dominant process and affects the electron temperature evolution tremendously (see section 2.2.5). The inelastic collision effects are included in the kinetic approach shown above with the help of rate equations which describe the rate at which the Rydberg atoms are formed and also their rate of excitation and de-excitation:

$$\dot{n}_a(\nu_f) = n_e \Sigma_{\nu_i}[K(\nu_i, \nu_f) n_a(\nu_i) - K(\nu_f, \nu_i) n_a(\nu_f)] + n_e[R(\nu_f) n_e n_i - I(\nu_f) n_a(\nu_f)], \tag{3.18}$$

where $K(\nu_i, \nu_f)$ is the rate coefficient for electron impact de-excitation from level ν_i to level ν_f, $R(\nu_f)$ and $I(\nu_f)$ are the rates of TBR into ν_f and ionization from ν_f respectively. The rate coefficients K, R and I are taken from [65]. The energy conservation equation is now modified to $E_{tot} + E_a =$ constant where $E_a = -R\Sigma_{\nu_f} N_a \nu_f^2$ is the total energy of the Rydberg atoms, N_a is the number of atoms recombined and $R = 13.6\, eV$. The evolution becomes complicated with the inclusion of such collisional processes and an analytic solution is no longer possible. Hence, numerical techniques are needed to determine the evolution of the plasma.

In addition to that, Eqs. 3.8-3.11 would not be a closed set of equations if we include the effect of strong coupling of the ions. In order to include the effect of the ion-ion correlations accurately, a microscopic approach to solving the plasma evolution is required. (As shown by Pohl *et al.* [56], the ion-ion correlations can be neglected

for the study of the electron temperature evolution during plasma expansion.)

3.2.2 Molecular dynamics simulations

While the kinetic approach describes the plasma evolution to a large extent, it does not include fully the effect of ion-ion correlations. Hence, as explained by [56], the molecular dynamics (MD) simulations [28] are employed which include the effect of the ion correlations. Due to the large difference in the evolution timescale of the electrons and ions, a full MD simulation including both the ion and electron interactions is computationally demanding. Hence MD simulations are not employed to study plasma expansion over microsecond timescale.

3.2.3 Hybrid molecular dynamics model

The HMD model assumes instantaneous equilibration of the electrons and they are treated on a hydrodynamic level as in the kinetic model described earlier. However, the ions are propagated individually and their interactions among themselves and with the electrons are fully taken into account. Ignoring the electron-electron correlations allows for large time steps during the propagation of time in the simulations. The large time steps enable us to compare the simulation results with experiments during the study of plasma expansion since the two timescales are similar. However, for this study, the hydrodynamic treatment of the ions and electrons, as described in the kinetic theory approach, will suffice since as shown by [56], the ion-ion correlations do not affect the plasma expansion and electron temperature evolution on a long

timescale.

3.3 Detection of UNP

The ultracold temperatures and low plasma density make it convenient to observe the evolution of UNPs. The time scale for the expansion of the plasma is on the order of microseconds. Some probing methods to study UNP evolution are charged particle detection [10, 18, 19], fluorescence imaging [13, 14, 17] and absorption imaging [11]. Charged particle detection (CPD) typically makes use of an electric field which accelerates either the ions or the electrons (depending on the direction of the field) to a microchannel plate (MCP). The signal from the MCP can then be interpreted to study the evolution of the plasma. The initial studies of UNPs employed the CPD technique [10, 15, 18]. One of the drawbacks of CPD is that since the signal is only a measure of the number of charged particles arriving at the detector, the signal has no spatial resolution. In addition to that, the CPD signal needs to be calibrated to establish the signal corresponding to one ion/electron reaching the detector. The signal also needs to be calibrated temporally since there are time constants involved at various stages in the detection system. To resolve the UNP evolution, a probe with nanosecond resolution is needed; however, this level of resolution is not provided by the CPD technique.

Another technique to study UNPs, which overcomes some of the drawbacks of the CPD technique, is measuring the fluorescence signal from the ions. An ion can tran-

sition to an excited state by absorbing resonant light. When the excited ion decays to the ground state, it releases a photon which can be captured on a CCD camera. This technique is called fluorescence imaging [9, 14]. Fluorescence imaging technique has been used to study ultracold neutral Calcium plasmas [13, 14]. Fluorescence measurements of UNP have an edge over CPD since we can get excellent spatial and temporal resolution with this technique. However, the fluorescence signals are typically low. Hence, we need to average many times to get good signal to noise. The accuracy of this technique relies on the precision with which various parameters such as image beam intensity and number of averages are recorded during the experiment. Also, we need an exact calibration of how many counts on each pixel of the camera correspond to one photon at the detector.

This study uses absorption imaging spectroscopy which has excellent temporal and spatial resolution. The absorption imaging technique to image UNPs was developed for the first time in this laboratory [11, 74]. Although the absorption technique is very effective for studying the evolution of UNPs, it has its own drawbacks. The next section talks about absorption imaging spectroscopy in detail.

3.3.1 Absorption imaging spectroscopy

Absorption imaging spectroscopy [11, 74] is a powerful technique which provides *in situ* measurements with excellent resolution to observe UNPs. To obtain an absorption image of the plasma, a collimated laser beam tuned near resonance, illuminates the ions. After the beam goes through the ions, it falls on a CCD camera. The ions

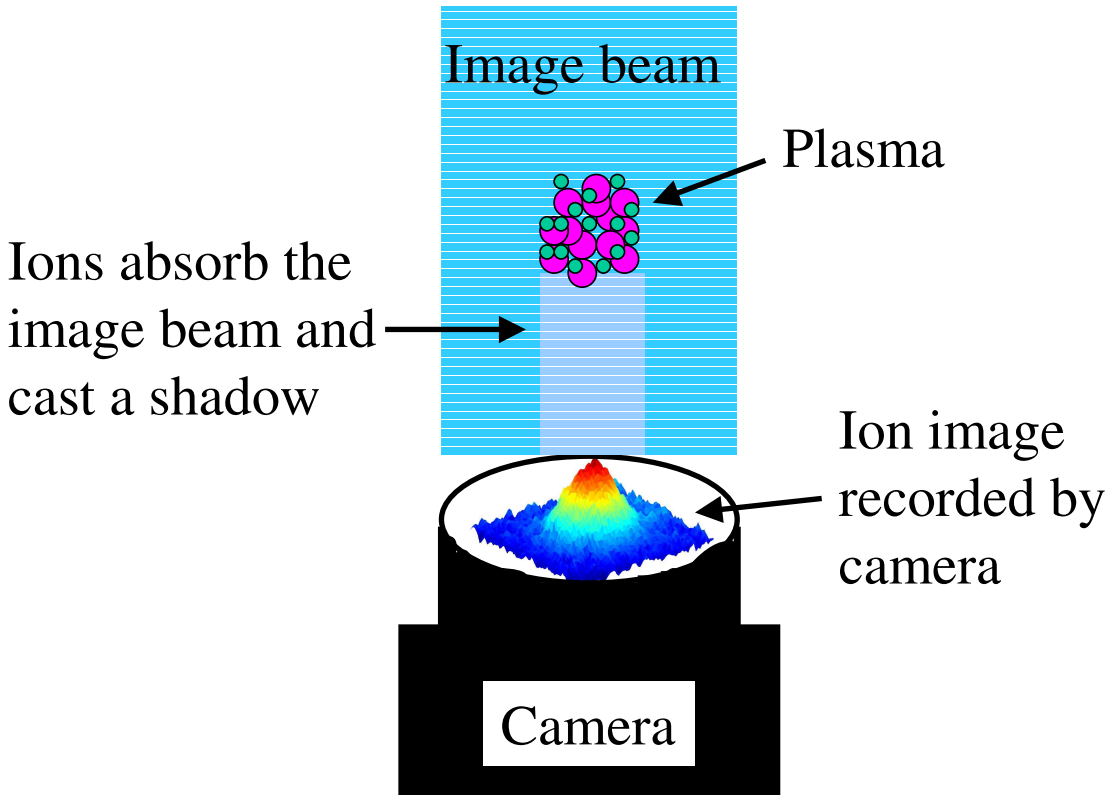

Figure 3.2: The figure shows a schematic of the absorption imaging technique. The ions are illuminated with resonant light. Since the ions absorb some of the light, they cast a shadow which is captured by a camera. The image captured by the camera gives us a wealth of information about the plasma dynamics.

scatter some photons out of the image beam and cast a shadow which is recorded by the camera. Fig. 3.2 shows the basic schematic to obtain an image of the ions.

The plasma evolves over a short timescale, sometimes as short as a few nanoseconds, so a detection technique with a high time resolution is essential. Some of the processes during plasma evolution require a detailed spatial analysis of the plasma cloud. To highlight such processes, the plasma detection technique needs to have a sharp spatial resolution. Absorption imaging technique possesses both advantages therefore it is employed as an effective technique to study UNP evolution. Due to its

excellent resolution, it has been used to study laser-cooled and trapped neutral atoms [49, 75]. However, in order to take advantage of the optical technique, the ground state of the ion/atom should have a resonant transition at a wavelength which can be easily generated using lasers. Sr^+ has a resonant transition at 422 nm as shown in Fig. 3.3. We use a diode laser to obtain 844 nm light which is frequency doubled to obtain 422 nm light for imaging the plasma.

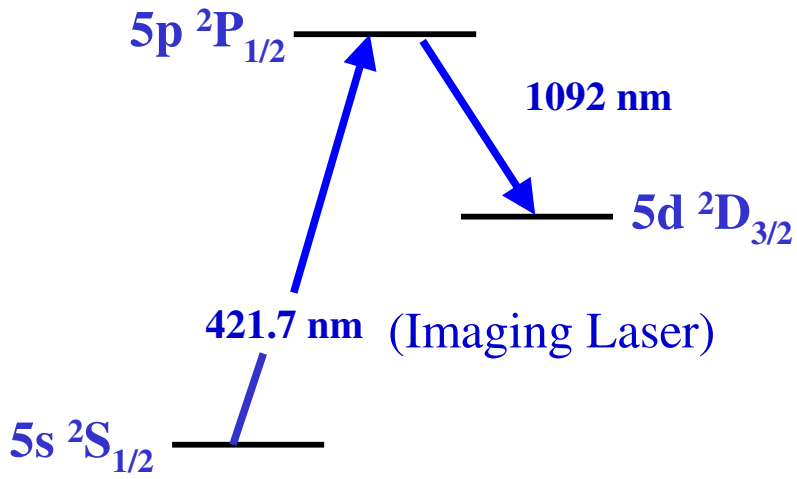

Figure 3.3: Ion Energy levels. The ions have a strong transition in the visible region of the spectrum which makes it convenient to observe them using optical imaging techniques such as absorption and fluorescence imaging. We double the 844 nm output of a diode laser to generate 422 nm imaging beam for the ions. Some of the ions decay to the D state; however, the decay rate is insignificant since the image beam has low intensity and is turned on for a short time.

Absorption imaging spectroscopy involves taking multiple images of the ions at different image beam frequencies close to the resonance frequency. From an analysis of these images, we obtain a spectrum of the ions. The spectrum gives information about the velocity of the ions and the number of ions present. Equipped with this information, we can determine the ion and electron evolution dynamics as will be

discussed in later chapters.

The absorption imaging technique has some drawbacks. Due to spatially uneven intensity of the image beam, the plasma image has an uneven baseline. Hence, we take another image with no ions present to obtain the baseline. The image with no ions present will be referred to as the background image. Another disadvantage of this technique is that we are limited in the minimum and maximum density of UNP that can be explored. In order to get images with good signal to noise, the lowest density that has been explored is on the order of $10^{14}\,m^{-3}$. Due to effects of radiation trapping, the maximum density that can be imaged is on the order of $10^{17}\,m^{-3}$. Fortunately, UNPs have a density range of $10^{15} - 10^{16}\,m^{-3}$, so we are able to observe all the significant physical processes during a UNP evolution.

The UNP detection begins with a measurement of the optical depth of the plasma cloud. Optical depth refers to the fraction of light that is scattered or absorbed by the atoms/ions in its path. Using Beer's law, the optical depth of the plasma cloud is obtained experimentally by,

$$OD_{expt}(x,y) = ln[I_{background}(x,y)/I_{plasma}(x,y)] \tag{3.19}$$

where I_{plasma} and $I_{background}$ are the image intensities with and without the plasma respectively. For a constant absorption cross-section, α, the OD of the cloud should

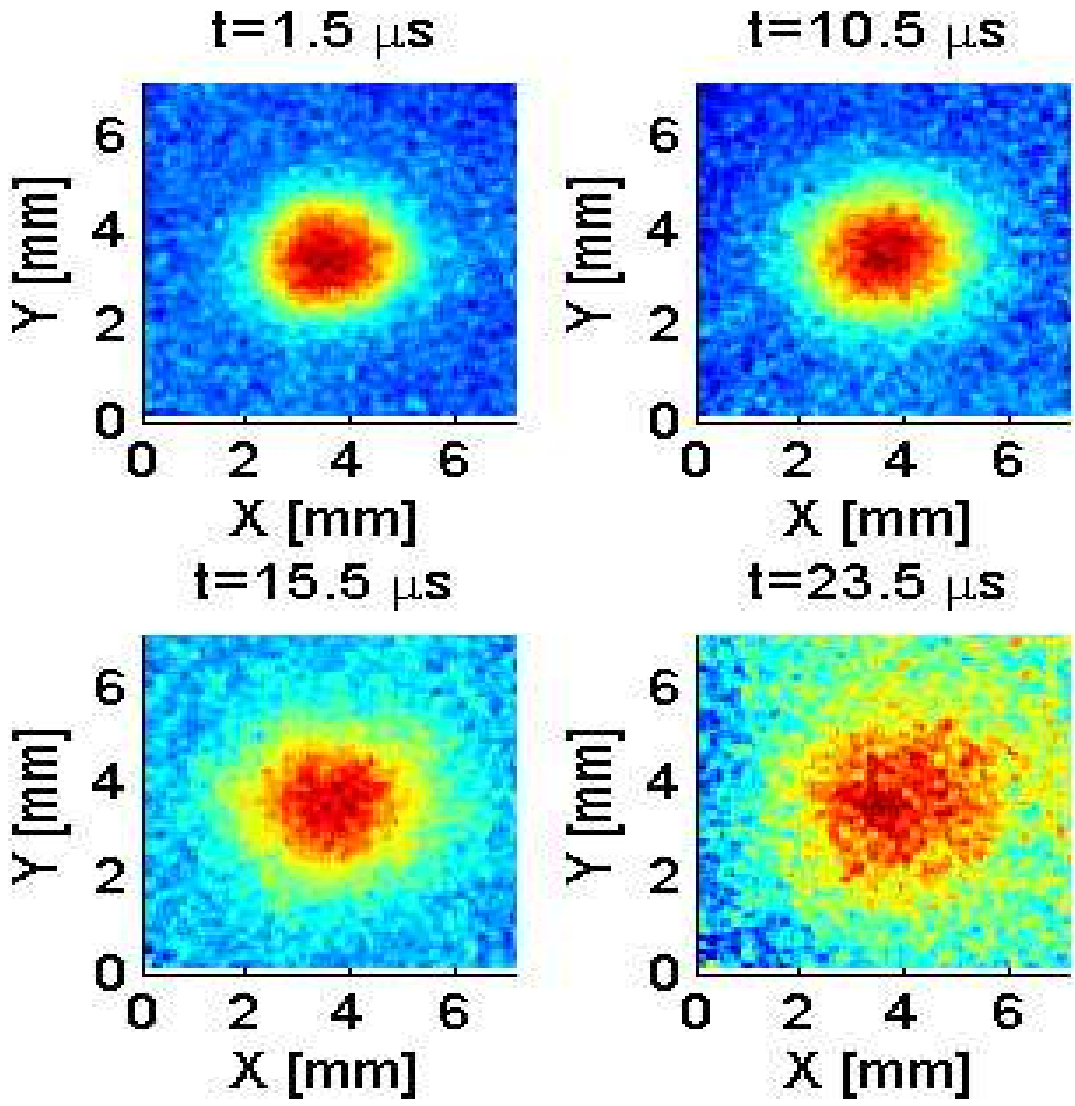

Figure 3.4: The figure shows images of UNP at 1.5, 10.5, 15.5 and 23.5 μs after photoionization. The plasma expands radially outwards due to the pressure of the electrons. The images show clear signs of expansion.

fit to a 2-D Gaussian:

$$OD(x,y) = \int n_{3D}(x,y,z)\alpha dz \tag{3.20}$$

$$= An_i(x,y) \tag{3.21}$$

where A is a constant that includes the value of the absorption cross-section and the amplitude from the integration over z (the direction of propagation of the probe beam), $n_{3D} \propto e^{-(x^2/2\sigma^2+y^2/2\sigma^2+z^2/2\sigma^2)}$ is the three dimensional Gaussian density distribution and n_i, known as the areal density, is the Gaussian density distribution averaged over the z-axis. [Note that α is a function of the probe beam frequency, ν and ion temperature, T_i. The ion temperature T_i is a measure of the thermal energy of the ions due to disorder-induced heating as explained in section 2.1.1. The assumption of a constant absorption cross-section throughout the cloud, is not a good approximation for UNPs. Ideally, we should perform an annular analysis (section 3.3.2) of the system and obtain the absorption cross-sections for different regions of the cloud. However, this approximation does not significantly affect the results of this thesis.] Fig. 3.4 shows the top view of typical absorption images. By simply looking at these images of the plasma, we can observe the plasma expanding. Fig. 3.4 shows images of plasma taken at 1.5, 10.5, 15.5 and 23.5 μs after photoionization. Plasma expansion is clearly evident from the figure.

The density distribution of the plasma is obtained by fitting the experimentally measured OD_{expt} (Eq. 3.19), to a theoretical model, and minimizing the χ^2. The χ^2

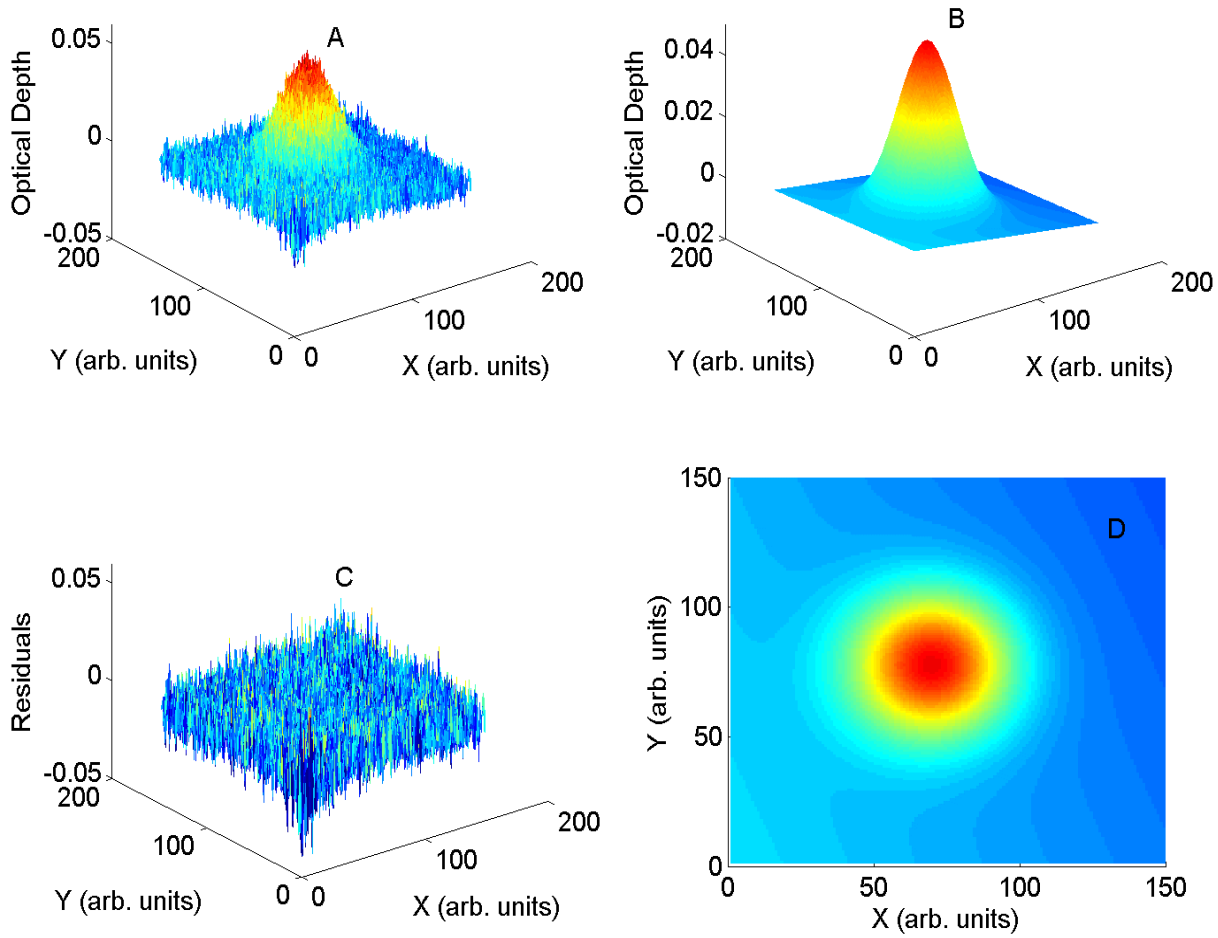

Figure 3.5: Absorption image. (A) shows a typical absorption image of a UNP where the optical depth of the plasma is plotted. The optical depth is fit to a two dimensional Gaussian to obtain the peak optical depth and the size of the cloud among other parameters. (B) shows a plot of the optical depth generated using the fit parameters. (C) shows the residues from the fit which is obtain by subtracting the fit from the data. (D) is a top view of the fit image shown in (B). It shows the shape of the cloud as seen by the image beam.

is minimized using the following function:

$$OD_{theory} = \left\{ T_o + slope_x(x - x_o) + slope_y(y - y_o) + C[e^{-\frac{(x-x_o)^2}{(2\sigma_x^2)} - \frac{(y-y_o)^2}{(2\sigma_y^2)}}] \right\}. \quad (3.22)$$

Here, x and y refer to the two coordinate axes, T_o refers to an overall offset, x_o and y_o refer to the center of the cloud in the two axes, $slope_x$ and $slope_y$ refer to the slope

in the OD which comes about due to uneven intensity of the image beam and poor background subtraction, σ_x and σ_y refer to the rms width of the cloud.

Due to poor signal to noise at the edge of the cloud where the density is low, the OD_{expt} measurements can have large uncertainties so a weighted fit is performed. Typically, in order to perform a weighted fit, one calculates $OD_{expt}(x_i, y_i)$ and the uncertainty in OD_{expt}: $err(x_i, y_i)$. Then using the fit function, OD_{theory}, the weighted χ^2 is minimized, where

$$\chi^2 = \frac{1}{N-1}\Sigma_i \left\{ \frac{OD_{expt}(x_i, y_i) - OD_{theory}}{err(x_i, y_i)} \right\}^2 . \tag{3.23}$$

It is assumed that the error in the counts on each pixel is the same throughout the image; a separate uncertainty in the OD for each pixel is not determined[1].

The error in OD_{expt} has many sources. There is shot to shot noise on the data due to fluctuations in the intensity of the ionizing pulse, and the intensity of the probe beam. Another contribution to the noise is from the changing shape of the probe beam. It is critical to account for these effects since the ability to obtain a good fit is greatly affected by the noise in the measurements. For example, introducing a term to account for the slope in the OD in Eq. 3.22, due to the changing beam shape, dramatically improved the results of the fit. The error in OD, using the method of

[1]The Matlab 'nlinfit' program that is used for the analysis does not allow a weighted fit such that we can input the uncertainties ($err(x_i, y_i)$) as a separate vector. Hence a different approach is taken to get the same result: An $OD_{expt}(x, y)/err(x, y)$ vector and $OD_{theory}/err(x, y)$ fit function is input to the fitting routine and minimize the χ^2.

propagation of error, is given by

$$\begin{aligned} OD(x,y) &= ln[I_{background}(x,y)/I_{plasma}(x,y) \\ \delta OD(x,y) &= \sqrt{\left\{\frac{\partial OD}{\partial I_{background}}\delta I_{background}\right\}^2 + \left\{\frac{\partial OD}{\partial I_{plasma}}\delta I_{plasma}\right\}^2} \\ &= \sqrt{\left\{\frac{\delta I_{background}}{I_{background}}\right\}^2 + \left\{\frac{\delta I_{plasma}}{I_{plasma}}\right\}^2} \end{aligned}$$

Under the assumption that $\delta I_{background}/I_{background} = \delta I_{plasma}/I_{plasma}$, we get

$$\delta OD(x,y) = \sqrt{2}\frac{\delta I_{background}}{I_{background}}. \tag{3.24}$$

The $\delta OD(x,y)$ is calculated using the following steps:

1. We identify a square of 5X5 pixels from the four corners of the plasma and background images (see black area in Fig. 3.6).

2. For each corner, we obtain the average difference between the pixel count of the plasma and background image.

$$AVG = \frac{\sum_{i=1}^{5}\sum_{j=1}^{5}(plasma_{i,j} - background_{i,j})}{25} \tag{3.25}$$

where $plasma_{i,j}$ and $background_{i,j}$ refers to the pixel count from the plasma image and corresponding background image corner respectively for the pixel i,j. (The subtraction is performed to get rid of fringes in the image.)

3. For each corner we obtain the rms of the difference between the pixel count on the

plasma and background image.

$$RMS = \sqrt{\frac{\sum_{i=1}^{5}\sum_{j=1}^{5}(plama_{i,j} - background_{i,j})^2}{25}} \tag{3.26}$$

4. We find the rms deviation by $\sqrt{RMS^2 - AVG^2}$.

5. We find the average of the rms deviations (DEV_{AVG}) from all four corners. This is the quantity $\delta I_{background}$ in Eq. 3.24.

6.The quantity $I_{background}$ in Eq. 3.24 is an average of the pixel counts in the background image. It is calculated by summing up the pixel counts for all the pixels in the background image and dividing the sum by the total number of pixels.

7. Thus, we obtain the uncertainty in the OD by dividing the quantity obtained in step 5 above by the quantity obtained in step 6.

Minimizing the χ^2 using Eq. 3.22 gives the value of the following fit parameters: $T_o, x_o, y_o, x_s, y_s, \sigma_x, \sigma_y$ and C. The peak optical depth of the cloud at a particular probe/image beam frequency is given by the fit parameter C. Fig. 3.5B and C shows a fit to the image shown in Fig. 3.5A and the residuals from the fit respectively. The residuals are calculated by subtracting the fit from the image. Fig. 3.5D shows a top view of the fit. The fit does not always give a $\chi^2 = 1$ due to non-statistical, shot to shot noise in the images. The theoretical expression for OD, given by Eq. 3.22, takes into account the fluctuations in the intensity and beam shape of the probe beam by introducing a linear slope in the model. However, sometimes the slope introduced by

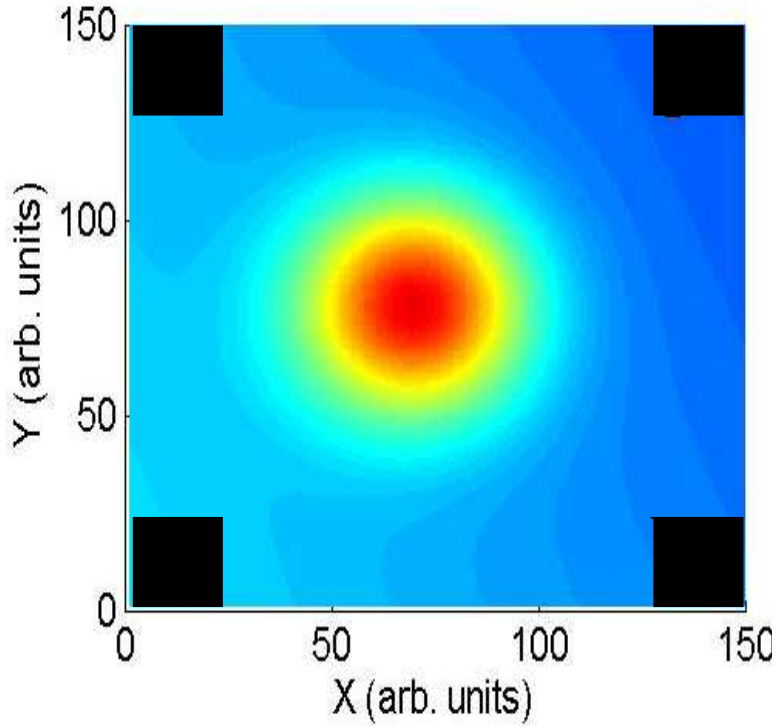

Figure 3.6: Estimating the uncertainty. In order to do a weighted fit of the optical depth, we need an estimate of the uncertainty in the plasma images. The uncertainty is estimated by finding the rms deviation in the pixel counts at the four edges of the plasma image with and without the ions.

the fluctuations is not linear. This also contributes to the χ^2 being different from 1.

A spectrum of the plasma cloud is obtained by integrating the OD of the entire cloud at different detunings of the image beam from resonance. We take images at different detunings and fit the OD to Eq. 3.22. This fit gives the value of peak OD, OD_{peak}, and the rms width of the cloud in the two axes, σ_x and σ_y, at that detuning. Then the spectrum (experimental) is obtained using

$$S_{expt}(\nu) = 2\pi\sigma_x\sigma_y OD_{peak}(\nu). \tag{3.27}$$

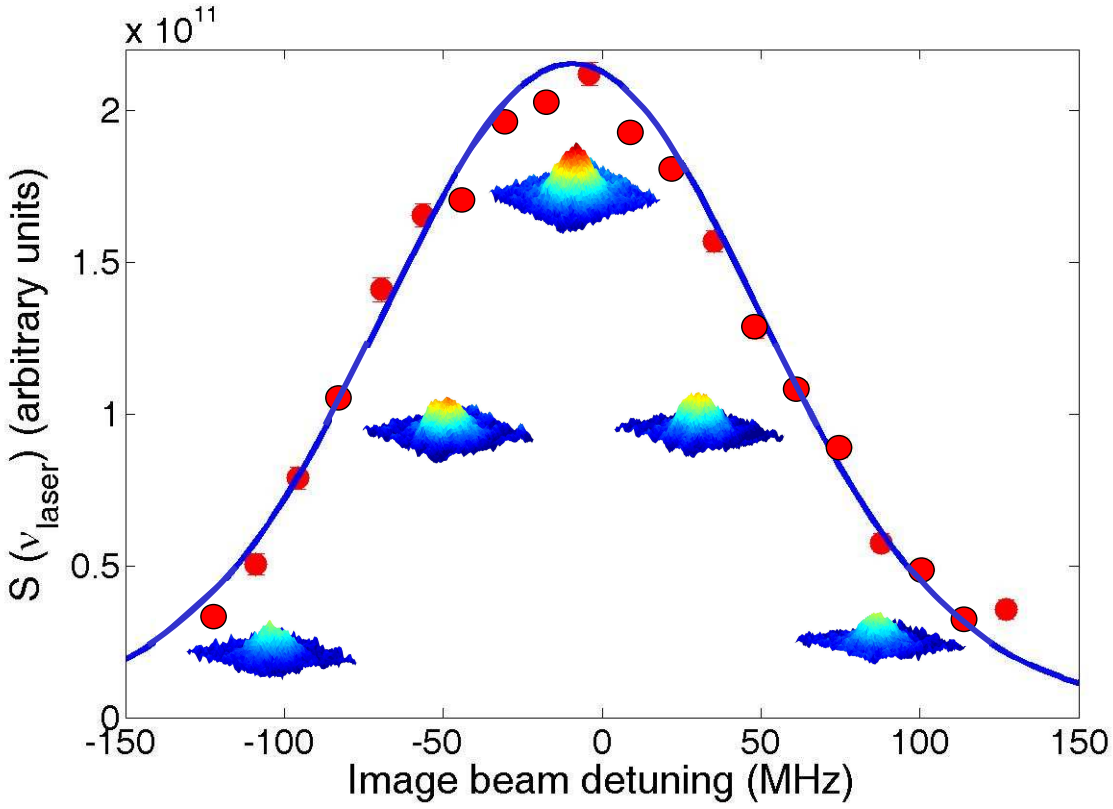

Figure 3.7: The figure shows a typical spectrum of ions along with the corresponding absorption images. The peak of the spectrum corresponds to peak optical depth which implies peak absorption cross-section. So the absorption image corresponding to the peak of the spectrum shows maximum absorption. The absorption images show decreasing absorption cross-section as you go away from resonance. This corresponds to decreasing optical depth as we go away from the peak of the spectrum.

Theoretically, an average spectrum of the plasma cloud is given by

$$S_{theory}(\nu) = \int OD(x,y)dxdy = \int n_i(r)\alpha[\nu, T_i(r)]d^3r \tag{3.28}$$

The variation of α with probe beam frequency and ion temperature is given by a Voigt profile (where the Lorentzian contribution is from the natural linewidth of the ionic transition and the image laser linewidth, and the Gaussian contribution is from

the thermal velocity of the ions, neglecting expansion of the plasma) [74]:

$$\alpha(\nu, T_i) = \frac{3^*\lambda^2}{2\pi}\frac{\gamma_0}{\gamma_{eff}}\frac{1}{\sqrt{2\pi}\sigma_D[T_i(r)]}\int_{-\infty}^{\infty} ds \frac{1}{1+\left[\frac{2(\nu-s)}{\gamma_{eff}/2\pi}\right]^2} \times \exp\left\{-\frac{(\mathrm{s}-\nu_0)^2}{2\sigma_{\mathrm{D}}^2[\mathrm{T_i(r)}]}\right\} \tag{3.29}$$

where $\lambda = 422\,\mathrm{nm}$ is the transition wavelength, $\sigma_D[T_i(r)] = \sqrt{k_B T_i/m_i}/\lambda$ is the Doppler width of the spectrum due to the ion thermal motion and $\gamma_{eff} = \gamma_0 + \gamma_{laser}$ is the effective linewidth due to the natural linewidth of the transition, γ_0, and imaging laser linewidth, γ_{laser}. (It is simple to derive that the convolution of a Lorentzian with linewidth, γ_0, with another Lorentzian with linewidth, γ_{laser}, results in a Lorentzian with linewidth, $\gamma_{eff} = \gamma_0 + \gamma_{laser}$). The center frequency of the transition is $\nu_0 = c/\lambda$. The "three-star" symbol [76] is a numerical factor that depends on the polarization state of the ions and the imaging beam. For this system, in which the ions are unpolarized while the image beam is polarized linearly, $3^* = 1$.

With no expansion, Eq. 3.29 only has a thermal width given by $\sigma_D[T_i]$ and the center frequency of the ionic transition is given by ν_0. Due to the expansion of the plasma, the resonant frequency of the ions is Doppler-shifted by v_{exp}^z/λ [77]. Substituting Eq. 3.14 into Eq. 3.7 gives the expansion velocity as $v_{exp}^z = k_B T_{e0} tz/(m_i\sigma^2(t))$, where T_{e0} is the electron temperature after thermalization and σ is the plasma cloud

size. Therefore, after including the effects of expansion, α is given by

$$\alpha_{exp}(\nu, T_i) = \frac{\lambda^2}{2\pi}\frac{\gamma_0}{\gamma_{eff}}\frac{1}{\sqrt{2\pi}\sigma_D[T_i(r)]}\int_{-\infty}^{\infty} ds \frac{1}{1+\left[\frac{2(\nu-s)}{\gamma_{eff}/2\pi}\right]^2} \times \exp\left\{-\frac{(\mathrm{s}-\nu_0-\mathrm{k_B T_{e0} tz/(m_i}\sigma^2\lambda))^2}{2\sigma_{\mathrm{D}}^2[\mathrm{T_i(r)}]}\right\} \quad (3.30)$$

When we substitute Eq. 3.30 in Eq. 3.28, we get a complicated expression for the spectrum. However, this expression can be simplified under certain assumptions. For a given ion, the total ion velocity has two components: the random thermal velocity and the directed expansion velocity. At early delay times ($< 2\mu s$) after photoionization, the thermal velocity is the dominant component but at longer delay times, the expansion velocity has a much greater contribution. The thermal velocity of the ion varies with $\vec{r}$ since the ion density varies with $\vec{r}$. So the heating due to DIH is different in different regions of the ion cloud [77]. However, on the expansion timescale, the variation of the random thermal velocity with $\vec{r}$ is negligible compared to the total ion velocity. Hence, it is assumed to be a constant over the entire cloud. This allows the density integral in Eq. 3.28 to be solved resulting in the following equation for the spectrum of the ions:

$$S(\nu) = \int dz \frac{\lambda^2}{2\pi}\frac{N_i}{\sqrt{2\pi\sigma}}\exp\left\{-\frac{\mathrm{z}^2}{2\sigma^2}\right\}\frac{\gamma_0}{\gamma_{\mathrm{eff}}}\frac{1}{\sqrt{2\pi}\sigma_{\mathrm{D}}(\mathrm{T_i})}\int_{-\infty}^{\infty}\mathrm{ds}\frac{1}{1+\left[\frac{2(\nu-\mathrm{s})}{\gamma_{\mathrm{eff}}/2\pi}\right]^2} \times \exp\left\{-\frac{(\mathrm{s}-\nu_0-\mathrm{k_B T_{e0} tz/(m_i}\sigma^2\lambda))^2}{2\sigma_{\mathrm{D}}^2(\mathrm{T_i})}\right\}. \quad (3.31)$$

Note: the ions are not in thermal equilibrium in the first microsecond of plasma evolution; however, they achieve local thermal equilibrium within the next microsecond or so (section 2.1.1).

In order to simplify the above expression, we follow a method of substitution. Let

$$\begin{aligned} \zeta &= \frac{k_B T_{e0} t z}{\lambda m_i \sigma^2} \\ d\zeta &= \frac{k_B T_{e0} t}{\lambda m_i \sigma^2} dz \end{aligned}$$

Assuming,

$$\begin{aligned} \frac{z^2}{2\sigma^2} &= \frac{\zeta^2}{2\sigma_\zeta^2} \\ \Rightarrow \sigma_\zeta &= \frac{\sigma\zeta}{z} \\ \sigma_\zeta &= \frac{k_B T_{e0} t}{\lambda m_i \sigma} \end{aligned}$$

where σ_ζ represents the width of the spectrum due to the expansion of the plasma cloud.

Eq. 3.31 can now be written as

$$S(\nu) = \int d\zeta \frac{\lambda^2}{2\pi} \frac{N_i}{\sqrt{2\pi}\sigma_\zeta} \exp\left\{-\frac{\zeta^2}{2\sigma_\zeta^2}\right\} \frac{\gamma_0}{\gamma_{\rm eff}} \frac{1}{\sqrt{2\pi}\sigma_{\rm D}({\rm T_i})} \int_{-\infty}^{\infty} {\rm ds} \frac{1}{1+\left[\frac{2(\nu-{\rm s})}{\gamma_{\rm eff}/2\pi}\right]^2} \times \exp\left\{-\frac{({\rm s}-\nu_0-\zeta)^2}{2\sigma_{\rm D}^2({\rm T_i})}\right\}. \quad (3.32)$$

Performing the dζ integration gives

$$S(\nu) = \frac{\lambda^2}{2\pi} \frac{N_i}{\sqrt{2\pi}\sqrt{\sigma_\zeta^2 + \sigma_D^2}} \frac{\gamma_0}{\gamma_{eff}} \int_{-\infty}^{\infty} ds \frac{1}{1 + \left[\frac{2(\nu - s)}{\gamma_{eff}/2\pi}\right]^2} \exp\left\{ -\frac{(\mathrm{s} - \nu_0)^2}{2(\sigma_\mathrm{D}^2 + \sigma_\zeta^2)} \right\}. \quad (3.33)$$

Hence, the width of the spectrum due to the thermal velocity of the ions and the expansion velocity add in quadrature:

$$\tilde{\sigma}_D^2 = \sigma_D^2 + \sigma_\zeta^2 \quad (3.34)$$

Finally, the spectrum of the ions is given by a Voigt profile:

$$S(\nu) = \frac{\lambda^2}{2\pi} \frac{N_i}{\sqrt{2\pi\tilde{\sigma}_D^2}} \frac{\gamma_0}{\gamma_{eff}} \int_{-\infty}^{\infty} ds \frac{1}{1 + \left[\frac{2(\nu - s)}{\gamma_{eff}/2\pi}\right]^2} \exp\left\{ -\frac{(\mathrm{s} - \nu_0)^2}{2\tilde{\sigma}_\mathrm{D}^2} \right\}. \quad (3.35)$$

Eq. 3.35 is fit to the experimentally obtained spectrum given by Eq. 3.27, with N_i, $\tilde{\sigma}_D$ and ν_0 as the fit parameters. $\tilde{\sigma}_D$ provides the information regarding the evolution of the ion total velocity.

The delay (t_{delay}) between the creation of the plasma and time of imaging can be varied to observe how the spectrum changes as the plasma evolves. The thermal pressure of the electrons accelerate the ions radially outwards [18]. This outward motion causes Doppler broadening of the ion spectrum as the velocity of the ions increase in time. Fig. 3.8 shows the spectrum at 25 ns and 3610 ns after photoionization. Due to the increase in the ion expansion velocity with time, the spectrum is much broader

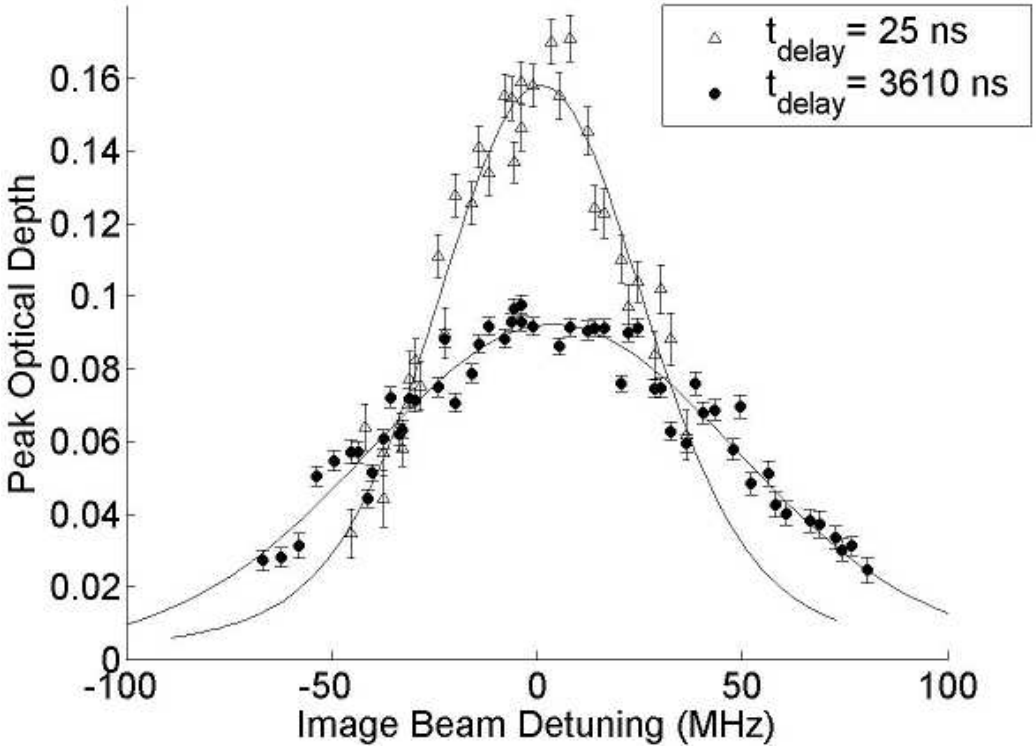

Figure 3.8: Ion spectrum at different delays after photoionization. Due to the thermal pressure of the electrons, the ions accelerate radially outwards leading to Doppler broadening of their spectrum with time. Hence, the spectrum is much narrower at 25 ns than at 3.6 μs after photoionization. As the ion cloud expands, its density decreases which lowers the peak optical depth. This figure is taken from [11].

at 3610 ns as compared to the spectrum at 25 ns delay.

The Doppler width of the ion spectrum gives us a lot of information about the temperature of the ions and electrons and the expansion velocity of the plasma. The variation in the thermal velocity of the ions over time is negligible compared to the increase in the ion expansion velocity. Hence, the ions are assumed to have a constant

thermal velocity throughout the evolution of the plasma. Under this assumption

$$\tilde{\sigma}_D = \sqrt{\sigma_\zeta^2 + \sigma_D} = \sqrt{\frac{k_B^2 T_{e0}^2 t^2}{\lambda^2 m_i^2 \sigma^2} + \frac{k_B T_i}{\lambda^2 m_i}}. \tag{3.36}$$

Note: σ_D refers to the Doppler broadening of the spectrum while σ refers to the plasma cloud size.

The size of the plasma cloud varies as (see section 3.2.1)

$$\sigma^2 = \sigma_0^2 + \frac{k_B T_{e0}}{m_i} t^2 \tag{3.37}$$

Substituting Eq. 3.37 into Eq. 3.36 and solving for $v^z = \tilde{\sigma}_D \lambda$, we get

$$v_{RMS}^z = \sqrt{\frac{k_B}{m_i} \left\{ \frac{k_B T_{e0}^2 t^2}{m_i(\sigma_0^2 + k_B T_{e0} t^2/m_i)} + T_i \right\}} \tag{3.38}$$

which is the rms total ion velocity along the z direction, which is the direction of propagation of the probe beam, henceforth referred to as the effective ion velocity.

3.3.2 Annular analysis

The absorption images of the plasma cloud give a wealth of information on the evolution of the plasma. However, to clearly observe certain aspects of plasma evolution, e.g. self-similar Gaussian expansion (Chapter 4), we require excellent spatial resolution. Hence, we resort to an annular analysis of the 2-D Gaussian images of the plasma [77].

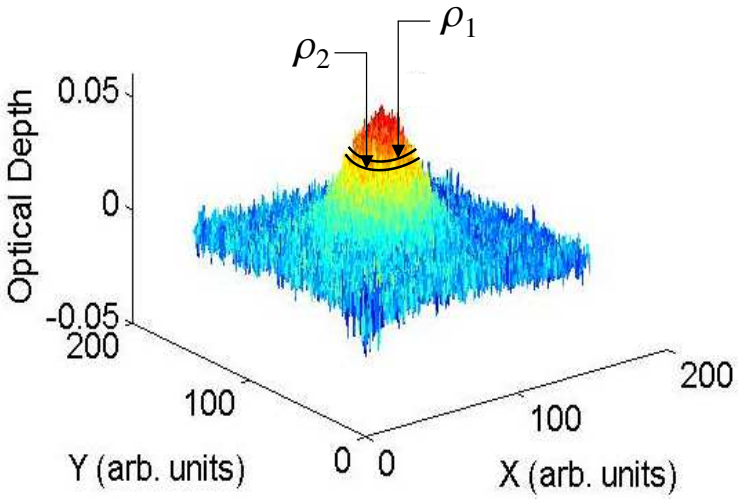

Figure 3.9: Annular analysis. Since the ion cloud has a Gaussian density distribution, we take annular sections of the cloud which are of low enough density variation to be assumed as being of constant ion density. A sample annular section is shown in the figure with inner diameter ρ_1 and outer diameter ρ_2. We fit the spectra of these regions individually to obtain the number of ions in the region as the plasma evolves.

The plasma is divided into many concentric regions whose axes pass through the plasma center parallel to the image beam as shown in the Fig. 3.9. The more number of regions we divide the image into, the better the resolution. The OD of each region is then integrated in space. A similar process is applied to plasma images at different detunings from resonance to obtain the spectrum for each region of the cloud. The spectrum is then fit to,

$$S_{reg}(\nu) = \frac{\lambda^2}{2\pi}\frac{\gamma_0}{\gamma_{eff}}\int_{-\infty}^{\infty} ds \frac{1}{1+\left[\frac{2(\nu-s)}{\gamma_{eff}/2\pi}\right]^2} \times \int_{reg} \frac{d^3r\, n(\vec{r})}{\sqrt{2\pi}\sigma_D[T_i(\vec{r})]} \exp\left\{-\frac{\left[\mathrm{s}-(\nu_0+\nu^{\mathrm{z}}_{\mathrm{exp}})\right]^2}{2\sigma^2_{\mathrm{D}}[\mathrm{T_i}(\vec{\mathrm{r}})]}\right\}. \tag{3.39}$$

to obtain the fit parameters. For more detail on the annular analysis method, please

refer to [77].

3.4 Experimental concerns

Before initiating the study of UNP expansion, it was critical to check the feasibility of being able to do these experiments with the existing experimental set up, and also determine its limitations. This check also determined the changes needed in the existing set up to allow a study of a large parameter space. One of the concerns was the Doppler broadening of the ion spectrum at long delay times after photoionization. A good measure of the spectrum including the wings would require a large frequency scan range of the probe beam. Another concern was the stray electric fields in the vacuum chamber which might tear the plasma apart. The plasma becomes more sensitive to stray fields as it expands and its Coulomb well depth decreases.

3.4.1 Maximum Doppler width

The thermal pressure of the electrons causes the ions to accelerate radially outwards resulting in an increase in the expansion velocity of the ions. This acceleration results in the Doppler broadening of the ion spectrum. In order to obtain a good spectrum, we need to scan $> 2\sigma_D$ to get the wings of the spectrum for a good fit to the theoretical model (see section 3.3.1). The maximum Doppler width for various initial plasma conditions was calculated to determine the range of initial conditions which could successfully be explored using the setup.

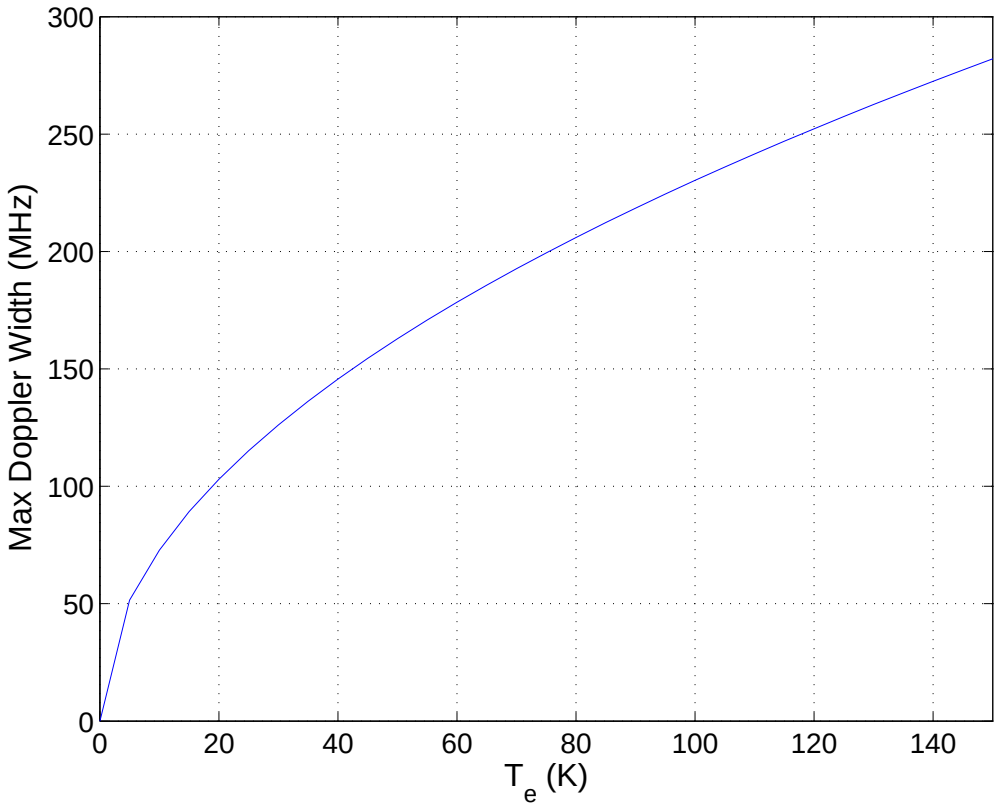

Figure 3.10: Maximum Doppler width. Figure shows the maximum Doppler width of the ultracold plasma spectrum corresponding to the maximum expansion velocity in the plasma at different initial electron temperatures for a 1 mm cloud size. The maximum expansion velocity is obtained by using the energy conservation equation.

An upperbound on the velocity distribution of the ultracold plasma for long delay times was obtained using the energy conservation equation (see section 3.2.1):

$$E_{total} = \frac{3}{2}k_B T_e(0) = \frac{3}{2}k_B(T_e(t) + T_i(t)) + \frac{3}{2}m\gamma^2\sigma^2,$$

where $\vec{v}_r = \gamma\vec{r}$ and σ is the rms size of the cloud. Since at long delay times, the electron and ion thermal energies does not contribute much to the total energy, almost all the energy in the plasma is converted to expansion energy. Hence, as a first

approximation, we can ignore the first term on the RHS of the energy conservation equation and thus find the value of $\gamma = \frac{1}{\sigma}\sqrt{\frac{k_B T_e}{m}}$. Then we can substitute this into $\vec{v}_r = \gamma \vec{r}$ and obtain v_r. However, what we measure using the optical probe beam is the z component of the ion velocity (as explained in section 3.3.1):

$$\langle v_z^2 \rangle = \int d^3r \frac{n_i(r)}{N_i} [v_r(r) cos\theta]^2, \tag{3.40}$$

where $\langle \cdots \rangle$ represents a local ensemble average and

$$n_i(r) = \frac{N}{(2\pi)^{3/2}\sigma^3} e^{-\frac{r^2}{2\sigma^2}},$$

which gives

$$\langle v_z^2 \rangle = \frac{2\pi\gamma^2}{(2\pi\sigma^2)^{3/2}} \int_0^\infty \int_0^\pi r^4 e^{-r^2/2\sigma^2} sin\theta cos^2\theta d\theta dr \tag{3.41}$$

After performing the integrations, this simplifies to,

$$\langle v_z^2 \rangle = \gamma^2\sigma^2 = \frac{k_B T_e}{m} \tag{3.42}$$

Hence the maximum Doppler width is given by

$$\sigma_{D_{max}} = \frac{1}{\lambda}\sqrt{\langle v_z^2 \rangle} = \frac{1}{\lambda}\sqrt{\frac{k_B T_e}{m}} \tag{3.43}$$

Fig. 3.10 shows the maximum Doppler width for various initial electron tempera-

tures. In order to obtain a good ion spectrum for a plasma with $T_e > 100\,K$, we need a scan range of $\sim 500\,MHz$.

A scan range as large as 500 MHz is difficult to obtain with an arrangement of acousto-optic modulators without losing too much beam power. So an offset-lock technique was used in which we locked the 844 nm diode laser at a controllable offset with respect to the 922 nm Ti:Sapph laser. The controllable offset is generated and varied using a scanning Fabry Perot interferometer. To bring the frequency of the 422 nm light close to the Sr^+ transition, the 422 nm light was sent through a rubidium absorption cell. Rubidium has three transitions close to the Sr^+ transition. These three transitions are separated by a known frequency. By scanning across these Rb transitions, we were able to calibrate the change in frequency corresponding to a known change in the offset voltage to the 844 nm laser.

One drawback of this technique is that the set up does not provide an accurate short-term lock. Therefore, it compromises the linewidth of the image beam; however, the image laser linewidth is not significant compared to the Doppler width of the ion spectrum due to expansion within a few microsecond of delay after photoionization. Hence it was ensured that the image beam can scanned far enough out from resonance to explore more than two orders of magnitude variation in electron temperature. More detail on the offset-lock circuit is available in the appendix C.

3.4.2 Electric field and potential in a UNP

Immediately after UNP formation, some of the highly energetic electrons escape leaving behind a net positive charge. The Coulomb well due to this net charge then traps the remaining electrons. As the plasma expands, the depth of the Coulomb well decreases and the ions and electrons are held together less strongly which makes them more susceptible to any external electric field. Although the vacuum chamber is grounded to the optical table, there still might be some residual stray electric fields from random stray charges inside the chamber. A good approximation is that if the stray field is an order of magnitude less than the electric field due to the excess charges in the plasma, then the plasma would not be affected significantly even at longer delay times.

The depth of the Coulomb potential well can be calculated by estimating the electric field due to the net charge in the plasma. Using Poisson's equation, and integrating over the Gaussian charge distribution, the total charge enclosed and the electric field due to this charge is given by

$$\oint E.da = \frac{Q_{encl}}{\epsilon_0} \tag{3.44}$$

or,

$$E.4\pi r^2 = \frac{1}{\epsilon_0}\int_0^r e(n_i - n_e)e^{-\frac{r'^2}{2\sigma^2}}4\pi r'^2 dr'. \tag{3.45}$$

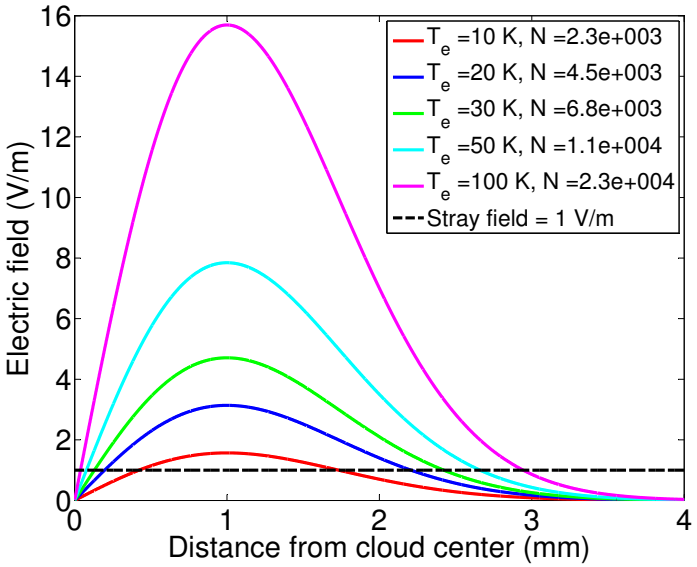

Figure 3.11: Electric Field in a UNP. The electric field with respect to distance from the center of the cloud is plotted for different electron temperatures. The field increases linearly till σ from the cloud center and then rapidly decreases as we go radially outwards. The dashed line in the figure is an arbitrary stray electric field which will be used to show the tilt in the Coulomb well due to stray fields in the chamber.

As will be shown in section 3.4.3,

$$n_i - n_e = \frac{3k_B T_e \epsilon_0}{e^2 \sigma^2} \tag{3.46}$$

(It will be shown in section 3.4.3 that the Eq. 3.46 is only valid within a few σ from the center of the cloud.)

$$E.4\pi r^2 = \frac{3k_B T_e}{e\sigma^2} 4\pi \int_0^r e^{-\frac{r'^2}{2\sigma^2}} 4\pi r'^2 dr' \tag{3.47}$$

$$E = \frac{3k_B T_e}{e\sigma^2 r^2} \int_0^r e^{-\frac{r'^2}{2\sigma^2}} 4\pi r'^2 dr' \tag{3.48}$$

The value of the electric field with respect to distance from the center of the cloud can be calculated using Eq. 3.48. The field increases with electron temperature since more number of electrons escape initially leaving a greater net positive charge in the cloud. The field decreases with increasing plasma cloud size since with larger cloud size, the net charge is spread over a large area. Fig. 3.11 shows a plot of the electric field in a UNP for different electron temperatures. The electric field increases linearly for a distance σ from the cloud center and then starts to decrease rapidly. Robicheaux *et al.* [26] did a numerical simulation of UNP expansion using the MD simulation model (see section 3.2.2) and confirmed the results of the simple calculation of the electric field shown in Fig. 3.11. They discussed the acceleration of the ions as a function of distance from the center of the plasma cloud during plasma expansion. Their results showed that the acceleration is linear with distance for a few σ from the center, after which it tends to fall off rapidly as r increases. Section 3.4.3 discusses their results in greater detail.

From the electric field, we can calculate the electric potential using

$$V = \int_0^r E.dr \tag{3.49}$$

If there are stray electric fields in the vacuum chamber, it will distort the Coulomb well and some electrons can escape from the well. Fig. 3.12 shows the tilt in the potential due to an arbitrary stray electric field (shown in Fig. 3.11). If the stray electric field is on the order of the electric field due to the net charge in the plasma, it would

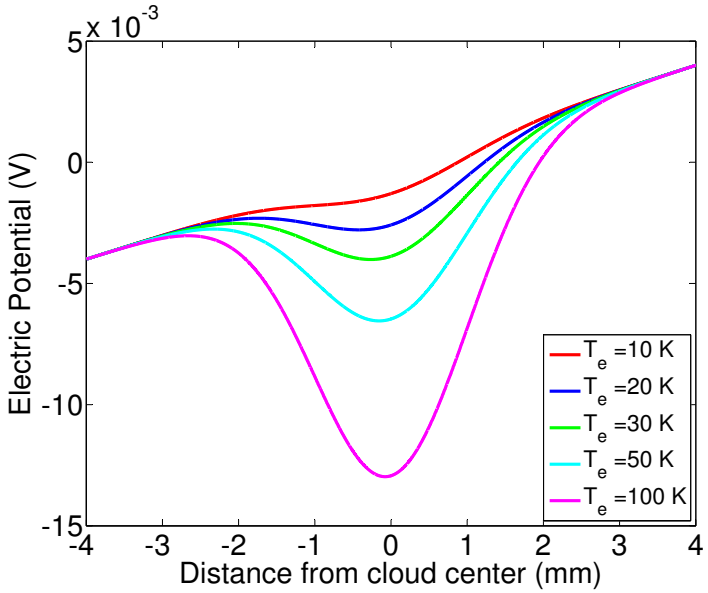

Figure 3.12: Coulomb well in a UNP. The figure shows the Coulomb potential well for various electron temperatures in a UNP. The Coulomb well tilts in the presence of a stray electric field and electrons can escape from the plasma cloud. The figure shows the tilt in the Coulomb well due to an arbitrary stray field of 1 V/m (shown in Fig. 3.11). As is evident from the figure, the effect of the stray field becomes more significant as we go to lower electron temperatures.

tear the plasma apart. Since the electric field increases with electron temperature and decreases with plasma cloud size, the upper limit on the stray field that can be tolerated in the vacuum chamber for a limiting case of plasma parameters was estimated. Fig. 3.13 shows the electric field in the UNP for an electron temperature of 1 K and plasma cloud size of 2 mm. Hence, the stray fields in the vacuum chamber need to be less than 10 mV/m in order to explore a vast range of plasma parameters.

A plot (Fig. 3.14) of the potential well for various initial conditions shows that the depth of the well in units of $3k_BT_e/2e$ is always -1. This universal value implies that the depth of the potential well is always on the order of the initial electron energy. This becomes obvious from the following explanation: a UNP keeps losing electrons

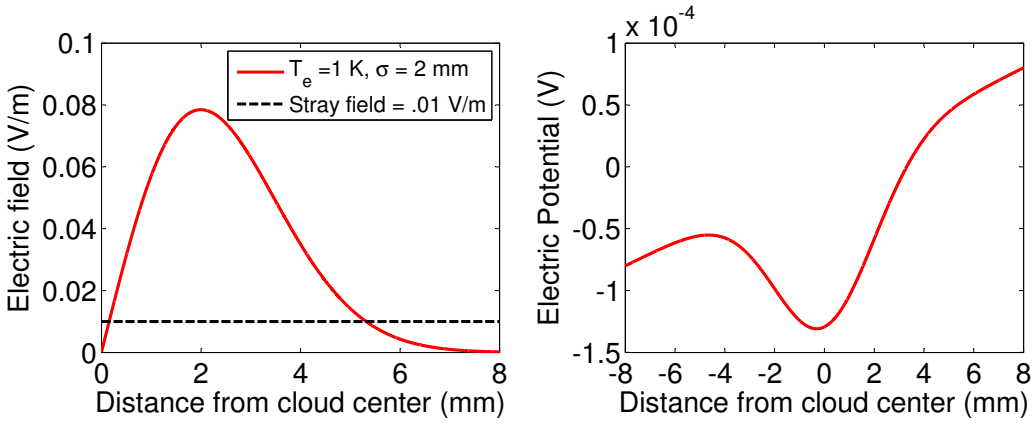

Figure 3.13: Figure shows the electric field and Coulomb potential well for a limiting case of plasma parameters. When the stray fields are on the order of the electric field due to the net positive charge in a UNP, it tears the UNP apart. The stray fields in the vacuum chamber should be less than 0.01 V/m to study cold electron temperature plasmas with large cloud size.

until the Coulomb well depth is greater than the thermal energy of the remaining electrons. Hence, Fig. 3.14 is a universal curve.

Possible sources of stray charges in the vacuum chamber creating the stray electric field could be charges released from the UNP which have stuck to the inner surface of the vacuum chamber and static charges on the glass windows. In order to remove any stray charges stuck to the vacuum chamber, the chamber was flushed with Argon and then brought down to vacuum again. All the glass windows in the vacuum chamber were moved far from the center of the chamber to reduce the effect of static charges that build up on glass surfaces. In addition to that, two segmented Copper plates were put in the vacuum chamber to counteract the effect of any stray fields that might build up due to stray charges [78]. The system was tested to determine the stray fields that might be present in the vacuum chamber by applying different voltages to the different segments of the Copper plates and observing the effect on the plasma cloud.

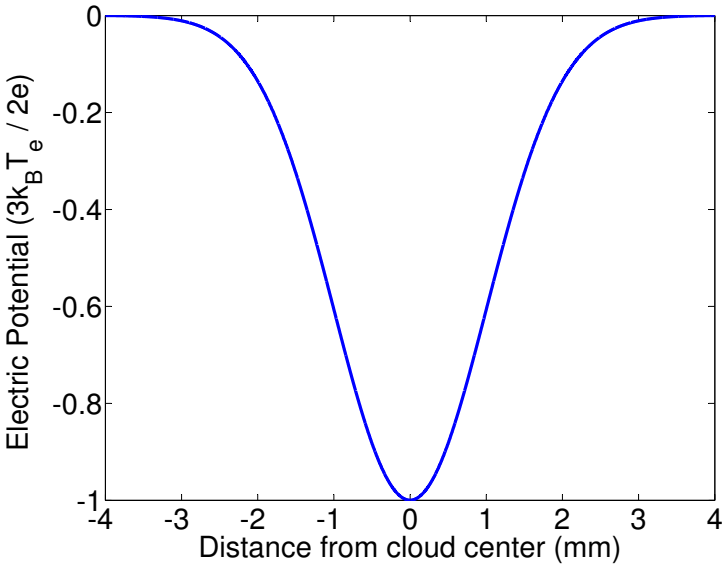

Figure 3.14: The Coulomb potential well curve in units of electron energy is a universal curve. It shows that electrons are lost from a UNP until the Coulomb well depth exceeds the thermal energy of the electrons.

There was no detectable effect on the cloud. So the Copper plates were grounded as a feature to add more protection against stray fields in the chamber.

3.4.3 Quasineutrality

Quasineutrality refers to the condition in which $n_e \approx n_i$ in a plasma. Quasineutrality is only valid if the length scale for the ion density variation exceeds the local Debye screening length [27, 72, 79], or $\sigma \gg \lambda_D(r)$ for a Gaussian plasma. The concept of quasineutrality is important because an exact analytical solution to a self-similar Gaussian plasma expansion exists in the quasineutral limit [70, 71, 80].

The extent of non-neutrality ($n_i - n_e = \delta_e$) in the plasma is determined with the

help of Eq. 3.4 [56]. Using Poisson's theorem,

$$\begin{aligned} E(r) &= \frac{Q_{enclosed}(r)\hat{r}}{4\pi\epsilon_0 r^2} \\ &= -\frac{e}{4\pi\epsilon_0 r^2}\int_0^r dr_1 4\pi r_1^2(n_i - n_e) \end{aligned} \tag{3.50}$$

Now using Eq. 3.4 we get,

$$\begin{aligned} \frac{n_e e^2}{4\pi\epsilon_0 r^2}\int_0^r dr_1 4\pi r_1^2(n_i - n_e) &= -k_B T_e \frac{dn_e}{dr} = k_B T_e n_e \frac{r}{\sigma^2} \\ \int_0^r dr_1 r_1^2(n_i - n_e) &= \frac{k_B T_e \epsilon_0}{e^2}\frac{r^3}{\sigma^2} \\ r^2(n_i - n_e) &= 3\frac{k_B T_e \epsilon_0}{e^2}\frac{r^2}{\sigma^2} \\ \delta_e &= 3\frac{k_B T_e \epsilon_0}{e^2\sigma^2} \\ \frac{\delta}{n_e} &= 3\frac{\lambda_D^2(r)}{\sigma^2} \end{aligned}$$

The fractional non-neutrality is small as long as $\lambda_D << \sigma$ which is true within a few σ from the center of the UNP, hence it is quasineutral. (Typically, $\lambda_D = 1 - 20\,\mu m$ and $\sigma = 0.7 - 1.5\,mm$ in the UNPs in this study)

In a quasineutral system, the mean electric field can be expressed as [56],

$$E = -k_B T_e \nabla n_i / e n_i \tag{3.51}$$

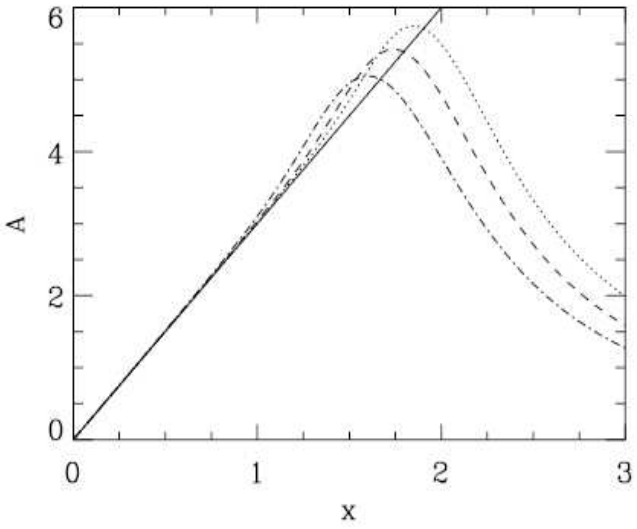

Figure 3.15: This figure is taken from Robicheaux *et al.* [27]. Using a molecular dynamic simulation model, they simulated the expansion of an ultracold neutral plasma. The figure shows the scaled radial acceleration A versus the scaled radial distance x = $r/\sqrt{< r^2 >}$ for electron temperatures of 15 K (dotted line), 30 K (dashed line), and 75 K (dot-dashed line). They key point to note in this figure is that the acceleration is linear till ∼1.5x so the plasma is quasineutral within that radial distance only.

which in a Gaussian system leads to a force on the ions of

$$\vec{F}(t) = \frac{k_B T_e(t)\vec{r}}{\sigma(t)^2}. \tag{3.52}$$

Eq. 3.52 implies unphysical forces at large r. Since there is some loss of electrons from the edges of the plasma immediately after plasma creation (section 1.2.3), a UNP is quasineutral only within a radius of a few σ [27], where the accelerating electric field reaches a maximum of $\sim k_B T_e/e\lambda_D$ [37, 81]. Hence Eq. 3.52 does not hold true for a UNP at large r.

For all the data that will be discussed in chapters 4 and 5, only an 'inner region' of the plasma cloud is analyzed where the 'inner region' extends to $r = 1.5\sigma$. Fig.

3.15 [27] shows that the force is linear with r only for $r/\sqrt{< r^2 >} \sim 1.5$. Now,

$$< r^2 >= \frac{\int_0^\infty r^2.4\pi r^2 e^{r^2/2\sigma^2} dr}{\int_0^\infty 4\pi r^2 e^{r^2/2\sigma^2} dr} = 3\sigma^2$$

$$\frac{r}{\sqrt{< r^2 >}} = \frac{r}{\sqrt{3}\sigma} \sim 1.5$$

Hence, the force is linear with r only till $r \sim 2.5\sigma$. By analyzing only the 'inner region', it was ensured that the plasma cloud in this study is quasineutral.

A significant feature of plasma expansion is shock waves. Shock waves appear due to the difference in the velocity of ions in different regions of the plasma. As shown in Fig. 3.15, the ion acceleration increases linearly from the center of the plasma until it decreases as $1/r^2$ near the edge. This behavior causes some ions at inner side of the edge of have a higher velocity than the ions at the outer side of the edge. At some point during the plasma evolution, these inner side ions catch up with the outer side ions and cause a density spike. This spike produces a shock wave. Since the signal to noise degrades strongly towards the edge of the UNP, no shock waves were observed. For more details on shock waves in UNPs, please refer to Sampad Laha's dissertation [54].

Chapter 4

Self-similar Gaussian Expansion

Self-similar Gaussian expansion means that if you start with a quasineutral, Gaussian plasma, then as the plasma expands, it continues to have a Gaussian density distribution. This type of expansion has been studied by many theorists [70–72] for hot plasmas. The self-similar expansion is due to the fact that the force as given by Eq. 3.5 varies linearly with $\vec{r}$. This type of expansion connects UNPs to the traditional hot plasmas.

The evolution of a plasma can be described by Vlasov equations. These equations have an exact analytical solution if the plasma cloud remains an adiabatic system as it evolves. As explained in section 3.2.1, for an ion initially at rest such that $T_i(0) = 0$,

$$\vec{u}(\vec{r},t) = \langle \vec{v}_i(\vec{r},t) \rangle = \frac{k_B T_{e0}}{m_i} \frac{t\vec{r}}{\sigma(t)^2}, \tag{4.1}$$

where $\langle \cdots \rangle$ refers to a local ensemble average. For self-similar expansion, the characteristic plasma size follows [56, 71, 72]

$$\sigma(t)^2 = \sigma_0^2 + \frac{k_B T_{e0}}{m_i} t^2 \tag{4.2}$$

and

$$\sigma(t)T_e(t) = \sigma_0 T_{e0} \tag{4.3}$$

Eq. 4.3 implies that the electrons undergo adiabatic cooling as the plasma expands. Using Eq. 4.3 and 4.2, the electron temperature evolution is given by

$$T_e(t) = \frac{T_{e0}}{(1 + \frac{k_B T_{e0}}{m_i \sigma_0^2} t^2)^{1/2}}. \tag{4.4}$$

Eqs. 4.1, 4.2 and 4.4 form the complete solution to the Vlasov equations. [Note that if the ions were not at rest initially, we would have to add T_i as shown in Eq. 3.17 to get the correct expressions. While the ions are not at rest initially in these experiments, the assumption that $T_i(0) = 0$ is justified since $T_i << T_{e0}$.] The analytic solution makes it convenient to verify the experimental results against theory. Similarly, realizing the solution experimentally helps confirm the theoretical predictions. The beauty of UNPs lies in the fact that since they expand on a microsecond timescale, it is easy to study their evolution experimentally with great temporal resolution. The experimentally measured evolution is then matched against the theory to show that UNPs undergo self-similar Gaussian expansion under certain initial conditions.

A clean and simple plasma expansion, with electron temperature evolution as given in Eq. 4.4, requires that there is no external source of heat during the expansion such that the system remains adiabatic. As explained in section 2.2, there are many processes that heat the electrons and complicate the plasma expansion. In order

to turn off these heating processes, we need to be in a region of parameter space in which effects such as TBR and R-e are insignificant. Since the rate of TBR $\propto T_e^{-9/2} n^3$, the effect of TBR (and subsequently R-e) can be minimized by high initial electron temperature and low density. Under these conditions, the effect of TL and DIH also become negligible. Hence, if we start with relatively high initial electron temperature and low density, a freely expanding, quasineutral Gaussian UNP undergoes self-similar Gaussian expansion.

There are many parameters which can be used to check if UNP undergoes self-similar Gaussian expansion. However, depending on the sensitivity of the probe, some parameters can be measured with greater precision than others. In order to determine if the plasma cloud undergoes self-similar Gaussian expansion, we can either check to see if the cloud fits well to a Gaussian profile as it expands, or we can verify it by fitting the plasma evolution to Eqs. 4.1 or 4.2.

4.1 Plasma remains Gaussian as it expands

Self-similar Gaussian expansion implies that the plasma retains its Gaussian distribution as it expands. As a preliminary test of the density distribution of the plasma cloud, linear cross-sections of the spherical cloud are taken and fit to a one dimensional Gaussian distribution.

The optical depth of the plasma images are recorded in the form of a square matrix. An average of the optical depth of the plasma in the three centermost columns (to get

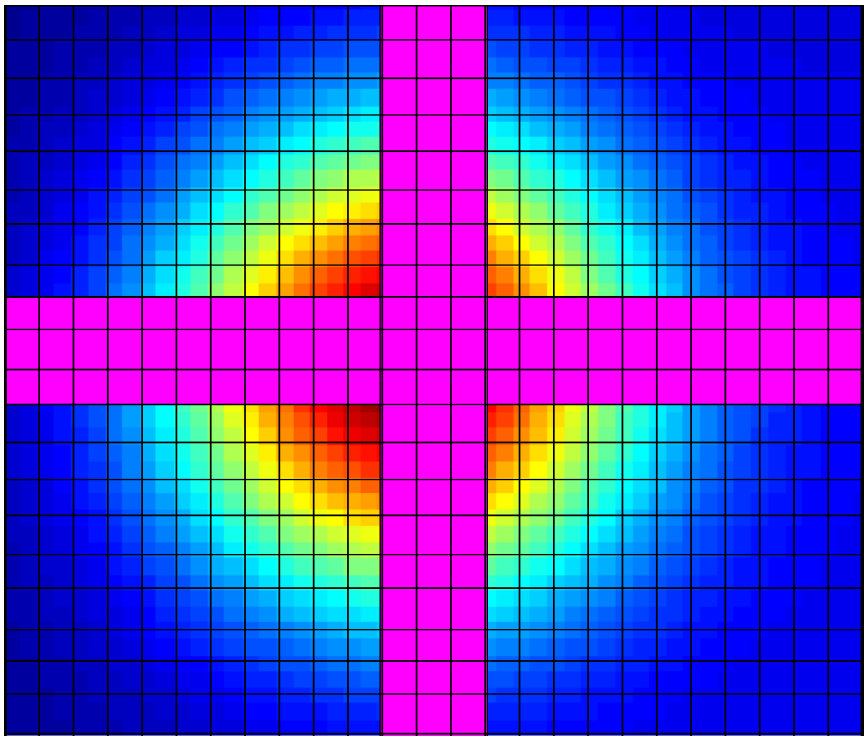

Figure 4.1: The figure shows how linear cross-sections of the plasma image are taken. A typical data set is recorded in the form of a matrix of pixel counts. In order to test whether a plasma remains Gaussian as it expands, linear cross-sections of the plasma image in the two dimensions are fit to a 1-D Gaussian distribution. These linear cross-sections correspond to columns and rows in the matrix of pixel counts. An average of 3 columns and 3 rows is taken for better statistics. The figure is not drawn to scale.

better statistics) of the matrix is taken. Similarly, an average of the optical depth in the three centermost rows is taken. Fig. 4.1 shows the plasma image in the form of a matrix. The color in the image is a representative of the optical depth of the plasma cloud, with red being the peak optical depth and blue implying the lowest optical depth. The area shaded in pink gives a depiction of the three centermost columns and rows from the image matrix which are used to obtain the averages. The pixel size on the camera is $11.9\,\mu m$, hence an average of three rows or columns implies averaging over $35.7\,\mu m$ of the image. These average optical depths are then fit to

a one dimensional Gaussian. Fig. 4.2 shows the optical depth along with the fit for various delays after photoionization for a UNP with initial electron temperature of 14 K and initial peak density of $3*10^{15}\,m^{-3}$. The fits show that as the plasma evolves, it fits well to a Gaussian density distribution at all delays after photoionization. The assumption of a constant absorption cross-section throughout the cloud affects this analysis adversely. In addition to that, there is non-statistical noise in the data. Hence, the weighted χ^2 are different from 1. Therefore, this is not a definitive method of verifying self-similar Gaussian expansion. [Note: A close look at Fig. 4.2 shows that the area under the Gaussian curve is decreasing with time. This is due to a loss in the number of ions because of collisions with a hot atomic beam during plasma expansion (for more details, refer to appendix A). This loss was identified as a one-body loss, and does not affect the results presented in this chapter.]

A more sophisticated approach would be to employ the annular analysis technique (section 3.3.2) to check if the ion density distribution fits $n_i(r) = n_0 exp(-r^2/2\sigma^2)$ at all delays after photoionization. Annular analysis allows us to obtain the spectrum of different cylindrical regions of the cloud. From the spectra, we can obtain the number of ions, N_i, in each region which when divided by the area of each cylindrical region, gives the areal density, n_{areal}, of the cloud. We can fit this n_{areal} to a Gaussian density distribution. The annular analysis verified that a quasineutral, Gaussian UNP undergoes self-similar Gaussian expansion. For greater detail on this scheme, refer to [77]. This method will also be covered in Sampad Laha's dissertation [54].

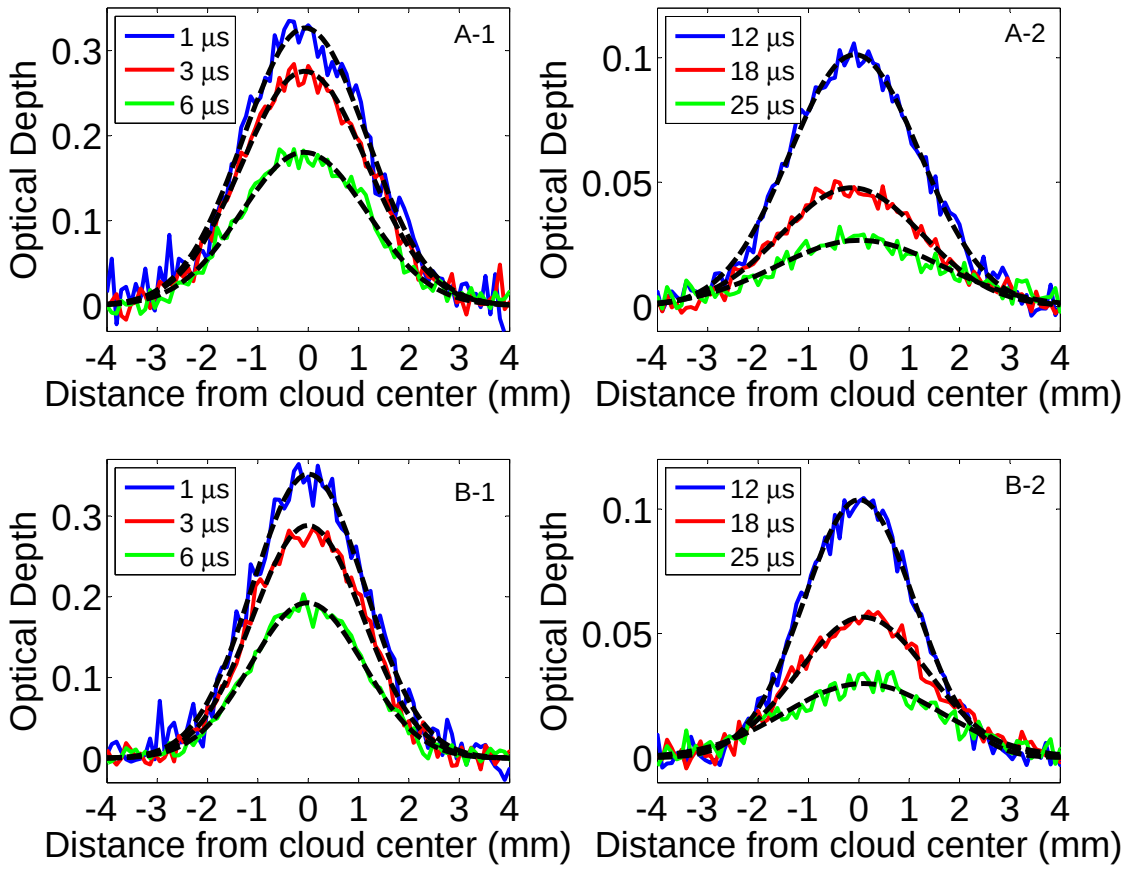

Figure 4.2: The figures A and B show the optical depth of the plasma in the two orthogonal axes for various delays after photoionization. The data is fit to a one dimensional Gaussian (dashed line) to show that the density distribution remains Gaussian as the plasma evolves.

4.2 Effective ion velocity evolution

The effective ion velocity is measured with great resolution and accuracy. The effective velocity has contributions from the random thermal velocity of the ions and the radially directed expansion velocity. As explained in section 3.3.1, we can analyze the ion spectrum for various delays after photoionization and obtain the Doppler width of the cloud. From the Doppler width, we get an effective ion rms velocity

using

$$v_{z,RMS} = \sigma_D \lambda \tag{4.5}$$

where $\lambda = 422\,nm$. Note that since the effective velocity of the ions is measured along the direction of propagation of laser, the measurement gives the value of $v_{z,RMS}$. Since the plasma cloud is isotropic,
$v_{RMS} = \sqrt{v_{x,RMS}^2 + v_{y,RMS}^2 + v_{z,RMS}^2}$.

The next step is to derive the velocity evolution of the cloud using the analytical solutions of the Vlasov equations to test if the experimental measurements of the velocity evolution fits the model. As explained in chapter 3, the velocity of the plasma cloud is directed radially outwards and $\vec{v} \propto \vec{r}$. For a Gaussian distribution, this implies that an ion at $r = \sigma$ will always remain at σ as the cloud expands. Also, since $\vec{v} \propto \vec{r}$, let us assume that $v = Kr$ where K is some constant,

$$\begin{aligned} v_i &= Kr_i \\ \Sigma_i v_i^2 &= \Sigma_i K^2 r_i^2 = K^2 \Sigma_i r_i^2 \\ \sqrt{\frac{\Sigma_i v_i^2}{\Sigma_i i}} &= \sqrt{\frac{\Sigma_i K^2 r_i^2}{\Sigma_i i}} = K\sqrt{\frac{\Sigma_i r_i^2}{\Sigma_i i}} \\ v_{RMS} &= Kr_{RMS} \end{aligned} \tag{4.6}$$

which implies that the rms velocity of an ion is equal to the velocity of the ion at the

rms width of the cloud, σ. Using Eq. 3.5, this gives

$$v_{RMS} = \int \frac{k_B T_e(t)}{m_i \sigma(t)} dt. \tag{4.7}$$

Substituting the electron temperature evolution, Eq. 4.4, and the ion cloud size evolution, Eq. 4.2, into Eq. 4.7 we get the rms expansion velocity of the ions for an adiabatically expanding plasma as

$$v_{exp} = \frac{k_B T_{e0} t}{m\sigma_0^2 \sqrt{1 + \frac{k_B T_{e0}}{m\sigma_0^2} t^2}} \tag{4.8}$$

Experimentally, the combined effect of the directed expansion velocity as well as the random thermal velocity of the ions along the z direction is measured. As shown in section 3.3.1, these two add in quadrature. Hence,

$$v_{z,RMS} = \sqrt{\frac{k_B}{m_i} \left(\frac{\frac{k_B T_{e0}^2}{m_i \sigma_0^2} t^2}{1 + \frac{k_B T_{e0}}{m_i \sigma_0^2} t^2} + T_i \right)}. \tag{4.9}$$

The experimental effective ion velocity evolution, which is the ion rms velocity, is fit to Eq. 4.9 with T_{e0} and T_i as the fit parameters where T_{e0} is the initial electron temperature and T_i is the temperature of the ions at $t = 0$. The initial size of the cloud, σ_0 is determined from the 2-D Gaussian fit and is treated as an input variable. According to Eq. 4.9 the rate of plasma expansion is greater when we start with a small cloud size and high initial electron temperature. Fig. 4.3 shows the ion velocity

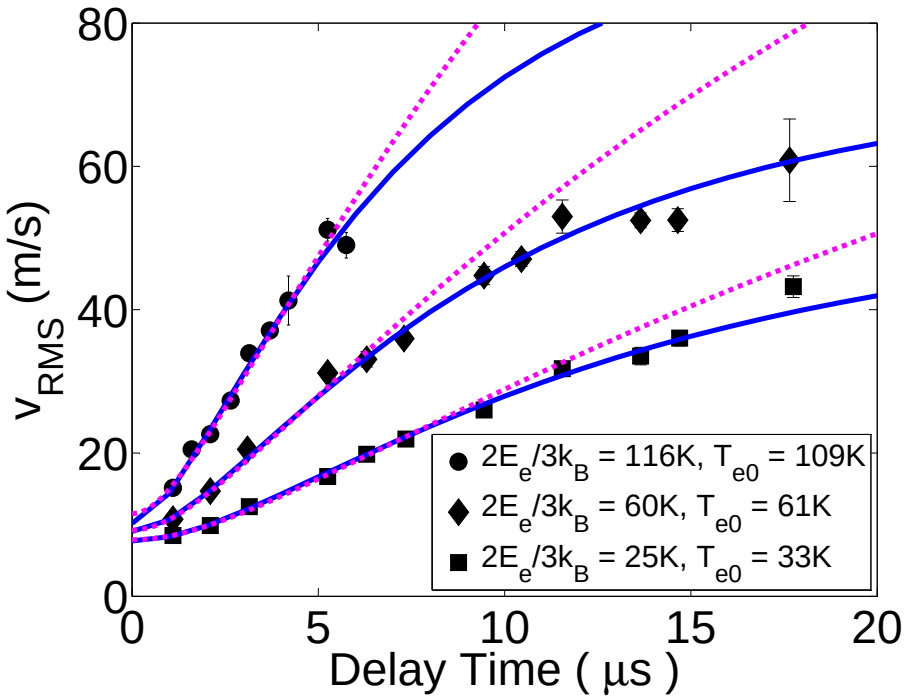

Figure 4.3: The figure shows data with $2E_e/3k_B = 116$, 60 and 25 K. The density of the plasma $n_0 = 3.5 * 10^{15} m^{-3}$ and initial size $\sigma_0 = 1mm$. The solid line is a fit of the data to the adiabatic electron temperature cooling model. At high initial electron temperatures, there is no or insignificant heating due to the various collisional processes in a UNP so $T_{e0} \approx 2E_e/3k_B$ for the 116 and 60 K data, within the uncertainties. For 25 K data, though, $T_{e0} > 2E_e/3k_B$ suggesting that some of the electron heating process are starting to become significant and so the plasma does not undergo a purely adiabatic expansion. The dashed line is a fit to the constant electron temperature model, which does not fit the 25 K and 60 K data. It fits the 116 K data; however, not enough data points were taken to distinguish the two models.

evolution for three datasets with peak density, $n_0 = 3 * 10^{15}\, m^{-3}$ and initial size, $\sigma_0 = 1\, mm$ and initial electron temperatures of 25 K, 60 K and 116 K. The figure shows a greater rate of expansion for a greater initial electron temperature. Since both the initial electron temperature and the initial cloud size are well within our experimental control, the rate at which the plasma will expand can be pre-determine and set according to the needs of the study. However, this is only true if the plasma expands

adiabatically and if there are no density dependent processes dominant during the evolution.

The solid lines in Fig. 4.3 shows the adiabatic electron temperature cooling fits to three datasets, essentially the fit to Eq. 4.9. Note that in all the figures, the v_{RMS} refers to the effective ion velocity along the direction of propagation of the probe beam. The initial offset in v_{RMS} in the figure is due to disorder-induced heating. This effect rapidly heats the ions from their initial temperature of a few millikelvin to $\sim$1 K. The adiabatic electron temperature cooling model does not determine the increase in the ion kinetic energy with time due to DIH within the first microsecond. The initial velocity of the ions at $t = 0$ in Eq. 4.9, is the ion random thermal velocity. This approach does not disturb the results for the expansion of the UNP since the details of the evolution of the ions within the first microsecond to reach the value of T_i does not affect the evolution of the effective ion velocity at later delay times. The quadratic increase during the first ~ 5 μs reflects constant acceleration before either σ or T_e changes appreciably. Then as σ increases (Eq. 4.2) and T_e drops (Eq. 4.4) due to adiabatic cooling, there is an inflection in the curve indicating decreasing force on the ions. During the expansion, the electron kinetic energy is transferred to the ions in the form of expansion energy. When essentially all the electron energy gets converted to the expansion energy, the ion expansion velocity rolls off as the ions reach terminal velocity [18]. For relatively higher initial electron temperatures, as shown in Fig. 4.3, the ions expand rapidly. As a result, observing the rollover of the

velocity is a challenge due to decrease of signal to noise with time.

As shown in the figure, the experimental data fits the theoretical model for adiabatic expansion well. Reported in the figure is also the value of the fit parameter T_{e0}. For an adiabatic expansion in which inelastic collisions, resulting in electron heating, are negligible, the T_{e0} should equal the initial electron temperature set by the energy of the ionizing photon. From the adiabatic electron temperature cooling fit,

$2E_e/3k_B$ (K)	T_{e0} (K)
116	109 ± 4
60	61 ± 1
25	33 ± 1

The initial electron temperature, $2E_e/3k_B$, has an uncertainty of $\pm 3\,K$. Within the uncertainties, $T_{e0} \approx 2E_e/3k_B$ for the 116 K and 60 K data, proving that UNP with high initial electron temperature expands adiabatically. For the 25 K data, though, $T_{e0} > 2E_e/3k_B$ significantly enough to suggest that some electron heating processes are starting to become non-negligible.

The 116 K and 60 K datasets show that this is the simplest form of UNP expansion with no external source of heating. This is a region of parameter space in which the UNP expansion is described by an exact analytical solution to the Vlasov equations which are used to describe the dynamics of a wide range of plasmas. Note that there is a $\sim \pm 3\,K$ uncertainty in the estimation of $2E_e/3k_B$ due to the dye laser linewidth, the wavelength calibration of the output of the dye laser, and the uncertainty in the movement of the counter that tunes the wavelength of the dye laser. (Please refer to

my Master's thesis [51] and appendix B for more detail on how this uncertainty is determined.)

To test the sensitivity of v_{RMS} to different evolutions of T_e, Eq. 4.7 is solved with T_e constant with delay after photoionization. The equation does not have an analytic solution so it was solved numerically. This model is referred to as the constant electron temperature evolution model. The dotted line in Fig. 4.3 shows the numerical solution to the constant electron temperature evolution fit. The overlap of the adiabatic electron temperature cooling fit and the constant electron temperature fit in the first $5\,\mu s$ for all three datasets indicates that the change in the electron temperature in the first few microseconds is not significant. Thus, the probe is not sensitive enough to separate the two models at these early times. However, at later delay times, the two fits start to deviate from each other, clearly showing that the adiabatic electron cooling evolution fits the data better.

An additional study was to test the sensitivity of the fit to electron temperature evolution model at delay times $\geq 10\,\mu s$ where the signal to noise is poor due to loss of ions (see appendix A). So I fit the data using Eq. 4.7 with an electron temperature evolution such that the electrons adiabatically cool for the first $11\,\mu s$ and then the temperature is held constant for the rest of the plasma evolution. Fig. 4.4 shows one such data set with a fit to the adiabatic electron temperature cooling model shown by a solid line. The dashed line shows a fit to the adiabatic electron temperature cooling model till $t = 11\,\mu s$ and then to a constant electron temperature model. The

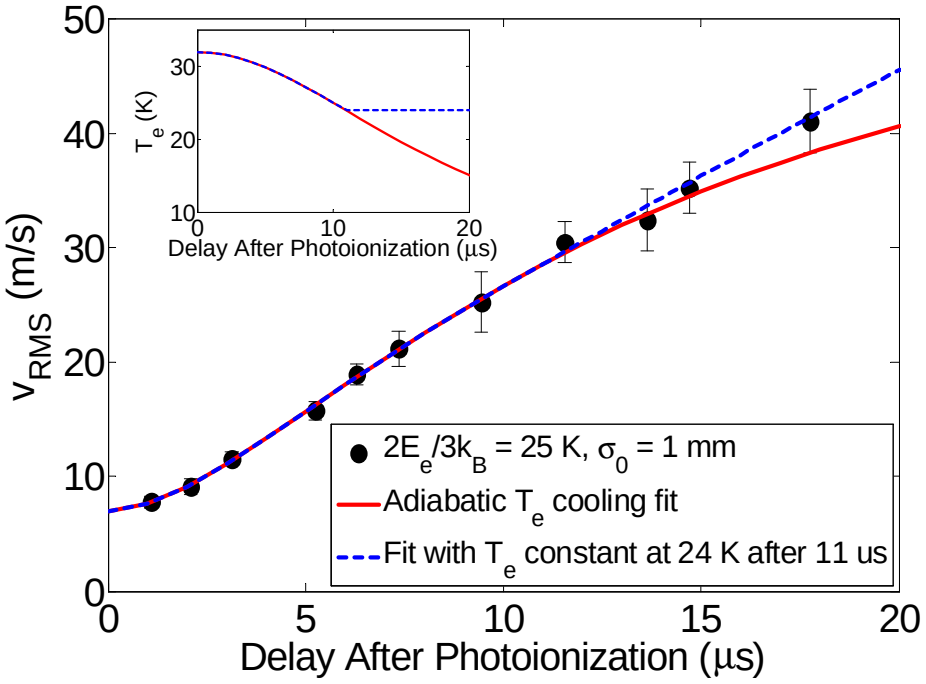

Figure 4.4: The figure shows data with $2E_e/3k_B = 25\,\mathrm{K}$. The density of the plasma $n_0 = 3.5 * 10^{15} m^{-3}$ and initial size $\sigma_0 = 1mm$. The solid line is a fit of the data to the adiabatic electron temperature cooling model. The dashed line is a fit to the model in which the effective ion velocity evolves according to the adiabatic electron temperature cooling model for the first $11\,\mu s$ and thereafter according to the constant electron temperature model. The electron temperature is assumed constant at its value at $11\,\mu s$ according to the adiabatic electron temperature cooling model. The inset shows the electron temperature evolution corresponding to the two fits. The figure shows that it is difficult to make any definite statements regarding the T_e evolution for delay times $> 11\,\mu s$ due to few number of data points and noise in the data.

electron temperature is assumed constant at its value at $11\,\mu s$ calculated from the adiabatic electron temperature cooling model. The inset shows the electron temperature evolution for the two models. For the adiabatic electron temperature cooling model, the electron temperature is plotted according to Eq. 4.4, where T_{e0} is obtained by minimizing the χ^2 for the effective ion velocity evolution using Eq. 4.7. The figure shows that it is difficult to distinguish definitely between the two fits due to very few

data points and poor signal to noise. We cannot rule out the possibility that processes such as TBR might become significant at later delay times when the electrons have cooled down due to adiabatic expansion. Such heating processes might hold the electron temperature constant or even increase the electron temperature at long delay times.

Since the rate of expansion of the plasma depends strongly on the electron temperature, the ion spectrum is Doppler broadened rapidly for higher initial electron temperatures requiring large image beam frequency scans. We are limited in the maximum initial electron temperature we can explore in a UNP due to the dependence of the initial loss of electrons immediately after photoionization on the initial electron temperature. For very high initial electron temperature, a lot of electrons are lost initially, before the Coulomb well, which is formed from the net positive charge, is able to trap the rest of the electrons. This loss of electrons leads to greater non-neutrality in the plasma for higher initial electron temperature, and the quasineutral approach to determine the expansion is no longer valid. In addition to that, the plasma expands more rapidly for higher initial electron temperature, implying that for a given delay after photoionization, the Doppler broadening is greater, requiring a greater frequency scan range of the probe beam to get a good spectrum. We have limited scan range capabilities which limits us to explore UNP expansion for a maximum initial electron temperature of a few hundred Kelvin. Despite the limitations, a region of parameter space in UNPs was determined in which the expansion can be described

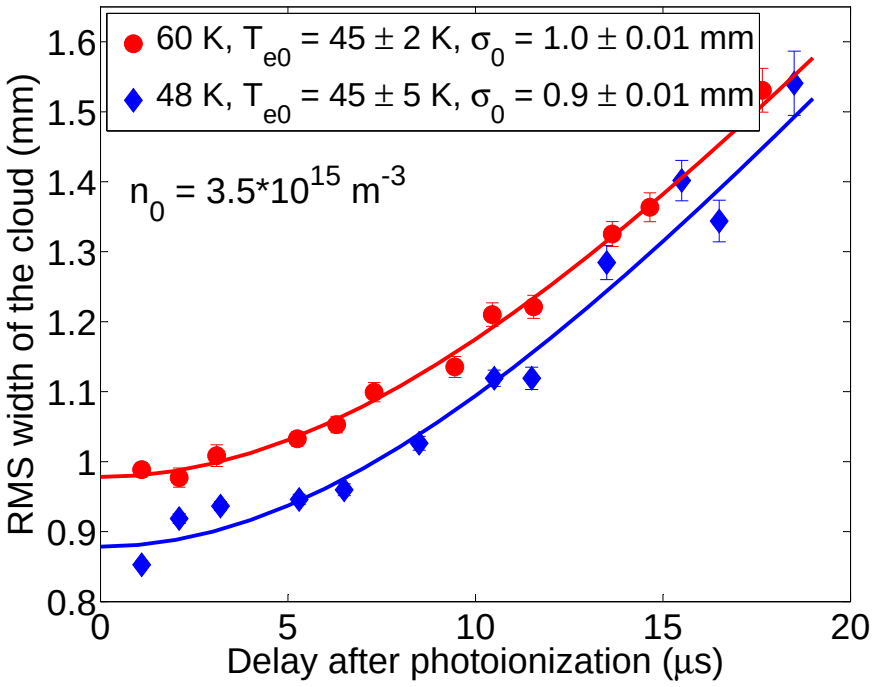

Figure 4.5: The plasma cloud size evolution is plotted for $2E_e/3k_B = 60$ and 48 K. The size evolves more rapidly for higher initial electron temperature and low initial cloud size. The two effects balance each other in the datasets shown in the figure such that the size of the cloud with $2E_e/3k_B = 48\,K$ catches up with the size of the cloud with $2E_e/3k_B = 60\,K$ in $\sim 20\,\mu s$. The data is fit to the solution of the Vlasov equation which describes the size evolution. While the fits look good, for the 60 K data, we expect $T_{e0} \approx 60\,K$ but inexplicably, $T_{e0} = 45\,K$.

by the analytic solution of the Vlasov equations. This facilitated verification of the theoretical work that has been done on plasma expansion in the last few decades.

4.3 Ion cloud size evolution

For a self-similarly expanding quasineutral Gaussian plasma, the size of the cloud should evolve as given by Eq. 4.2. Hence, another method to test if UNP undergoes self-similar Gaussian expansion is to test if its size does evolve according to Eq. 4.2.

The optical depth of the plasma is fit to a two dimensional Gaussian distribution as explained in section 3.3.1. This fit gives the rms width of the cloud, σ_x and σ_y, in the two dimensions. The plasma cloud size in the two dimensions is compared to the atom cloud size to ensure even illumination of the atom cloud from the optical pumping and photoionizing beam. With the help of two cameras placed on orthogonal axes, it is ensured that $\sigma_x = \sigma_y$ and $\sigma_x = \sigma_z$. This confirmed that the spherically symmetric Gaussian approximation for the plasma evolution can be used in this study.

The plasma size evolution is fit to Eq. 4.2 with T_{e0} and σ_0 as the fit parameters. Fig. 4.5 shows a plot of the size evolution along with a fit to Eq. 4.2 for a UNP with density, $n_0 = 3.5 * 10^{15}\, m^{-3}$ and initial electron temperatures of 60 and 48 K. The figure also shows the fitted values of T_{e0} and σ_0 for the two initial conditions. While the value of $T_{e0} = 45 \pm 5\, K$ is consistent with $2E_e/3k_B = 48\, K$, the value of T_{e0} for $2E_e/3k_B = 60\, K$ does not make sense.

While the data fits well to Eq. 4.2, the cloud size measurement is not the most sensitive measurement in this study. The signal to noise degrades tremendously before there is enough variation in the cloud size to concretely establish the fit with acceptable amount of uncertainty in the fit parameters. The signal to noise degrades due to the loss in ion number with delay after photoionization due to collisions with hot atoms (see appendix A). For some set of initial conditions where the expansion is rapid, a reasonable ion spectrum was obtained only for the first $10\, \mu s$ or so. For these datasets, size variation is not nearly enough to establish a good fit and make

deductions from the fit parameters. For very low density data ($n_0 < 2 * 10^{-15} m^{-3}$), the expansion is slow enough to get data for long delay times. However, due to the poor signal to noise, the size measurement is not reliable. Another reason why the fit to the size evolution does not give expected results is because of the way the size of the cloud is determined. Eq. 3.22 gives the size of the plasma cloud. However, the absorption cross-section of the ions is assumed to be constant throughout the cloud, which is not really true. This brings uncertainties in the measurement of the cloud size and the value of σ_x and σ_y as obtained from Eq. 3.22 does not really reflect the true size of the cloud. Inexplicably, some of the data gives the expected value for T_{e0} while others are far from expectation.

Fig. 4.6 shows the T_{e0} for datasets taken at different initial conditions. The figures compare the T_{e0} obtained from the fit of the size evolution of the UNP to Eq. 4.2 and a fit of the effective ion velocity (v_{RMS}) evolution to Eq. 4.9. The fits to the ion effective velocity evolution are more constrained and the fit parameters have small uncertainties. Hence, the fit is much more trustworthy. The T_{e0} from the size fit has large error bars which results from the uncertainties in the measurement of the plasma cloud size along the two axes. The uncertainties make it difficult to trust the results of the fits to size evolution. Although the size fits give large errorbars, the T_{e0} from the size and effective ion velocity fits match to a reasonable extent in both axes.

In this chapter, we discussed the self-similar Gaussian expansion of a UNP. The theoretical work done in the last few decades was experimentally verified. It is exciting

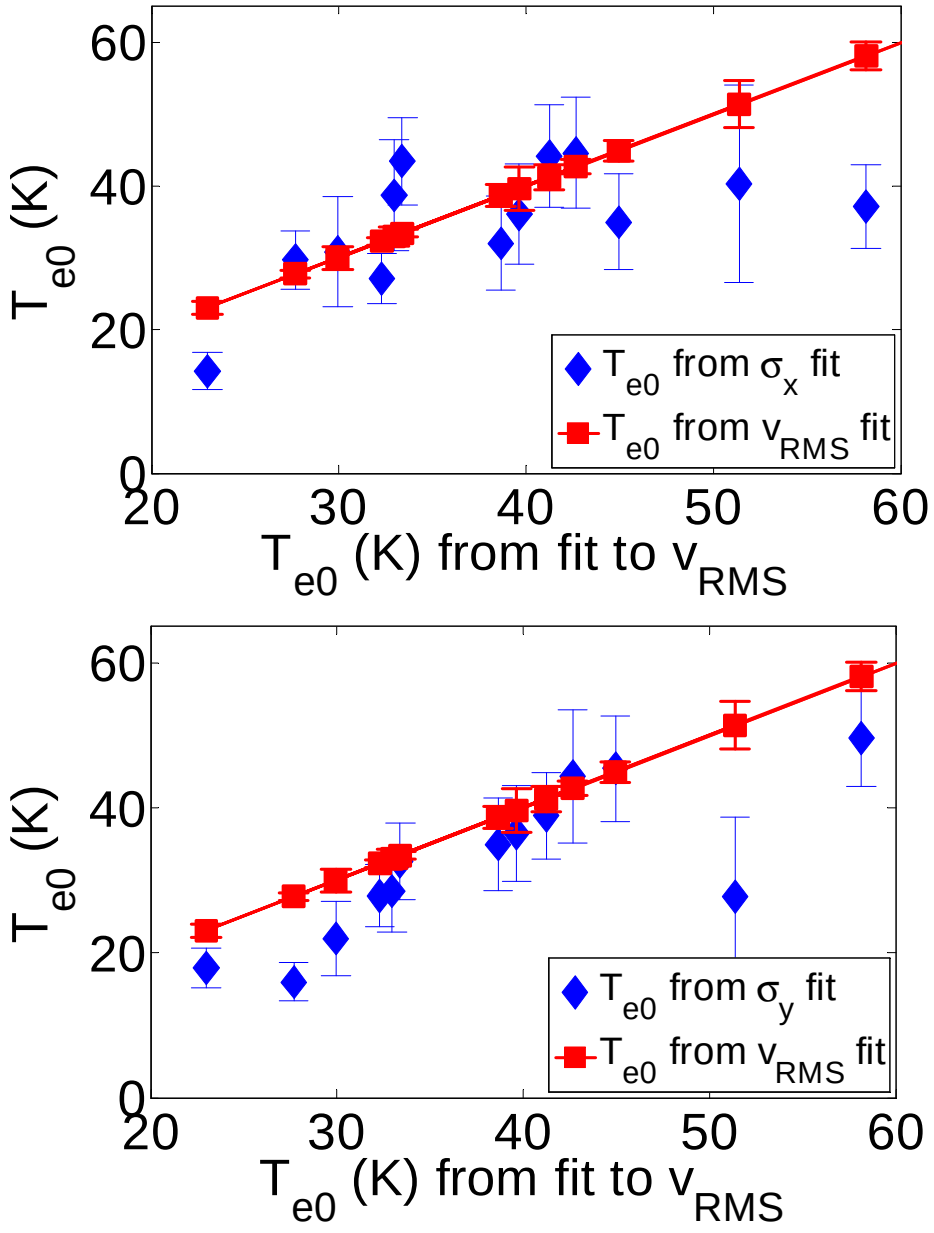

Figure 4.6: The figure shows a comparison of the fit parameter T_{e0} obtained from a fit of the solutions to the Vlasov equation to the effective ion velocity evolution and the ion cloud size evolution in x and y axes. While the values of T_{e0} obtained from the fits match reasonably, the ion cloud size evolution fit has big uncertainties which makes it difficult to trust the fit. Due to a systematic error in the measurement of cloud size in the y-axis, all the values of T_{e0} from the size fit are equal to or smaller than the T_{e0} from the fit to the effective ion velocity evolution.

to know that under certain initial conditions, the UNP expansion is similar to the expansion of plasmas found in stellar systems and produced by an intense laser field hitting solid and gaseous targets. Under such conditions, UNPs can serve as model systems to study the evolution of astrophysical plasmas and verify plasma theory. (The limits on the initial conditions under which the UNP undergoes an adiabatic expansion will be quantified in the next chapter.)

Chapter 5

Electron Temperature Evolution

A UNP expands because of the thermal pressure from the electrons. Understanding the electron temperature evolution is critical to controlling and modifying the rate of plasma expansion. This study of plasma expansion under different initial conditions shows that the electron temperature evolution can be categorized based on the significance of the various collisional processes in a UNP. The plasma expands adiabatically when we start with high initial electron temperature and/or low initial plasma density. Under these conditions, the ions and electrons undergo elastic collisions, but the inelastic collisions such as TBR and R-e are insignificant and there is no external source of heat. This type of evolution is labeled as 'Elastic Collisions Regime'. In contrast, for low initial electron temperature and/or high density, the inelastic collisions become significant during the evolution, and the plasma is no longer an adiabatic system. This type of evolution involves heating of the electrons beyond the energy provided by the ionizing photon, and is labeled as 'Inelastic Collisions Regime'. A third type of evolution is observed when a UNP is created from a cold Rydberg gas. This evolution depends on the process by which the cold Rydberg gas

ionizes to form a plasma. This type of evolution is labeled as 'Rydberg to Plasma Regime'. While these three evolutions are very different, the electrons are not in the strongly coupled regime during any of these evolutions.

5.1 Elastic Collisions Regime

The simplest form of plasma expansion is one in which there is no external source of energy such that the system is adiabatic throughout the expansion. While there are elastic collisions between the ions and electrons, there are no inelastic collisions such as TBR and R-e that heat the electrons. Under these conditions, the electron temperature decreases with time due to adiabatic expansion as the electron kinetic energy is converted to the ion expansion energy. As explained in chapter 4, this form of clean expansion is described by the analytical solution to the Vlasov equations, and the electron temperature evolution can be determined accurately. The expansion process under such conditions was described in detail in the previous chapter. High initial electron temperature and/or low initial plasma density turns off collisional processes such as TBR, R-e, RD, EQ and minimizes the effects of TL and DIH, resulting in a purely adiabatic expansion.

Fig. 5.1 shows the effective ion velocity evolution during the adiabatic expansion of UNP with $n_0 = 3.5 * 10^{15}\, m^{-3}$ and $\sigma_0 = 1\, mm$, for initial electron temperature $2E_e/3k_B = 116\,\mathrm{K}$, $60\,\mathrm{K}$ and $25\,\mathrm{K}$. The solid line in the figure is a fit of Eq. 4.9 to the data with T_{e0} and T_i as the fit parameters. According to the adiabatic electron

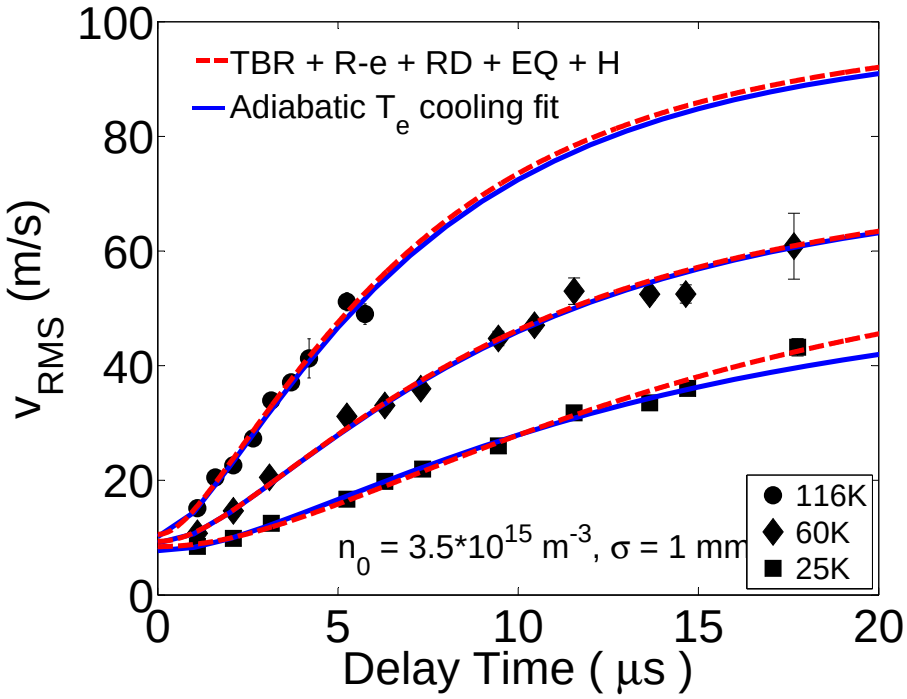

Figure 5.1: The effective ion velocity evolution is plotted for $2E_e/3k_B = 116\,\mathrm{K}$, $60\,\mathrm{K}$ and $25\,\mathrm{K}$. The solid line is a fit to the adiabatic electron temperature cooling model with T_{e0} as one of the fit parameters. The fit gives $T_{e0} = 109 \pm 4\,K, 61 \pm 1\,K$ and $32 \pm 1\,K$ respectively. The dashed line is the result of theoretical simulations with no fit parameters. The simulations are performed for the same initial conditions as the experimental data.

temperature cooling model, T_{e0} is an effective initial electron temperature when all the electron heating processes have become insignificant within the first few microseconds after photoionization. Fig. 5.2 shows a schematic of how long the various electron heating processes are significant after photoionization. However, for the adiabatic electron cooling model, the key assumption is that all these processes happen within a few microseconds. The fit parameter T_{e0} gives the electron temperature after these processes become insignificant. This assumption is justified for an adiabatic plasma expansion; however, if the electron heating processes are significant, then the adiabatic electron temperature cooling model is not applicable.

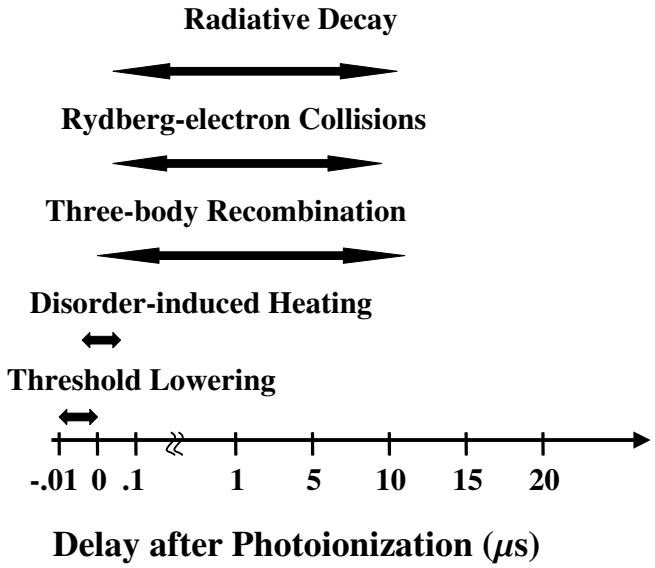

Figure 5.2: The figure shows the timescale over which some of the significant electron heating processes occur during plasma evolution. While TL and DIH are quick processes which happen on a nanosecond timescale, TBR, R-e and RD are significant for a few microseconds after plasma creation.

With high initial electron temperature, we expect no electron heating effects (described in section 2.2) to be significant. The data confirming this fact was also discussed in chapter 4. Since T_{e0} is the initial electron temperature from theory, it should match the experimental initial electron temperature given by $2E_e/3k_B$. For the three datasets shown in Fig. 5.1, $T_{e0} = 109K \pm 4K \approx 116K$ and $T_{e0} = 61K \pm 1K \approx 60K$; however, $T_{e0} = 33K \pm 1K \not\approx 25K$. This inequality implies that the 25 K data has some external source of heat during its evolution.

To verify the results, we collaborated with a theorist, Thomas Pohl [61], who simulated the plasma expansion [56]. His simulations included the various plasma

processes that are significant during the evolution on a microsecond timescale (refer to section 3.2.1). Thomas Pohl simulated the ion velocity and electron temperature evolution for the same initial conditions as the experiments. He included the effects of three-body recombination (TBR) and Rydberg-electron collisions (R-e), Radiative decay (RD), ion-electron thermalization (EQ) and the initial heat due to disorder-induced heating (H). Section 3.2.1 gives an overview of how the various collisional processes are included in the simulations.

The simulations do not include the effect of TL. Resolving rapid processes such as TL would make it computationally intensive to simulate the entire expansion which happens on a tens of microsecond timescale. The effect of TL is to increase the electron temperature which would subsequently decrease the effect of DIH. Instead of simulating this complicated behavior, Thomas Pohl kept the simulations simple by neglecting the effect of TL under the assumption that the photoionizing pulse is so short that all the electrons are created at the same time. A detailed understanding of the heating due to TL and DIH, and their interdependence, is still an open question; however, this method covers the essential physics of the initial heating of the electrons.

The effect of EQ is calculated with Eq. 2.14; however, it is negligible for the UNPs discussed in this chapter. The dashed lines in Fig. 5.1 show the result of the effective ion velocity simulations. The simulations do not include any fit parameters; instead they simply evolve the ions and electrons starting with the same initial conditions of $2E_e/3k_B, \sigma_0$ and n_0 as the experiments. The results of the adiabatic electron

temperature cooling fit and the simulations match exactly for the 116 K and 60 K data. The fact that the simulations do not contain any fit parameters, yet the simulation results overlap perfectly with the experimental data gives a lot of confidence in the validity of the physics that is being communicated by the experimental results. Also, the results of the simulations are exactly the same whether the effects of TBR, R-e, RD, EQ or H are included or excluded, emphasizing the insignificance of these processes. There is a non-negligible discrepancy between the results of the adiabatic electron temperature cooling fit and the simulations for the 25 K data. Probably at this electron temperature, certain electron heating mechanisms start to become significant. This hypothesis will be discussed in greater detail later in this section.

The electrons undergo adiabatic cooling (given by Eq. 4.4) due to expansion, and there is no significant external source of heat during the expansion. Fig. 5.3 shows the electron temperature evolution corresponding to the effective ion velocity evolution for the three datasets shown in Fig. 5.1. The solid line shows the electron temperature evolution using Eq. 4.4 corresponding to the adiabatic electron temperature cooling fit. The dashed line is the result of the theoretical simulations of the expansion. The electron temperature evolution from the fit and simulations overlap within the uncertainties for the 116 and 60 K data; however, they differ slightly for the 25 K data.

For the 25 K data shown in Fig. 5.1, $T_{e0} \approx 33\,K$ implying that there is an additional source of heat for the electrons, beyond what was provided by the ionizing

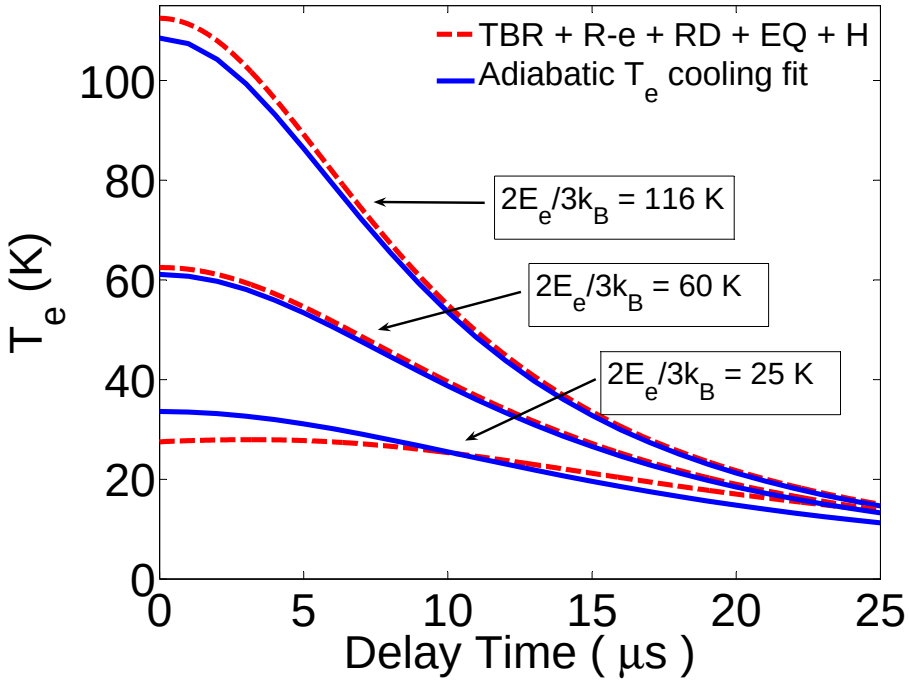

Figure 5.3: The electron temperature evolution corresponding to the ion velocity evolution shown in Fig. 5.1 is plotted. The solid line shows the temperature evolution according to the adiabatic electron temperature cooling fit and the dashed line is the result of theoretical simulations. The adiabatic cooling curve and the simulations curve matches well for the higher electron temperature data; however, there is slight discrepancy between the two for the lowest electron temperature data.

photon. This heating of electrons means that the plasma does not undergo a pure adiabatic expansion. Fig. 5.4 shows the 25 K data again, with the adiabatic electron temperature cooling fit as well as the results of the simulations. The various electron heating/cooling processes have been turned on or off in the simulations to gauge the significance of each process individually. The dot-dashed curve includes only TBR and R-e. The effect of RD is added to TBR and R-e in the cyan dotted curve, while the effect of both RD and EQ are added in the green dotted curve. The dashed curve includes the effect of TBR, R-e, RD, EQ and H. The solid line is a result of the fit to

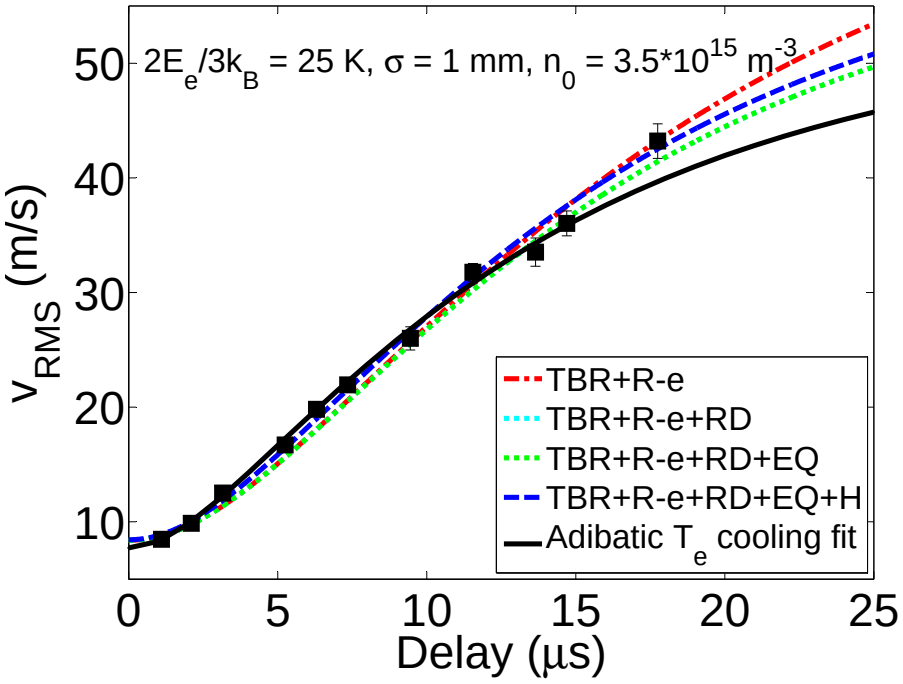

Figure 5.4: The figure shows the ion effective velocity evolution for an initial electron temperature of 25 K. The solid line is a fit of the data to the adiabatic electron temperature cooling fit which gives a value of $T_{e0} = 33 \pm 1\,K$. The dot-dashed line includes the effect of TBR and Rydberg-electron collisions. The effect of RD and EQ is added in the dotted lines; however, since the effect of EQ is negligible, the two lines overlap perfectly. The effect of H is added in the dashed line.

the adiabatic electron temperature cooling model. The fact that all the curves almost overlap shows that none of the electron heating processes is dominant, although their combined effect is not as negligible as in the case of the 116 K and 60 K data.

Fig. 5.5 shows the electron temperature evolution corresponding to the adiabatic electron temperature cooling fit and the various theory curves for the 25 K data shown in Fig. 5.4. It is evident from Fig. 5.5 that the various curves do not overlap, indicating that the data does not undergo a purely adiabatic expansion. The curves do not overlap because the adiabatic electron temperature cooling model assumes

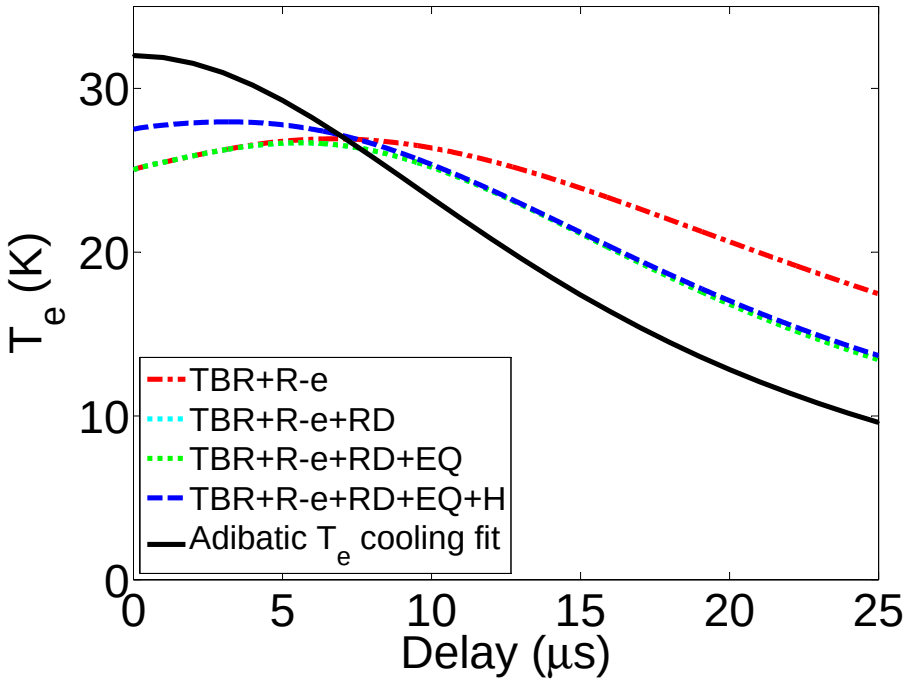

Figure 5.5: The figure shows the electron temperature evolution corresponding to the data presented in Fig. 5.4. The solid line shows the adiabatic cooling of the electrons with $T_{e0} = 33\,K$. The dot-dashed line includes the effect of TBR and Rydberg-electron collisions. The effect of RD and EQ is added in the dotted lines; however, since the effect of EQ is negligible, the two lines overlap perfectly. The effect of H is added in the dashed line. The solid line and the dashed line do not overlap indicating that the plasma does not undergo a purely adiabatic expansion under these experimental conditions.

that all the electron heating process happen on a rapid timescale $< 1\,\mu s$. Hence, the T_{e0} obtained from the fit includes the effect of all the heating mechanisms effectively at time, t = 0. After that the electron temperature decreases rapidly according to Eq. 4.4. However, the interpretation of the simulations results gives a different dynamic. The simulations give accurate results for the ion and electron evolution and can be trusted over the adiabatic electron temperature cooling fit results. The superiority of the simulations is confirmed by the fact that the theoretical curves overlap with the effective ion velocity evolution data perfectly even though the simulations have no fit

parameters.

Although the simulations can predict the ion and electron evolution accurately, the experimental results are critical to determine the relative significance of each of the collisional processes during the plasma expansion. This will be more evident in the next section which shows results for which the theoretical curve which includes only TBR and R-e clearly does not overlap with the experimental data, thus confirming that the simulation is missing a significant process during the expansion. Hence, a combination of experimental and theoretical results is the key to establishing flawless physics of UNPs in this study.

The results of the simulations shown in Fig. 5.5 are interpreted as the following: DIH happens on a few tens of nanosecond timescale, while the expansion happens on a microsecond timescale. Hence, the heat due to DIH can effectively be added to the electron temperature at t = 0. Under this assumption, the figure shows that the initial heating due to H increases the electron temperature by $\sim 2\,\mathrm{K}$ since the theory curve shows an electron temperature of $\sim 27\,\mathrm{K}$ at t= 0. At this electron temperature, the rate of TBR is not negligible. Hence, processes such as TBR and R-e bring in some amount of heat which counteracts the effect of cooling due to adiabatic expansion such that the electron temperature is maintained fairly constant for the next $6\,\mu s$. Effects such as RD significantly decrease the amount of heat due to Rydberg-electron collisions as explained in section 2.2.7. However, the fact that the TBR+R-e+RD and TBR+R-e+RD+EQ curves overlap perfectly with the TBR+R-e curve shows

that the effects of RD and EQ are insignificant. As the plasma expands and the density decreases, the heating due to the processes such as TBR and R-e becomes negligible and the cooling due to adiabatic expansion starts to dominate.

This electron temperature evolution in the UNP with initial electron temperature of 25 K is different from that of the UNPs with 60 K and 116 K in which the electrons undergo adiabatic cooling as the plasma expands, with no heating at any stage of the expansion. The deviation of the 25 K data from a purely adiabatic expansion invoked thinking on a non-adiabatic expansion. Hence, the next step was to explore a regime in which effects such as TBR and R-e are very significant, as is described in the next section.

5.2 Inelastic Collisions Regime

For UNPs with low initial electron temperature and/or high density, TL, DIH, TBR, R-e and RD start to become important. The inelastic collisional processes bring energy into the system as the plasma expands and the UNP is no longer adiabatic. The heating due to TL and DIH in the first few ns is significant in this region of parameter space. Due to the low electron temperature and/or high density, there is significant TBR [26, 27, 66, 82, 83] as shown in Fig. 2.4, and Rydberg electron collisions [26, 65] as shown in Fig. 2.7 at early delay times ($< 5\mu s$). The rate of recombination $R \propto n_0^3 T_e^{-9/2}$ and hence TBR is a negative feedback effect; so as the electrons heat up due to recombination, the rate of TBR decreases. In addition to

TBR, Rydberg-electron collisions further heat up the electrons and reduce the rate of recombination. Radiative decay of the Rydberg atoms contributes significantly to the evolution. Radiative decay causes the highly excited Rydberg atoms to decay to lower lying quantum states thereby reducing the number of Rydberg atoms available for R-e. Hence, there is less heating of electrons from the reduced number of Rydberg-electron collisions.

Fig. 5.6 shows the effective ion velocity evolution of a UNP with $2E_e/3k_B = 14\,K$, peak plasma density of $7 * 10^{15}\,m^{-3}$ and initial size of 0.9 mm. The solid line in the figure is a fit to the adiabatic electron temperature cooling model; the fit gives $T_{e0} = 34 \pm 1\,K$. The fact that $T_{e0} >> 2E_e/3k_B$, indicates that the plasma expansion is not adiabatic in this region of parameter space. There is tremendous heating of the electrons as the plasma evolves, causing the expansion to deviate from the 'ideal' expansion. Hence, while a fit to the adiabatic electron temperature cooling model is surprisingly accurate, the value of the fit parameter T_{e0} does not have a real physical meaning.

From the experimental results, the general behavior of the electron temperature evolution is evident, which is that the electrons are heated due to inelastic collisions. However, to get a detailed description of the evolution, to examine exactly for how long these processes are significant, and to quantify their contribution, we have to turn to simulations. The theoretical simulations done by Thomas Pohl unravel the complicated electron temperature evolution which dictates the plasma expansion.

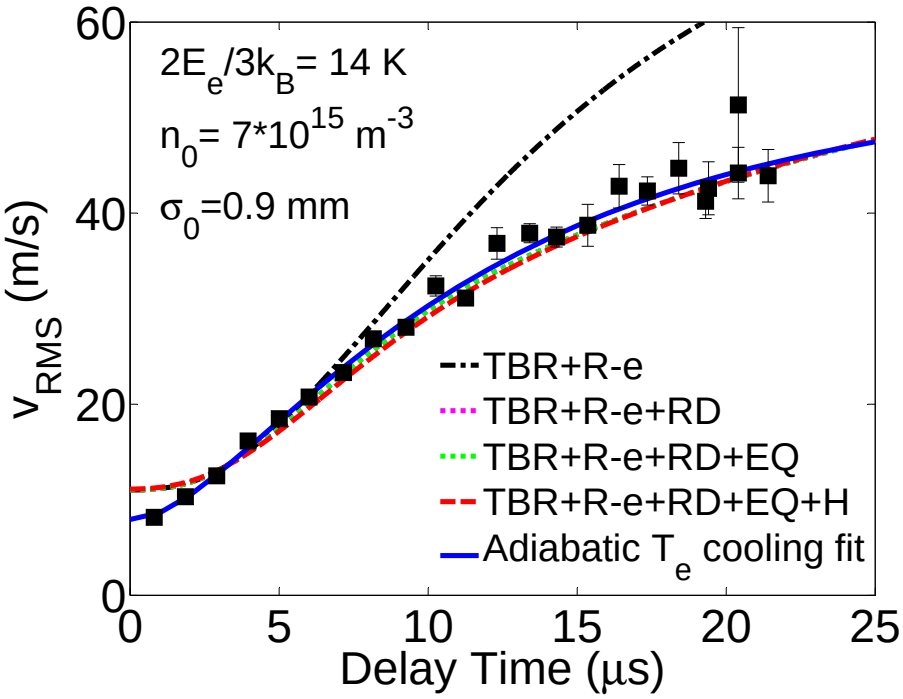

Figure 5.6: The figure shows the effective ion velocity evolution for UNP with initial electron temperature of 14 K. At this low temperature, effects such as TBR, R-e, RD, EQ and H are significant and heat the electrons in the first few microseconds after photoionization. The solid line is a fit to the adiabatic electron temperature cooling fit which gives a value of $T_{e0} = 34 \pm 1\,K$. The dot-dashed line does not fit the data indicating that TBR and Rydberg-electron collisions alone cannot explain the electron dynamics. The significance of RD is evident from the fact that inclusion of this effect make the theory curve go through the data perfectly. The effect of EQ is insignificant, hence, the two dotted line with and without EQ overlap perfectly. The effect of H also seems negligible since the dashed line overlap with the dotted lines.

By turning the various electron heating/cooling mechanisms on or off during plasma evolution, the simulations give a clear picture of the relative importance of the various processes. The simulations do not contain any fit parameters, as explained in the previous section.

The dot-dashed line in Fig. 5.6 is a result of the theoretical simulations when only the effect of TBR and Rydberg-electron collisions is included in the evolution.

Clearly, the curve does not match the data, indicating that other collisional processes are dominant during the expansion. The dotted line, which shows the expansion including the effects of TBR + R-e + RD, overlaps the data much better, emphasizing the importance of the effect of RD in the evolution. The dotted line indicates a lower rate of expansion than the dot-dashed line, implying that the instantaneous electron temperature is lower, thereby exerting a smaller force on the ions. This makes sense from the explanation given in section 2.2.7. Due to radiative decay of Rydberg atoms, fewer highly excited Rydberg atoms undergo collisions with electrons because once a Rydberg atom decays radiatively to a deeply bound state, the rate of collisions with electrons decreases significantly. The net effect is that there is less heating of the electrons due to Rydberg electron collisions which leads to a lower electron temperature at a given delay after photoionization than in the absence of RD.

The two dotted lines corresponding to TBR + R-e + RD and TBR + R-e + RD + EQ overlap perfectly, indicating that the effect of EQ is negligible. The dashed line which includes the effect of TBR + R-e + RD + EQ + H overlaps the data well, although the effect of H is also insignificant. The various curves generated by the theoretical simulation do not overlap the data at early delay times of 1 - 2 μs due to a discrepancy in the method by which the initial ion temperature is calculated by the simulations and the formula given by Murillo [23] (The formula given by Murillo was verified by Chen *et al.* [11]). The discrepancy does not significantly affect the rest of the evolution of the effective ion velocity.

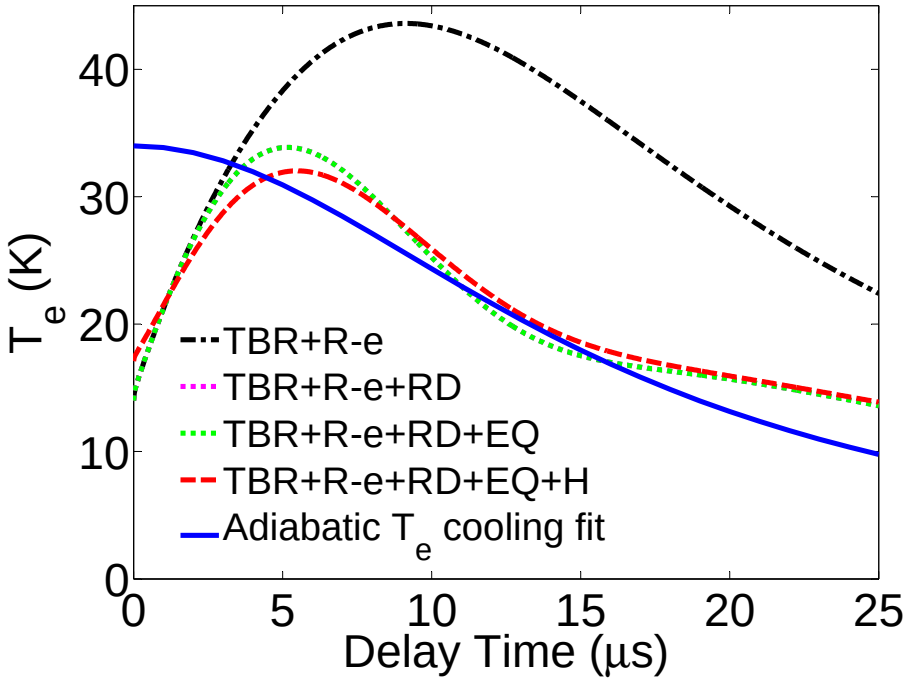

Figure 5.7: The figure shows the electron temperature evolution corresponding to the data shown in Fig. 5.6. The dot-dashed line which includes the effect of TBR and Rydberg-electron collisions shows that if only these processes were included, there would be tremendous heating of electrons for a long time. The effect of RD tends to decrease the heat due to Rydberg-electron collisions tremendously, hence the dotted line indicated much less electron heating. The effect of EQ is negligible so the two dotted lines with and without EQ overlap. The effect of H is not significant although it is not negligible either as shown by the dashed line.

Fig. 5.7 shows the electron temperature evolution corresponding to the data shown in Fig. 5.6, with the various electron heating processes turned on and off. The solid line shows the electron temperature evolution obtained by the adiabatic electron temperature cooling model. The dot-dashed, dotted and dashed lines are a result of the simulations done by Thomas Pohl. The dot-dashed line shows the evolution if only TBR and Rydberg-electron collisions are included in the plasma evolution simulations. As explained earlier, the effect of RD is to decrease the amount of heat

that comes into the system due to Rydberg-electron collisions. This effect is clear from the dotted line in the figure. For the first few microseconds, there is significant TBR and R-e which heats the electrons by ∼15 K. Then the effect of RD starts to become significant and the Rydberg-electron collisions begin to decrease. Also, the rate of TBR decreases since the electrons have heated up. Hence, within the first 5 μs, all the electron heating processes become negligible and the system becomes close to adiabatic again, and the cooling due to plasma expansion starts to dominate. The dashed line shows the electron temperature evolution including TBR + R-e + RD + EQ + H. The initial heating of the electrons by a few kelvin is evident in Fig. 5.7 with the inclusion of H. According to the calculations shown in Fig. 2.3, DIH for a plasma density of $7 * 10^{15}\, m^{-3}$ heats the electrons by $\sim 3\, K$, which is the same as the value of H according to the simulations. This increase in electron temperature decreases the rate of TBR and subsequently affects the R-e and RD. Hence, as shown in Fig. 5.7, the dashed line deviates slightly from the dotted line in the first few microseconds and the maximum temperature reached by the electrons is lesser than if this effect was turned off.

A closer look at Fig. 5.7 shows that at a delay of $\sim 15\, \mu s$, the electron temperature starts to deviate from the expected adiabatic electron cooling behavior. This deviation occurs because as the electrons cool down due to adiabatic expansion, effects such as TBR and R-e start to become significant again and bring in more heat to the system. So the electrons begin to heat again. However, since the density of the plasma has

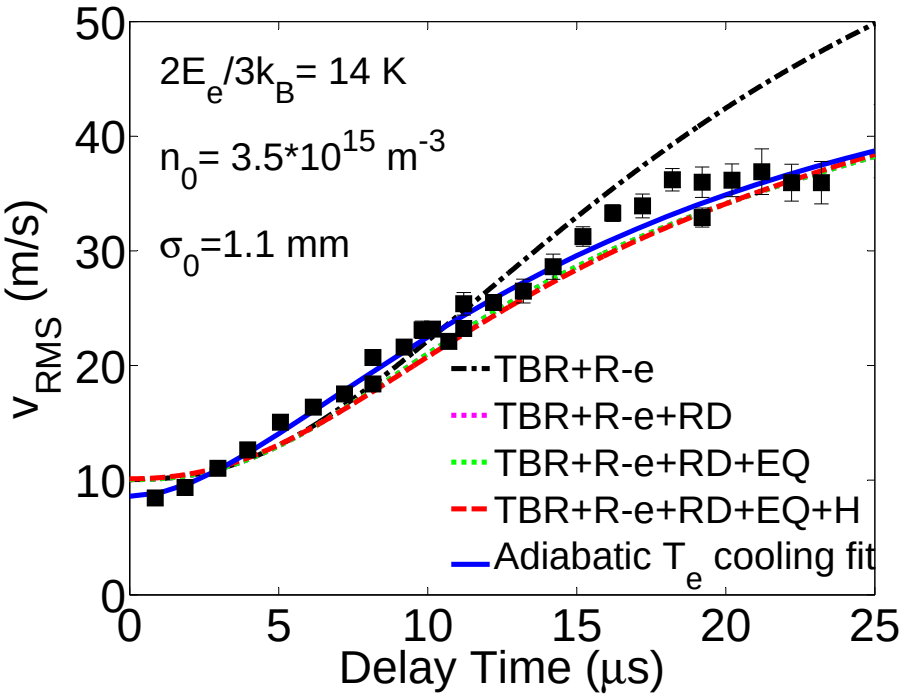

Figure 5.8: The figure shows the effective ion velocity evolution for UNP with initial electron temperature of 14 K. At this low temperature, effects such as TBR, R-e, RD, EQ and H are significant and heat the electrons in the first few microseconds after photoionization. A comparison of the effective ion velocity with that shown in Fig. 5.6 proves that the density dependent processes such as TBR and R-e heat the electrons less for lower density plasma such that the rate of expansion is slower.

decreased considerably due to expansion, the rate of TBR and R-e is less than it was at the early delay times.

Fig. 5.8 shows another instance of moderate heating of electrons due to inelastic collisions in a UNP. The $T_{e0} = 27 \pm 0.4\,K$ for this data. Figs. 5.9 shows the corresponding electron temperature evolution. The difference between Figs. 5.6 and 5.8 is the initial plasma density and cloud size of the UNP. The rate of expansion is higher if we start with a plasma at higher density and/or smaller cloud size. If we compare the effective ion velocity at $20\,\mu s$ after photoionization in Figs. 5.6 and 5.8, we can

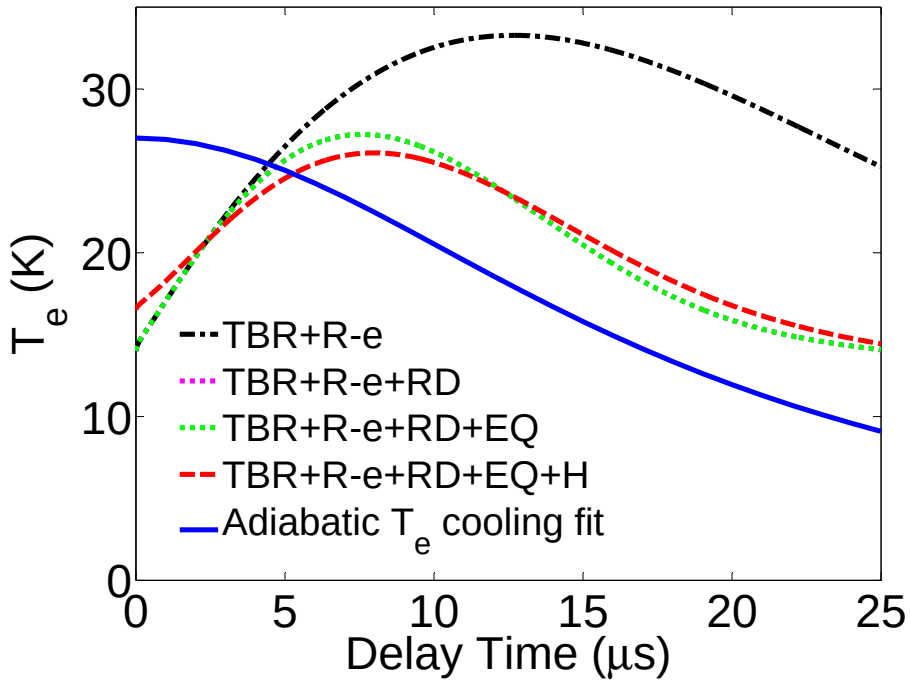

Figure 5.9: The figure shows the electron temperature evolution corresponding to the data shown in Fig. 5.8. A comparison of the electron temperature evolution with that shown in Fig. 5.8 indicates that due to lower density, processes such as TBR and R-e heat the electrons less and more slowly. This is why the electrons reach peak temperature of 25 K at $\sim 8\,\mu s$ while in Fig. 5.8 the peak temperature of 32 K is reached within $5\,\mu s$.

see that the data at higher density has an effective ion velocity of $\sim 44\,m/s$, while the one at lower density is $\sim 38\,m/s$. A higher effective ion velocity indicates that the rate of expansion is higher which is due to a greater pressure from the electrons. The greater force on the ions occurs because of higher electron thermal energy.

A comparison of Figs. 5.7 and 5.9 shows that the former has faster and greater electron heating than the latter. The UNP in Fig. 5.7 has a higher density and a smaller initial cloud size than the UNP shown in Fig. 5.9, so the rate of TBR and R-e are greater. Once the electrons reach a temperature of 25-30 K, the various electron heating processes become insignificant and the adiabatic cooling of the electrons

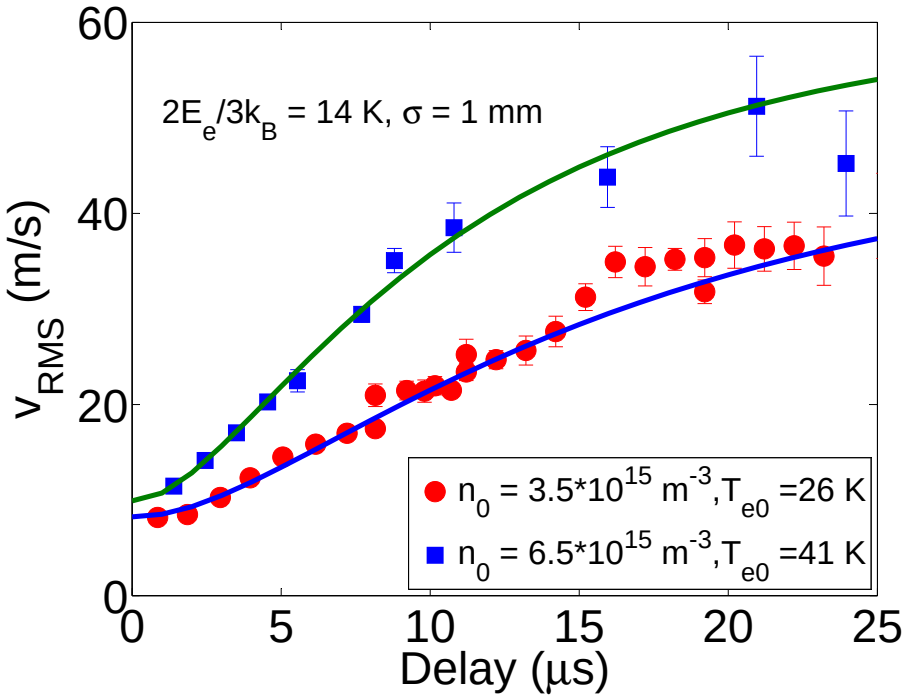

Figure 5.10: The figure shows the ion effective velocity evolution for two datasets with same initial electron temperature and plasma cloud size but different initial plasma density. The fact that the data with higher density undergoes a more rapid expansion than the data at lower density shows the importance of the density-dependent collisional processes that heat the electrons and increase the rate of expansion.

starts to dominate. This behavior is dominant regardless of initial conditions of the UNP. The difference lies in how long it takes to heat the electrons to a high enough temperature such that the inelastic processes become insignificant. In Fig. 5.7, the electrons heat up to a temperature of $\sim 32\,K$ in $5\,\mu s$, while Fig. 5.9 shows that the electrons heat up to a temperature of $\sim 25\,K$ in $8\,\mu s$.

Processes such as TBR, R-e and RD are density-dependent. The two datasets shown so far in this section prove the density dependence of the collisional processes; however, the UNPs in the two datasets shown also have different initial size. If we hold all the other plasma parameters constant except density, the electrons heat up

more due to the inelastic collisional processes in a UNP with a higher peak plasma density. This effect is evident in Fig. 5.10 which shows two datasets with same initial electron temperature of 14 K and cloud size of 1 mm, but the density is different by almost a factor of two. The solid lines in the figure show the adiabatic electron temperature cooling fit to the two datasets. The $T_{e0} = 41\,K$ for the high density data is greater than that for the lower density data ($T_{e0} = 26\,K$) indicating that the density-dependent processes such as TBR, R-e and RD are more dominant at higher plasma density and heat the electrons more.

Having established the significance of the density dependent processes such as TBR, R-e and RD in this regime, it is interesting to test how far this regime extends into the parameter space. As we go to lower electron temperatures, the rate of TBR is higher. Due to their low kinetic energy, the electrons are bound in high lying Rydberg states. The Rydberg atoms thus formed undergo collisions with electrons and also decay radiatively. For Rydberg atoms in high principal quantum states, the rate of excitation from collisions with electrons is higher, as is shown in section 2.2.6. This type of collision tends to cool the electrons; however, the heating of electrons due to TBR supersedes the cooling effect due to Rydberg excitation so the net effect is a slow heating of the electrons. As the electrons heat up, they tend to recombine into more deeply bound Rydberg states. For Rydberg atoms in low lying states, the rate of de-excitation is higher than the rate of excitation from collisions with electrons. Hence, now the electrons are heated due to TBR as well as de-excitation of Rydberg

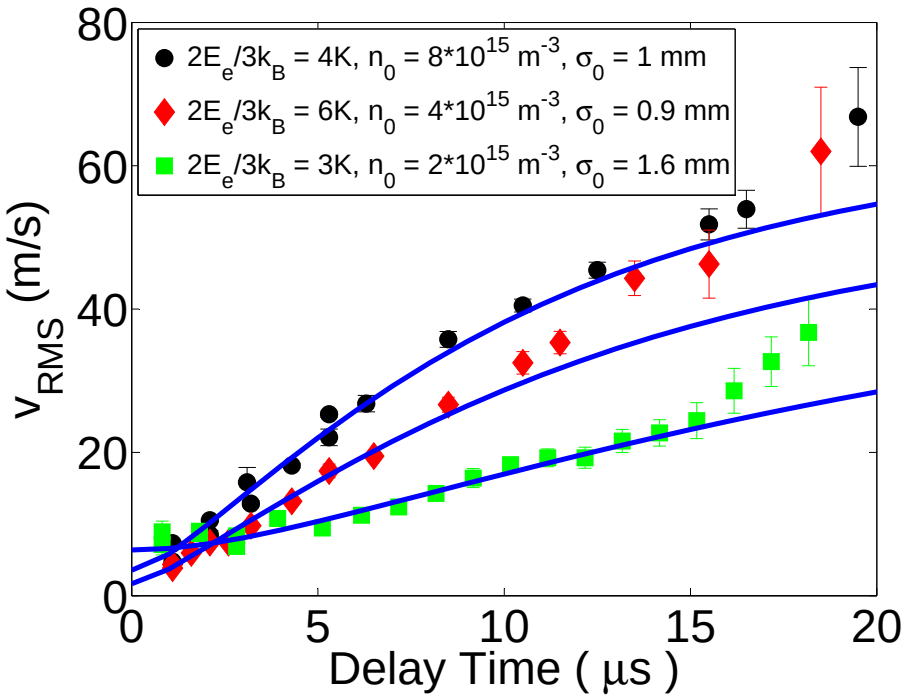

Figure 5.11: The figure shows the effective ion velocity evolution for UNPs with $2E_e/3k_B = 3\,K, 4\,K$ and $6\,K$. The rate of plasma expansion is higher for the UNP with higher density. The solid lines show a fit to the adiabatic electron temperature cooling model. While the value of the fit parameter T_{e0} does not have a real physical meaning, its relative value indicates the relative amount of heating of the electrons during the UNP expansion.

atoms.

To summarize, if we start with colder electrons, the general electron temperature evolution is the same as shown in Figs. 5.7 and 5.7; however, the heating phase lasts much longer. Apart from the counteracting heating and cooling effects, the heating is also slow because it takes longer to increase the temperature of the electrons from a few kelvin to 25-30 K than it takes when we start with an electron temperature of 14 K.

Fig. 5.11 shows a plot of the effective ion velocity evolution along with the adia-

batic electron temperature cooling fit for three datasets with:

$2E_e/3k_B$ (K)	n_0 (m^{-3})	σ_0 (mm)	T_{e0} (K)
3	$2 * 10^{15}$	1.6	27 ± 1
4	$8 * 10^{15}$	1	49 ± 1
6	$5 * 10^{15}$	0.9	35 ± 1

For low initial electron temperature the electrons are able to screen the ion-ion interactions (see section 2.1.2) more strongly. This screening implies that immediately after photoionization, the ions are at a lower potential energy than if we started with electrons at higher initial electron temperature. If their potential energy is not large, then the increase in the ion kinetic energy due to DIH is not high. This effect is evident from Fig. 5.11 in which the initial velocity of the ions is low compared to data shown in Figs. 5.1, 5.6 and 5.8 with high initial electron temperatures.

The solid lines in Fig. 5.11 are a fit to the adiabatic electron temperature cooling model. The T_{e0} obtained from the fits do not have a real physical meaning since the expansion is not adiabatic. However, the relative value of T_{e0} indicates the relative heating of the electrons. Comparing the value of T_{e0}, it is evident that the heating of the electrons is greater for UNP with higher density.

A quantitative description of the electron temperature evolution in this region of parameter space requires a numerical simulation of the expansion. The simulations done by Thomas Pohl for the expansion described in the previous section do not give accurate results for this type of evolution. The inaccuracy results from the fact that threshold lowering heats the electrons considerably for $2E_2/3k_B < 10\,K$, and cannot

be ignored. As explained in section 5.1, the simulations include the effect of DIH but exclude the heating due of TL. In this region of parameter space, the electrons are heated by 6-8 K due to TL which decreases the rate of TBR and subsequently affects the rate of R-e and RD. Hence, the inclusion of TL would modify the evolution significantly. Efforts to extend the simulation to this regime are underway.

A quantitative determination of the electron temperature evolution of UNP with $2E_e/3k_B \sim 1\,K$ requires a hybrid molecular dynamics simulation as explained in section 3.2.3. However, the experimental results give a qualitative idea of the electron temperature evolution. For UNPs with moderate electron heating, a combination of experimental results and simulations based on kinetic theory was able to determine exactly the evolution of the ions and electrons as the UNP expands.

5.3 Rydberg to Plasma Regime

Another type of evolution happens when a UNP is formed by the spontaneous ionization of a cold Rydberg gas. Inelastic collisions are expected to be significant in this regime as well; however, the evolution is more complicated. Rydberg atoms were excited to principal quantum numbers 75 and 85 at initial density of $3.5 * 10^{15}\,m^{-3}$ and initial cloud size of 1 mm. Fig. 5.12 shows the effective ion velocity evolution for a UNP created from Rydberg atoms. The solid line shows a fit of the data to the adiabatic electron cooling model. The dashed line shows a fit to the constant electron temperature model. Neither of the two models fits the data well. The data shows that

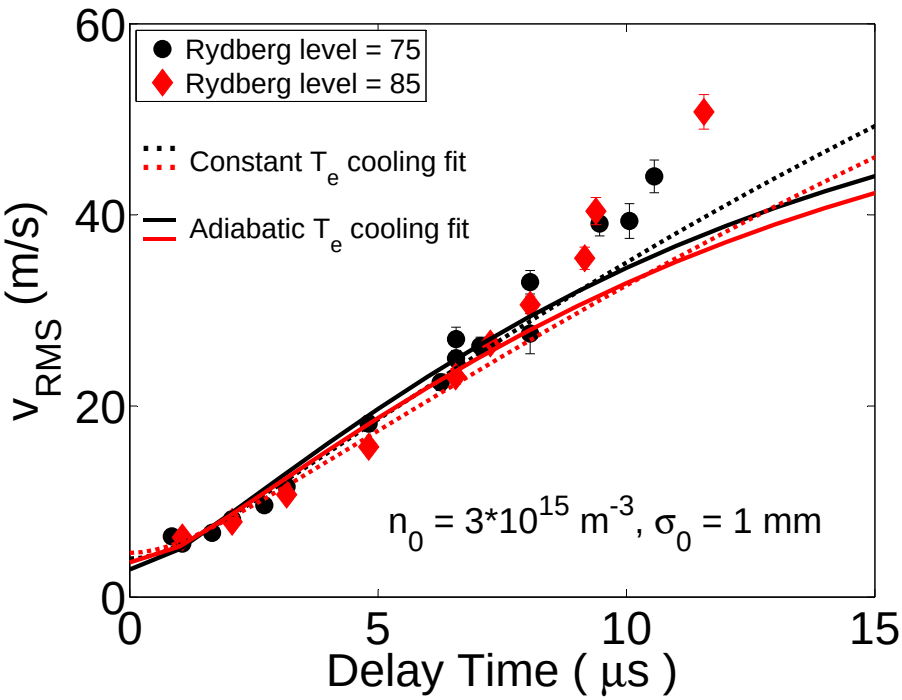

Figure 5.12: The figure shows the evolution of the effective ion velocity of UNPs created from a cold and dense gas of Rydberg atoms in principal quantum states 75 and 85. The solid lines show the adiabatic electron temperature cooling fit and the dotted lines show the constant electron temperature fit. The effective ion velocity is greater than that predicted by either of the two fits. This higher rate of expansion means that the electrons temperature is increasing as the plasma expands.

the rate of expansion of the ions is greater than predicted by either of the two models. This higher rate of expansion suggests that the electron temperature is greater than that predicted by both the models indicating that there is a constant source of heat to the electrons during the evolution even at later delay times. However, the rate of expansion is similar to the case when we start with electrons with initial temperature on the order of 1 K.

Fig. 5.13 shows that the rate of expansion of the plasma created from Rydberg atoms in principal quantum level = 85 is similar to the rate of expansion of plasma

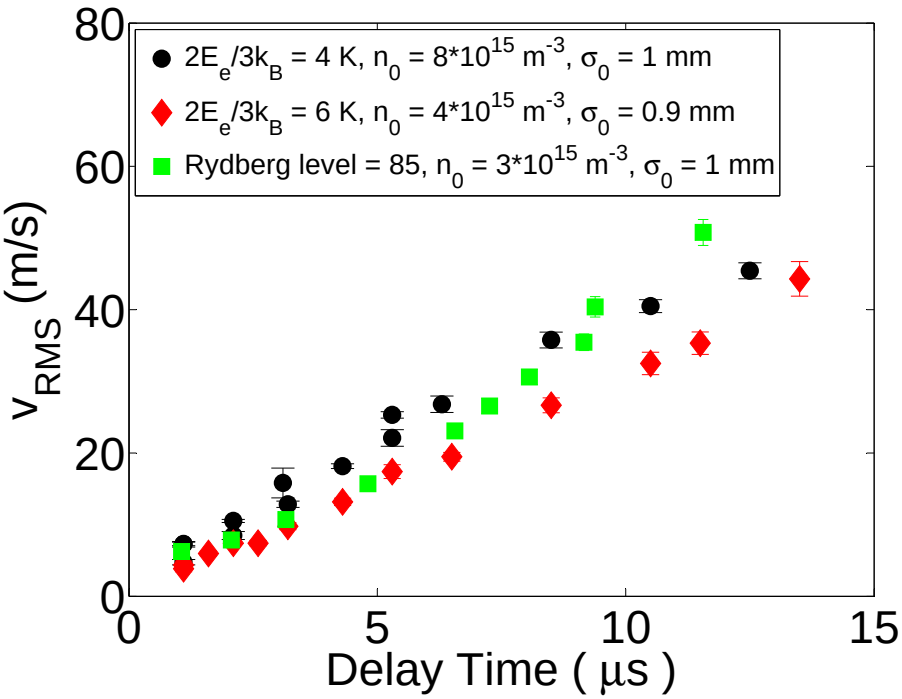

Figure 5.13: The figure shows the effective ion velocity evolution for plasma created by exciting neutral atoms above and below the threshold. The rate of expansion for plasma created by exciting Rydberg atoms is the same as that for plasma with $2E_e/3k_B = 4$ and $6\,K$. However, this does not necessarily mean that the evolution of the electron temperature is the same for these UNPs.

created with initial electron temperature of 4 K and 6 K. However, this does not necessarily imply that the electron temperature evolution is the same as well. The evolution of UNP when created from Rydberg atoms is complicated and depends on the process by which the Rydberg atoms form a plasma. It also depends on how long it takes the whole cloud to ionize. As the Rydberg atoms are getting ionized to form a plasma, the density of the plasma is increasing. At the same time, the plasma is expanding, which decreases the density. Hence, the rate of TBR, R-e and RD are changing in a complicated manner. Exploring this complicated, yet interesting evolution is a project for future work.

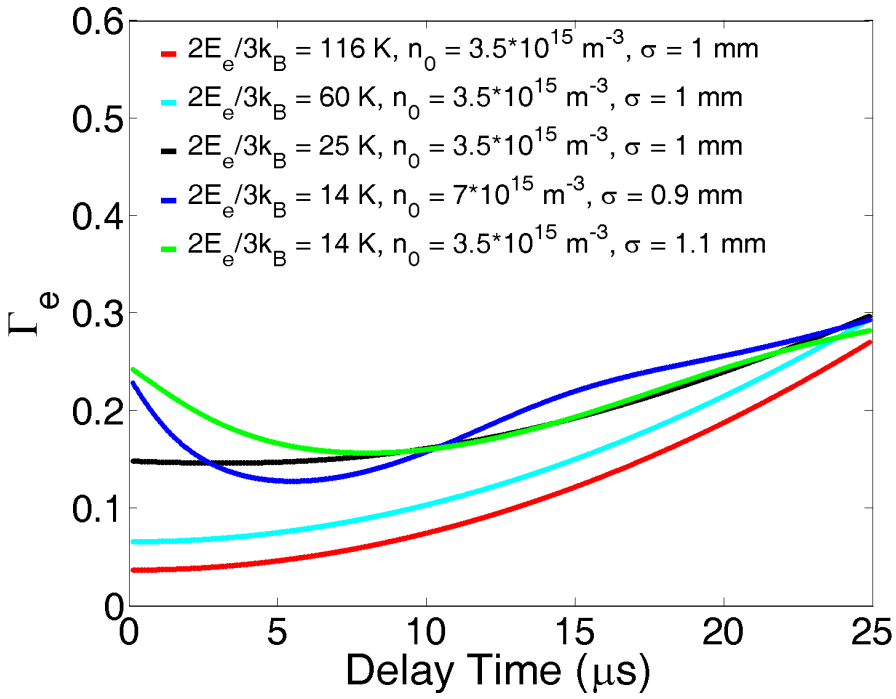

Figure 5.14: The figure shows the evolution of the electron Coulomb coupling parameter for UNPs with $2E_e/3k_B = 116\,K, 60\,K, 25\,K$ and $14\,K$. The Γ_e is calculated using peak density shown in the figure and evolving the size according to the adiabatic electron cooling model. The electron temperature evolution is set according to the result of the simulations. It is evident from the figure that the electrons are never in the strongly coupled regime for as long as the plasma is observed in this study.

5.4 Γ_e evolution in the different regimes

Strongly coupled plasmas are an interesting field of study since they exhibit collective effects [84] such as ion-acoustic waves and can undergo phase transitions to form Wigner crystals [9]. However, if a plasma is allowed to expand freely, various ion and electron heating effects decrease the Coulomb coupling parameter such that the ions are at the edge of the strong coupling regime while the electrons are completely pushed out of the strongly coupled regime [28].

Fig. 5.14 shows the evolution of the electron Coulomb coupling parameter for five

different datasets. The Γ_e is calculated using peak density as stated in the figure. For this calculation, the density is propagated assuming that the size is increasing according to Eq. 4.2 where the T_{e0} is taken from fits to the adiabatic electron temperature cooling model. This is a reasonable approximation because while the cloud is not expanding adiabatically, the adiabatic electron temperature cooling model fits the effective ion velocity evolution surprisingly well, and the size evolution is simply the effective ion velocity evolution times delay after photoionization. Fig. 5.14 shows that the electrons are never in the strongly coupled regime for as long as the plasma is observed. The Coulomb coupling parameter curves for all the datasets come together at later delay times, indicating that the electron temperatures for all the datasets come together to within a narrow range as the plasma expands. This was also shown by Roberts *et al.* [19]; however, they quoted 70% overall systematic uncertainties in their measurements. Although the Coulomb coupling parameter is increasing in time for later delay times, it is not expected to continue increasing for long because as the electrons cool down, effects such as TBR start to become significant again.

The datasets with initial electron temperature of 116 K and 60 K represent UNP which undergoes adiabatic expansion. The Γ_e initially is very low and increases as the plasma evolves. This is because the electrons cool down due to adiabatic expansion. However, during the time for which the plasma was observed with the optical probes, the electrons never reach the strongly coupled regime.

The datasets with initial electron temperature of 14 K represent UNP which un-

dergoes non-adiabatic expansion. The Γ_e decreases for the first few microseconds while the electron heating mechanisms are significantly heating the electrons. Then as the cooling due to adiabatic expansion dominates, when TBR and R-e become insignificant, Γ_e starts to increase. However, once again, during the time for which the plasma expansion is observed, the electrons never reach the strongly coupled regime.

We can qualitatively determine the evolution of Γ_e for UNPs with initial electron temperature $\sim 1\,K$. The initial Γ_e is large; however, various electron heating processes such as TL and DIH increase the electron temperature by 5-10 K within the first few nanoseconds such that the electrons are pushed out of the strongly coupled regime. Thereafter, due to effects such as TBR and R-e, the Γ_e continues to decrease for $10 - 15\,\mu s$ until adiabatic cooling starts to dominate. The electrons are not in the strongly coupled regime for as long as we are able to observe the plasma.

Even though the plasma is not strongly coupled, the electron Coulomb coupling parameter can help determine the type of expansion: elastic collisional or inelastic collisional, that the UNP might undergo. Fig. 5.15 shows a log-log plot of $T_{e0}/(2E_e/3k_B)$ with respect to Γ_e, where Γ_e is calculated from the initial electron temperature $(2E_e/3k_B)$ and peak density. With the optical probes, we are able to explore only a small range of density $(10^{15} - 10^{16}\,m^{-3})$, so the range of Γ_e in Fig. 5.15 is mostly determined by the range of initial electron temperatures that have been studied. The value of T_{e0} is obtained by fitting all the data to the adiabatic electron cooling model. From the figure, we can see that plasmas with initial $\Gamma_e < 0.2$ have

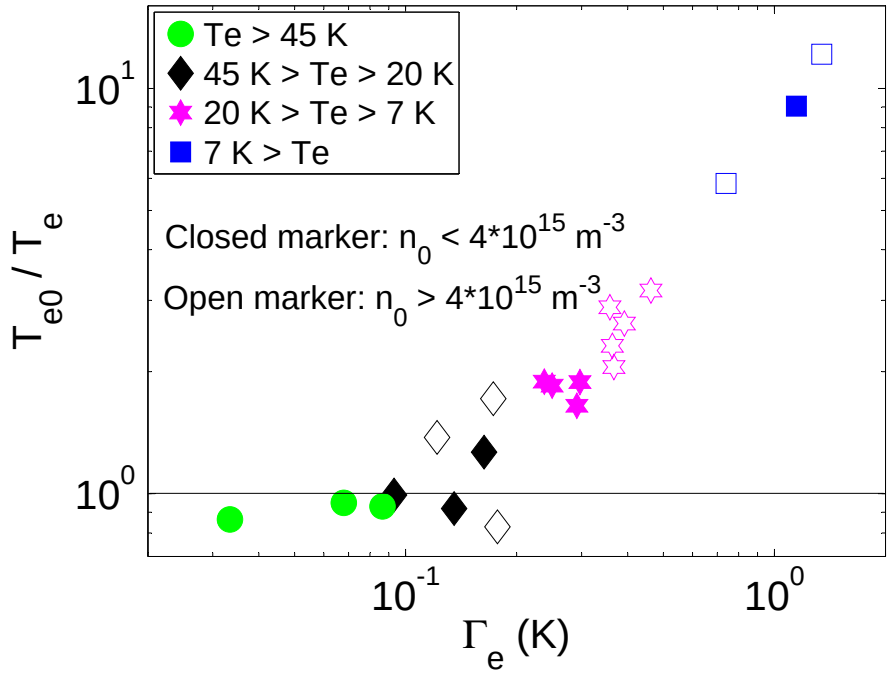

Figure 5.15: The figure shows the elastic and inelastic regimes of plasma expansion. $T_e = 2E_e/3k_B$ in (T_{e0}/T_e). For elastic collisional expansion, $T_{e0} = T_e = 2E_e/3k_B$ which is obtained for high initial electron temperatures and/or low plasma density. As the initial electron temperature decreases and/or the plasma density increases, the rate of TBR increases resulting in greater heating of the electrons. The stars are all for UNPs with $2E_e/3k_B = 14\,K$. For the same initial electron temperature, the plasma with higher density has greater heating of electrons.

$T_{e0}/(2E_e/3k_B) \sim 1$. Plasmas with initial $\Gamma_e > 1$ have $T_{e0} >> 2E_e/3k_B$ indicating that there is intense heating of the electrons. For the intermediate regions, the plasma undergoes moderate electron heating during expansion. Fig. 5.15 also shows that for the same $2E_e/3k_B$, the T_{e0} is higher for higher density data because of a higher rate of TBR and R-e.

A similar study was done by Cummings *et al.* [13] and by Kulin *et al.* [18]. They show the excess heating of the electrons during UNP evolution when the initial electron temperature is low. The study described in [13] is done with a cylindrical

plasma. Cummings *et al.* assume that the expansion along the x and y-directions of the cylindrical plasma is decoupled from the expansion along the z-direction, which is along the axis of the cylinder. However, they found that the expansion in the z-direction does, in fact, affect the expansion in the x and y-directions, while their model did not incorporate such a dependence. Also, when the expansion velocity was calculated using three different models in [13], the results were very different, hence their work has large uncertainties. Kulin *et al.* [18] studied UNPs with a large range of initial electron temperatures ($1\,K < 2E_e/3k_B < 210\,K$). They found heating of the electrons due to inelastic collisions for initial electron temperatures of $2E_e/3k_B \leq 20\,K$ with initial average densities in the range of $6 * 10^{12}\,m^{-3}$ and $2.5 * 10^{15}\,m^{-3}$. For the same range of densities but initial electrons temperatures of $2E_e/3k_B \geq 50\,K$, they found no significant heating due to inelastic collisions. They did not report results for the intermediate region of $20\,K < 2E_e/3k_B < 50\,K$. In this study, this intermediate region was explored.

Fig. 5.15 can serve as a reference to predict the amount of electron heating expected during the plasma expansion for a known set of initial electron temperature and plasma density. Then, for high initial electron temperature and/or low plasma density, the exact electron temperature evolution can be quantitatively determined with the experimental observation of the effective ion velocity evolution. For low initial electron temperature and/or high plasma density, a quantitative description of the electron temperature evolution can be obtained from experimental observation of

the effective ion velocity evolution, combined with theoretical simulations.

Fig. 5.15 shows that for $\Gamma_e < 0.2$, the UNP undergoes adiabatic expansion and belongs to the elastic collisional regime. For $\Gamma_e > 0.2$, there is additional heating of the electrons due to inelastic collisions and the UNP is not an adiabatic system as it expands. Hence, for $\Gamma_e > 0.2$, the UNP belongs to the inelastic collisional regime. Being able to determine the type of evolution that can be expected for a certain set of initial conditions is one of the main contributions of this thesis. Equipped with this knowledge, we can determine the region in parameter space which will be a good starting point to obtain strong coupling in UNPs with the help of external cooling forces such as laser cooling.

Chapter 6

Conclusion

This work represents an accurate and complete study of many plasma/atomic processes in ultracold neutral plasmas. Ultracold neutral plasmas belong to an exotic regime of plasma physics in which the ions and electrons evolve on a timescale different from that of traditional plasmas. What makes them exotic is that the ions and electrons are at a much lower temperature than most laboratory produced plasmas. This low temperature allows strong coupling such that collective effects and phase transitions can be observed.

Ultracold neutral plasmas form a bridge between atomic physics and plasma physics. They are created by photoionizing laser-cooled neutral atoms in ultra-high vacuum. The ions created are typically at millikelvin temperatures while the electrons are in the range of 1 - 100 K in this study. UNPs provide an excellent system for experimental study because the initial conditions of the plasma, which determine the rate of expansion, are completely under experimental control. The initial temperature of the electrons can be set by tuning the wavelength of the photoionizing laser; the initial density of the ions and electrons is controlled by the intensity of the

ionizing beam; and the initial plasma cloud size is set by the cloud size of the neutral atoms which is under experimental control as well.

Another unique feature of UNPs is that due to the low ion and electron temperatures, they evolve over a nanosecond to microsecond timescale. This slow evolution enables us to observe the UNPs with excellent temporal resolution, using optical probes. The evolution can be resolved experimentally on a nanosecond timescale, which enables theorists to compare their theoretical predictions against experimental results. This verification allows us to make definite conclusions which are validated by both, experiments as well as by theory.

This thesis focusses on the various physical processes which are significant in a freely expanding UNP. The plasma expands due to the thermal pressure of the electrons. As the plasma expands, the electron thermal energy is converted into the ion expansion energy until essentially all the electron energy is expended and the ions reach terminal expansion velocity. Hence, at any given instant, the rate of UNP expansion is determined by the instantaneous electron temperature. A detailed study of the electron temperature evolution is critical to understand and control the plasma expansion. This thesis describes three different types of electron temperature evolutions, based on different regions of the parameter space of initial conditions. It presents the first clear, experimental and theoretical identification of the regimes in which elastic and/or inelastic processes are significant.

High initial electron temperature and/or low initial plasma density ($\Gamma_e < 0.2$)

constitute the first region of parameter space that was explored. In this region, there is no significant external source of energy during the plasma evolution so the UNP behaves as an adiabatic system. While the expansion is riddled with elastic collisions, the inelastic collisions are minimal. With a quasineutral, Gaussian distribution, the UNP undergoes self-similar Gaussian expansion and the ion and electron evolution can be described exactly by the analytical solutions of the Vlasov equations. This is an exciting discovery because this behavior of UNPs connects them to traditional hot plasmas and plasmas found in stellar systems. Hence, UNPs serve as model systems for these traditional plasmas and can shed light on the behavior of astrophysical plasmas.

The second region of parameter space refers to low initial electron temperature and/or high initial plasma density ($\Gamma_e > 0.2$) . The UNP is no longer an adiabatic system since many electron heating processes such as TL, DIH, TBR and R-e become significant and heat the electrons. This effect causes a non-adiabatic expansion in which the electron energy increases for the first few microseconds after plasma creation, until the rate of the inelastic collisions becomes negligible and cooling due to expansion starts to dominate. TL and DIH heat the electrons on a nanosecond timescale after photoionization while TBR and R-e are significant for 5 - 15 μs. TBR is a negative feedback effect so as the electron temperature increases, the rate of TBR decreases, and eventually becomes negligible when the electrons reach a temperature of 25-30 K. Radiative decay of Rydberg atoms formed due to TBR is a significant pro-

cess during plasma expansion and affects the rate of R-e collisions. Due to radiative decay, there are fewer high lying Rydberg atoms which can collide with electrons to either heat or cool them. Hence, R-e also becomes negligible after a few microseconds. As the electron heating processes become insignificant, the electron cooling due to adiabatic expansion starts to dominate.

Interpreting such a complicated electron evolution by simply observing the evolution of the ion velocity is difficult unless analytical solutions to the evolution are available. Hence, we collaborated with Thomas Pohl who simulated the evolution of the plasma with initial conditions from this parameter space. The effective ion velocity evolution from the simulations overlap perfectly with the experimental data. Combining experimental results with the simulations determined the exact electron temperature evolution as the UNP expands. The simulations also unravel the relative importance of the various physical processes which complicate the plasma expansion. In particular, the simulations confirm the importance of TBR, R-e and RD decay during plasma expansion; however, since the effect of TL is ignored in the simulations, its applicability to UNPs with a significant contribution from TL is still under question.

This study shows that the initial electron temperature and the initial density of the UNP determine the duration for which the electron heating processes are significant. For instance, if the initial electron temperature is less than 10 K, there are counteracting effects which heat and cool the electrons at the same time, prolong-

ing the time it takes to heat the electrons to high enough temperatures that these processes become insignificant. Simulations to untangle this complicated electron temperature evolution are underway and constitute a project for future work.

This thesis also includes an introduction to the evolution of UNPs created by exciting a gas of cold Rydberg atoms. This type of evolution was categorized as a third region of parameter space. Observing the evolution of the ion velocity, it was evident that there is tremendous heating of the electrons causing rapid expansion. However, the evolution of a UNP created from a dense Rydberg gas is complicated and depends on the process by which the Rydberg atoms evolve into a plasma. Whether the plasma is created in a few nanoseconds after photoionization, or in a few microseconds, would completely change the dynamics of the evolution. Interpreting such a tangled evolution requires a complete understanding of the ionization process and is beyond the scope of this study.

An interesting study for the future is to determine, with nanosecond resolution, how many ions are present in the Rydberg cloud as the cloud evolves. One of the challenges of this study comes from the fact that some of the highly excited Rydberg atoms would absorb the imaging beam and appear as ions in the images. Distinguishing between the Rydberg atoms and the ions would require exciting deeply bound Rydberg states; however, that affects the ionization rate of these low-lying Rydberg atoms to form a UNP. Despite the complications, this study will untangle the confusion about the spontaneous ionization of a cold, dense gas of Rydberg atoms to form

a UNP.

Another interesting study would be to observe Rydberg atom formation in a UNP through TBR, in a regime in which TBR theory breaks down. There is an on-going debate about the applicability of the existing TBR theory to UNPs. The theory behind TBR is based on the assumption that the electron Coulomb coupling parameter, $\Gamma_e < 1$, such that the electrons are not strongly coupled. This theory is valid for the UNPs in this study because the various electron heating processes decrease the coupling parameter to less than 1, rapidly after photoionization. Hence, pushing the electrons into the strongly coupled regime would require external cooling. Indirect cooling of the electrons by collisions with laser-cooled ions can help achieve and maintain cold enough temperatures during plasma evolution that the electron coupling parameter remains greater than 1. These collisions would bring the UNP into a regime where a new theory would be required to explain the recombination process as the UNP evolves.

Shock waves make a case for another interesting study in UNPs. Shock waves appear in the form of a density spike during plasma expansion. In this study, due to the loss of ions from collisions with atomic beam, the signal to noise degraded over time enough to prevent a clear sign of the appearance of shock waves. However, shock waves form an integral part of plasma expansion and cannot be ignored. With the inclusion of the shutter in the experimental set up, the ion loss problem has been overcome. Hence, an experiment targeted towards observing shock waves in a UNP is

no longer an impossible task. Further investigation of plasma expansion can unravel the mystery behind the possibility of observing shock waves in a UNP.

The study of plasma expansion in this thesis involved certain assumptions. One of the assumptions was that the thermal energy of the ions is negligible compared to their expansion energy. Hence, the temperature of the ions was assumed constant over the whole plasma cloud. It was also assumed to be constant in time, at its initial value after DIH, and did not change as the plasma evolved. While these assumptions are valid for this study, an interesting question about the ion thermal energy evolution remains. A study of the ion temperature will determine whether the ions remain strongly coupled throughout the expansion or if they are heated enough to be pushed out of the highly correlated regime.

This study on the ion temperature evolution will assist in the execution of one of the most interesting experiments in the field of UNPs, which is laser cooling of the UNPs. Laser cooling of an ultracold neutral plasma will increase the ion Coulomb coupling parameter by many orders of magnitude. The resulting strong coupling of ions will enable us to observe collective effects such as ion-acoustic waves and phase transition into Wigner crystallization. The importance of the study of plasma expansion described in this thesis factors into the investigation of the possibility of cooling the ions to cold enough temperatures for strong coupling.

This thesis comprises a comprehensive study of the ion and electron evolution as a UNP expands. Equipped with the knowledge of how much the ions and electrons

heat up when a UNP is created under different initial conditions, we can estimate the amount of cooling force needed to counteract the heating effects. It also enables us to determine the region of parameter space where strong coupling can be achieved with greatest ease. In short, this thesis provides a detailed and complete understanding of UNPs, and serves as a great source of reference for unraveling the mysteries that riddle the creation and evolution of UNPs.

Appendix A

Ion number evolution

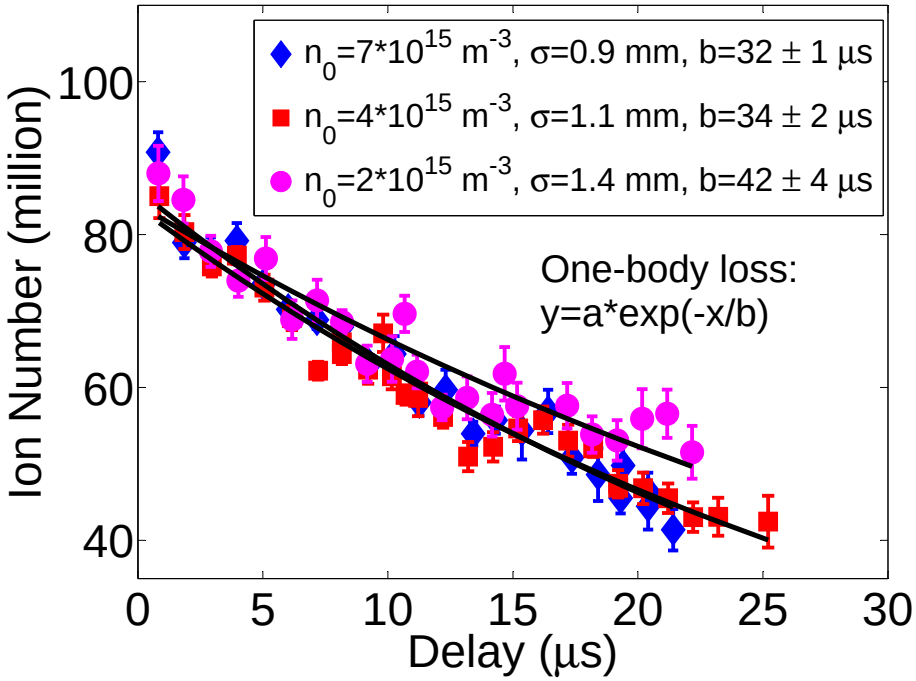

Figure A.1: The figure shows the number of ions for different initial plasma cloud density versus delay after photoionization. The loss of ions during plasma expansion does not depend on the initial density of the plasma cloud as is evident from the rate of loss given by the inverse of the quantity "b". The slight difference in the rate of loss is due to many-body effects such as TBR.

While performing the experiments on UNP expansion, as many as 50% of the ions were lost within $20\,\mu s$ after photoionization. The only process which causes a loss of ions during expansion is TBR. A theoretical estimate of the number of ions

lost due to TBR was much less than the loss observed in the experiments. In order get an insight into the cause of the ion number loss, the number loss was studied under various initial conditions. Fig. A.1 shows the loss in ion number in UNP with $2E_e/3k_B = 14\,K$ for three different plasma densities. As is evident in the figure, the loss rate does not depend on the density of the plasma. The rate of loss is similar to a one-body loss rate. Using the one-body loss rate equation, $y = a * exp(-x/b)$, rate of loss, given by b^{-1}, was determined. The loss rate for the three datasets are similar with slight differences due to many body effects such as three-body recombination which adds to the ion loss. The rate of TBR is higher for higher density data and is reflected in the slight difference in the rate of loss for the datasets. So the rate of loss is highest for the highest density data.

Fig. A.2 shows three datasets with the same initial density of $2 * 10^{15}\,m^{-3}$ and initial cloud size of 1.6 mm, for three different initial electron temperatures of 3 K, 14 K and 37 K. The figure shows that at this low density, the rate of loss does not depend on the initial electron temperature. The data was fit to the one-body loss expression and the inverse of the rate of loss obtained from the fit is displayed in the figure. Within the uncertainties, the rate of loss is the same for all three datasets.

At higher initial electron temperatures, the rate of loss does seem to depend strongly on the electron temperature as is evident in Fig. A.3. The figure shows the rate of loss for two datasets with same initial density of $3 * 10^{15}\,m^{-3}$ and initial cloud size of 1 mm, and two different initial electron temperatures of 60 K and 116 K. The

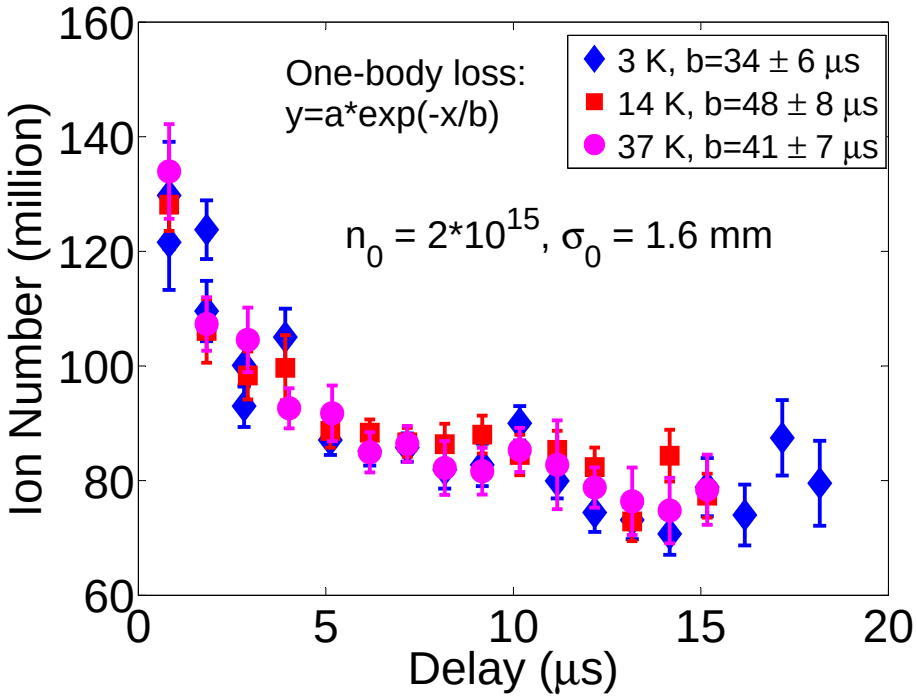

Figure A.2: The figure shows the number of ions versus delay after photoionization for $2E_e/3k_B = 10$, 14 and 37 K. The loss of ions during plasma expansion, for very low plasma density, does not depend on the initial electron temperature. Within the uncertainties of the fit, the loss rate, "b", is the same for all three datasets. The fit is not plotted in the figure to display the data clearly.

rate of loss for the 116 K data is considerably higher than the 60 K data. Equipped with all this knowledge, we hypothesized the reasons why we were losing so many ions with delay after photoionization.

One of the suspicions was that the vacuum might have degraded over time and so there were collisions with background gases which resulted in a one-body loss in the UNP. Another hypothesis was that there might be some build up of charges inside the vacuum chamber and on the glass viewports. These charges can create an electric field in the vacuum chamber which can cause some ion and electron motion resulting in a loss in the number of ions visible through the probe beam. Hence, we opened

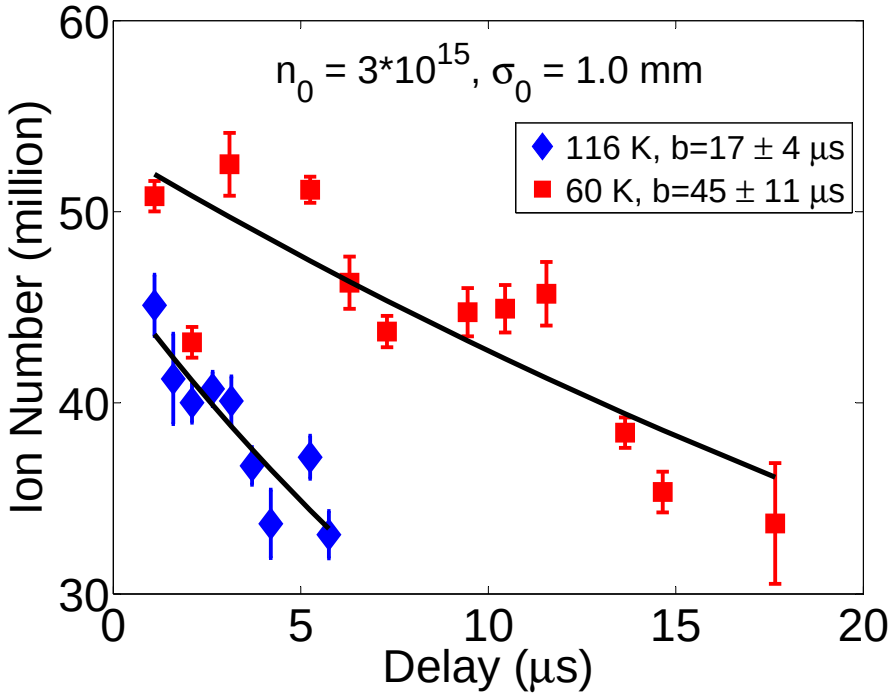

Figure A.3: The figure shows the ion number evolution for $2E_e/3k_B$ =60 and 116 K. The rate of loss of ions is greater for higher initial electron temperature. 'b' refers to the inverse of the rate of loss, which is greater for lower initial electron temperature.

up the vacuum chamber and flushed it with an inert gas to remove the stray charges in the vacuum chamber. Then we brought it down to ultra-high vacuum again. This cleaning of the vacuum chamber seemed to improve things only marginally. We still saw a large enough ion number loss with delay after photoionization to cause concern.

The next step we took was to introduce a shutter in the path of the atomic beam as it travels from the reservoir to the MOT chamber. The hot atoms could be colliding with the ions and causing the ion loss. Fig. A.4 shows a schematic of the timing sequence that was followed to ensure that no hot atoms were introduced into the MOT while imaging the plasma. The shutter blocked the atomic beam once the MOT was completely loaded. The plasma image loop and background image loop

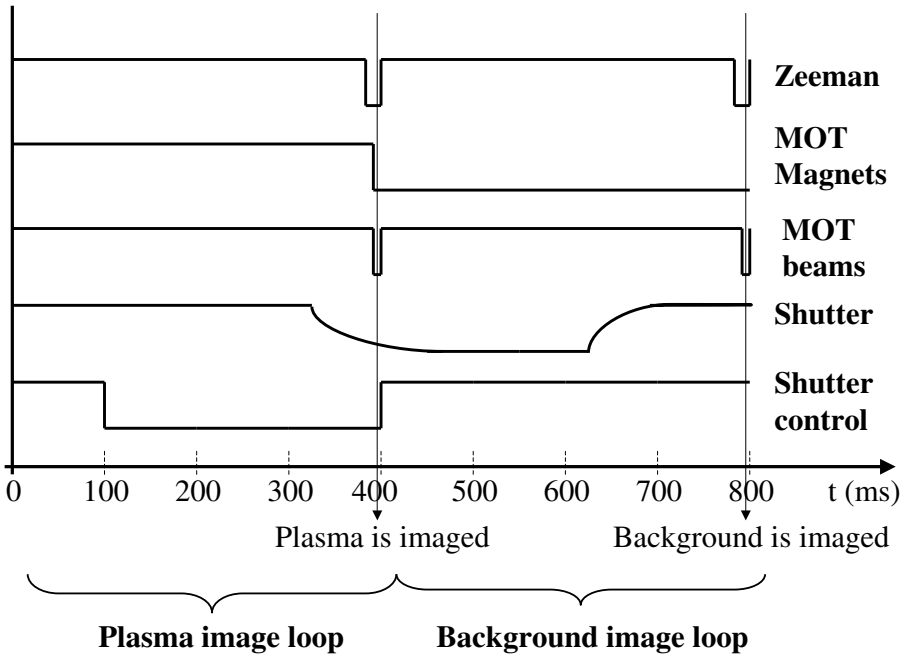

Figure A.4: The figure shows the timing sequence for the plasma and background images taken with the shutter incorporated in the system. The shutter blocks the atomic beam from entering the vacuum chamber and colliding with the ions while we take images of the UNP. The shutter, being a mechanical system, is the slow component of the experimental system. It takes about 200 ms to respond to the computer control and an additional 100 ms to completely open and close. Hence, the timing for the rest of the apparatus is set up to accommodate the shutter timing.

refers to the part of the timing sequence in which the plasma image and background image respectively are taken. The shutter would block any hot atoms from colliding with the plasma while the plasma image is being taken. In the background image loop, we do not need to block the hot atoms since we do not form a plasma. The shutter is controlled by a pneumatic actuator which can be controlled by the computer through a digital-to-analog converter. The shutter, being a mechanical system, is slow and takes about 200 ms to respond to the computer control and $\sim$ 100 ms to open and to close completely.

After ~ 100 ms from the beginning of the plasma image loop, the shutter is given the signal to close. The shutter takes 300 ms after that to close completely. Meanwhile the MOT beams, MOT magnets and Zeeman beams are turned on and the MOT is loaded. We do not need to wait for the shutter to close completely because the shutter blocks the atomic beam even when it is only $60-70\%$ closed. Once the MOT is fully loaded, we wait for the MOT fluorescence signal to decrease by $\sim 10\%$, indicating that there are no more hot atoms coming into the MOT chamber and being loaded into the MOT. Then we photoionize these laser-cooled atoms to create a UNP and image the ions. The shutter is reopened after the image beam is turned off ensuring that no hot atoms have collided with the ions while the plasma is expanding. Note that, according to the schematic shown in Fig. A.4, there are a lot more time delays introduced in the plasma and background image loop than is required. The delays are introduced to adjust the time of the arrival of the photoionizing beam in the two loops, because we do not control the dye laser pulse and it arrives every 100 ms.

Figs. A.5 and A.6 show the ion number with delay after photoionization for initial electron temperature of 25 K and 60 K, respectively. Both figures show one dataset with the shutter incorporated in the system and one without the shutter. Clearly the data with no shutter in the set up shows an ion loss while the one with shutter in the set up does not show any significant decrease in the ion number. The data is fit to the one-body loss expression. While the data is noisy, the rate of loss shown in the figure for the different datasets gives a clear indication that if we block the atomic

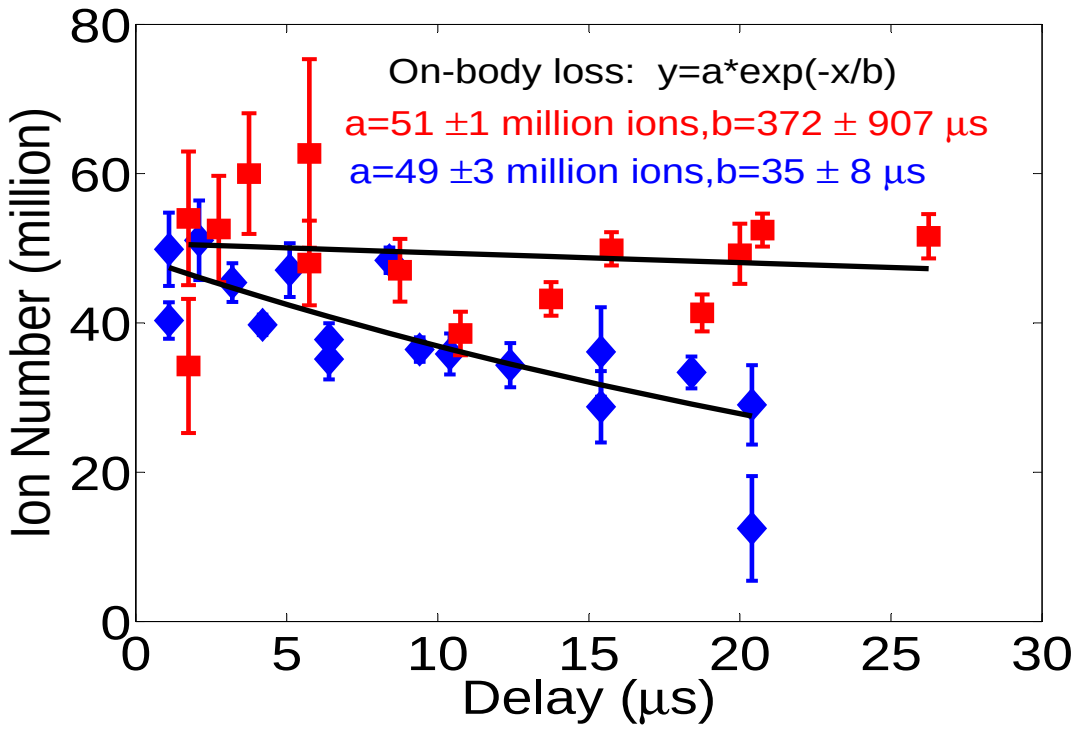

Figure A.5: The figure shows the ion number loss in UNP for two datasets with $2E_e/3k_B = 25\,K$. The diamonds are data showing ion number loss that we observed when we did not have a shutter incorporated in the experimental system. The squares show the data with the shutter blocking the atomic beam during plasma expansion. The red text shows the one-body loss rate for the dataset with no ion loss and the blue text shows the rate for the dataset with the ion number loss. While the data is noisy in the first few μs, it is evident that there is negligible loss of ions even at long delay times with the shutter incorporated in the system.

beam during plasma expansion, the ion number does not decrease with delay after photoionization.

The loss of ions was a one-body loss which does not depend on density. Hence, for UNPs created in a regime where no density dependent processes are significant, the ion loss does not affect the effective ion velocity and electron temperature evolution. Therefore, even though the data for UNPs undergoing self-similar Gaussian expansion has ion loss with time, the theoretical curves still overlap very well with

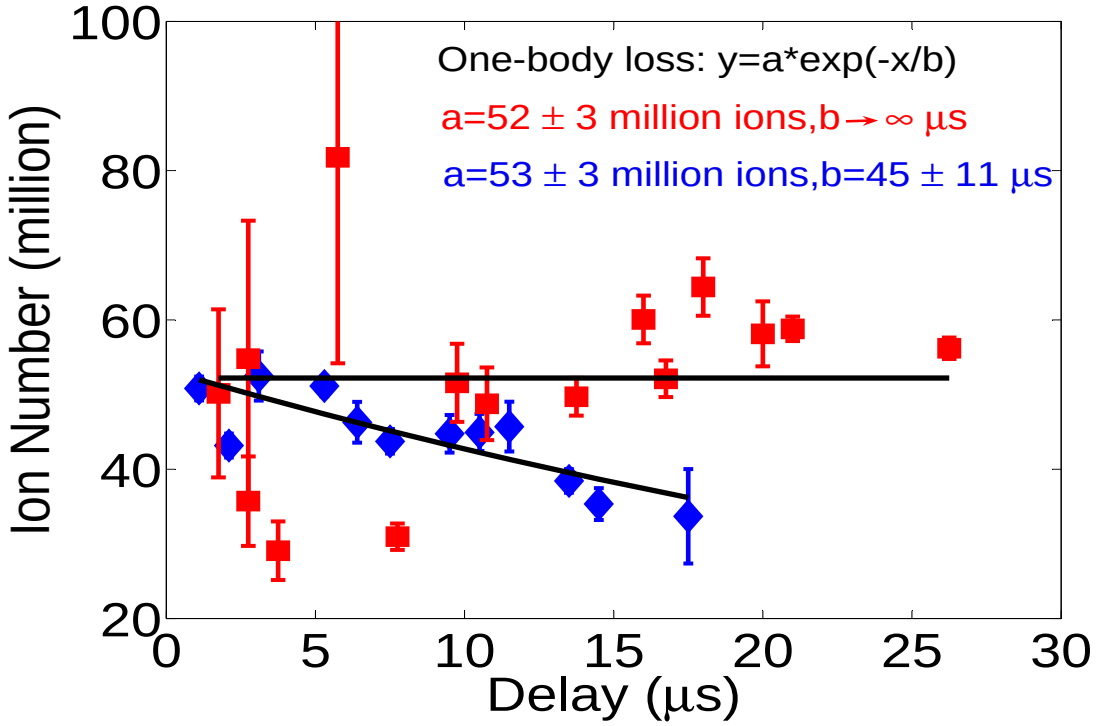

Figure A.6: The figure shows the loss of ions with time for two datasets with $2E_e/3k_B = 60\,\mathrm{K}$. The diamonds are data showing ion number loss that we observed when we did not have a shutter incorporated in the experimental system. The squares show the data with the shutter blocking the atomic beam during plasma expansion. The red text shows the one-body loss rate for the dataset with no ion loss and the blue text shows the rate for the dataset with the ion number loss. While the data is noisy in the first few μs, it is evident that there is no loss of ions even at long delay times with the shutter incorporated in the system. (For clarity, the ion numbers in the "no-loss" data were scaled to match the initial number of ions in the dataset with ion loss).

the experimental results of effective ion velocity evolution.

Under conditions in which the density dependent processes are significant, the theory curves for electron temperature evolution show that these processes are significant only during the first few microseconds after plasma creation. Within this time, there is no significant loss in the ion numbers. The loss becomes significant in comparison to the initial number of ions in the UNP on a time scale of $15 - 20\,\mu s$. In

future, we would like to explore the dependence of the ion number loss on the high initial electron temperature as is evident in Fig. A.3.

Due to the ion number loss, the signal to noise degraded tremendously with delay after photoionization which prevented us from observing the effective ion velocity evolution and plasma cloud size evolution for long delays. It especially hindered the ability to observe a considerable variation in the size to obtain a good fit to the theoretical cloud size evolution given by Eq. 4.2. Therefore, we were not able to verify the self-similar Gaussian expansion using the size evolution. It would be interesting to get data under the conditions for ideal expansion in which no density dependent processes are significant and verify the self-similar Gaussian nature of the expansion using both the size and effective ion velocity evolution and show consistency in the value of T_{e0} from both fits.

Appendix B

Indium cell

The pulsed dye laser that is used to photoionize laser-cooled Strontium atoms is tunable from 395 - 420 nm. In order to tune the wavelength of the laser, we rotate the angle of the diffraction grating which forms one end of the laser cavity. The grating sits on a rotatable mount attached to a counter which keeps track of how much we have tuned the wavelength. The counter reading does not directly read the wavelength. Instead it reads a number which is a multiple of the wavelength with some offset. In order to determine what wavelength the counter readings correspond to, we needed to calibrate the counter. My Master's thesis [51] describes how we calibrated the counter reading to determine the wavelength of the dye laser. One of the methods we used was to excite Rydberg atoms and compare the counter readings corresponding to the various Rydberg peaks to known values of Rydberg energy levels [85]. However, due to the laser linewidth and other broadening mechanisms in the Rydberg gas there was some uncertainty in this method since it is difficult to exactly determine the quantum level that the Rydberg peaks correspond to. The assignment of the quantum level could be offset by ± 1.

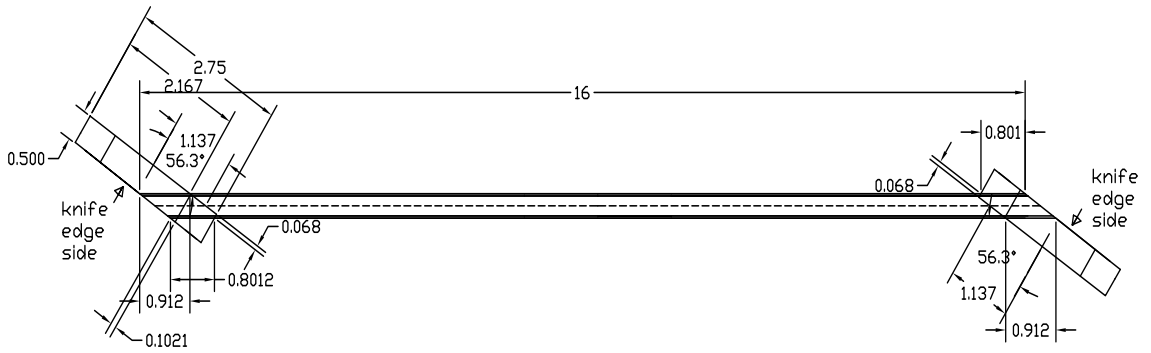

Figure B.1: The figure shows the Indium absorption cell. The viewports were soldered close to Brewster's angle to prevent multiple reflections from the glass that can lead to etaloning effect and power loss.

In order to get a better calibration, we excited the $5^2S_{1/2} \rightarrow 5^2P_{3/2}$ transition in the Strontium ion at 407 nm, in a discharge cell and included the counter reading corresponding to this wavelength with the Rydberg data. However, this wavelength is far from the normal operation region of 410 - 412 nm. Also, the 407 nm wavelength is far from the wavelength we used to excite the Rydberg peaks. We needed to include a data point within the 410 - 412 nm range to help determine the calibration of the counter more precisely.

Indium atoms have a 5p $^2P_{1/2} \rightarrow$ 6s $^2S_{1/2}$ transition at 410.175 nm with a natural linewidth of 8.9 MHz. Hence, we built an absorption cell for Indium to excite the 410.175 nm using the pulsed dye laser to help calibrate the counter better. The cell needed to be built of stainless steel since we would have to heat it to 800 - 1000 K to vaporize Indium under pressure. As shown in Fig. B.1, we use a 16 in long tube made of stainless steel and hard solder it to vacuum flanges on both sides. We wrapped a heater coil on the cell which enabled us to heat the cell to 650° C when we applied a

voltage of 40 V and 2.11 A current to the coil. The heater coil is also hard soldered on to the Indium cell.

Then we connected the Indium cell to a vacuum pump and used the heater coil to bake out the cell. We did not want to heat the cell too much since the Indium might evaporate and stick to the edges of the cell or the glass ports in the absence of any background gas. The pressure needed in the Indium cell was determined by following calculations: The absorption cross-section is given by

$$\alpha_{0,In} = \frac{3\lambda^2}{2\pi}. \tag{B.1}$$

But Doppler shift and laser linewidth cause it to be of the form,

$$\alpha_{In} \approx \alpha_{0,In} \frac{\gamma_0}{\sqrt{\gamma_{Doppler}^2 + \gamma_{laser}^2}}, \tag{B.2}$$

where

$$\gamma_{Doppler} = \frac{1}{\lambda}\sqrt{8ln(2)\frac{k_B T}{m}}, \tag{B.3}$$

γ_0 is the natural linewidth of the transition, $\gamma_{Doppler}$ is the Doppler broadened linewidth of the transition, T is the temperature of the cell, m is the mass of Indium atom. We also need to include the effects of the dye laser linewidth and power broadening when we calculate α_{In}. For $\lambda = 410.175\,nm$, $m = 126.9 * 10^{-3}/(6.023 * 10^{23})\,kg$, $T = 873\,K$ we get $\gamma_{Doppler} = 1.4\,GHz$. The dye laser linewidth is $\approx 12\,GHz$, hence, we assume an upper limit on $\sqrt{\gamma_{Doppler}^2 + \gamma_{laser}^2}$ to be $2\pi * 15\,GHz$. Therefore, with

$\gamma_0 = 2\pi * 8.9\,MHz$, we get an absorption cross-section, $\alpha_{In} \approx 5 * 10^{-17}\,m^2$. Using Beer's law,

$$I = I_0 e^{-nl\alpha_{In}} \tag{B.4}$$

where I is the intensity of the incident light, I_0 is the saturation intensity of the transition, n is the density of the interaction region and l is the length of the interaction region. Assuming, $I = 0.5I_0$ and $l = 0.1\,m$, we get $n = 1.5 * 10^{17}\,m^{-3}$. From ideal gas law, $P = dRT$, where P is the pressure, d is number of moles in a cubic meter volume and R is the gas constant. Putting in the value of $d = n/m$, R and T in the ideal gas law equation gives a vapor pressure of $1 * 10^{-5}\,Torr$ needed in the Indium cell.

A vacuum pressure of $\sim 10^{-7}\,Torr$ was sufficient to ensure a clean cell for our purposes. We wanted a background pressure of $\sim 1\,Torr$ to prevent the Indium from sticking to the glass flanges. With a background pressure of $1\,Torr$, we were sure that the mean free path of the atoms was short enough to prevent them from reaching the vacuum flanges at the ends of the cell. So once we reached the vacuum pressure of $10^{-7}\,Torr$, we filled the cell with Argon until the pressure in the cell was close to $1\,Torr$.

In order to reach a temperature higher than what the heater coils would allow us to obtain, we enclosed the Indium cell in a ceramic heater. To ensure a good heat transfer, we covered the cell with fiber glass before enclosing it in the ceramic heater. The ceramic heater enabled us to increase the temperature of the cell by $\sim 100^\circ C$.

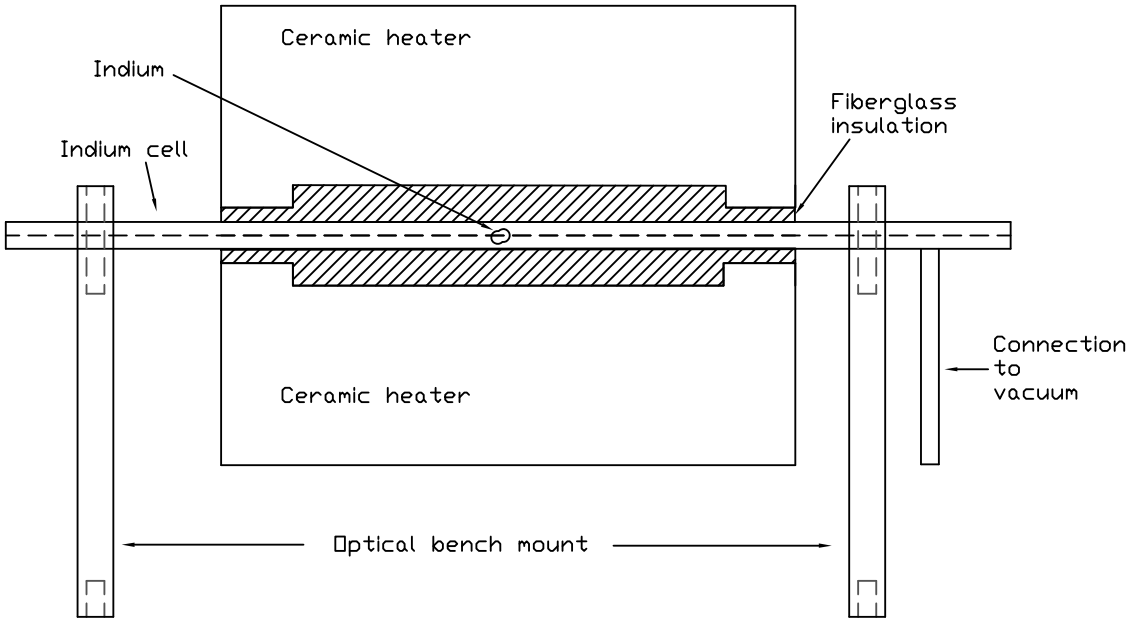

Figure B.2: The figure shows the Indium cell inside the ceramic heater. In order to heat the cell up to 800°C, the cell is wrapped with heater wire (not shown in the figure) and then enclosed in a ceramic heater. The fiber glass helps with heat conduction from the heater to the cell. The cell can be connected to a vacuum pump to reach high vacuum pressures.

Fig. B.2 shows the arrangement of the Indium cell enclosed in the ceramic heater.

Then we set up the optics for double passing the pulsed dye laser beam through the Indium cell. Since the pulsed dye laser has a high shot to shot noise, we set up two photo detectors. One detected the laser beam before it passed through the Indium cell and another after a double pass through the cell. By subtracting the signals from the two photodiodes, we were able to get rid of the shot to shot noise. The diffraction grating mount is connected to a rotary encoder. The rotary encoder was connected to a stepper motor driver which allowed us to scan the wavelength of the dye laser. As we scanned the laser, we recorded the signals from the two photodiodes. To observe the absorption signal, we subtracted the signal at the photodiode before the cell from

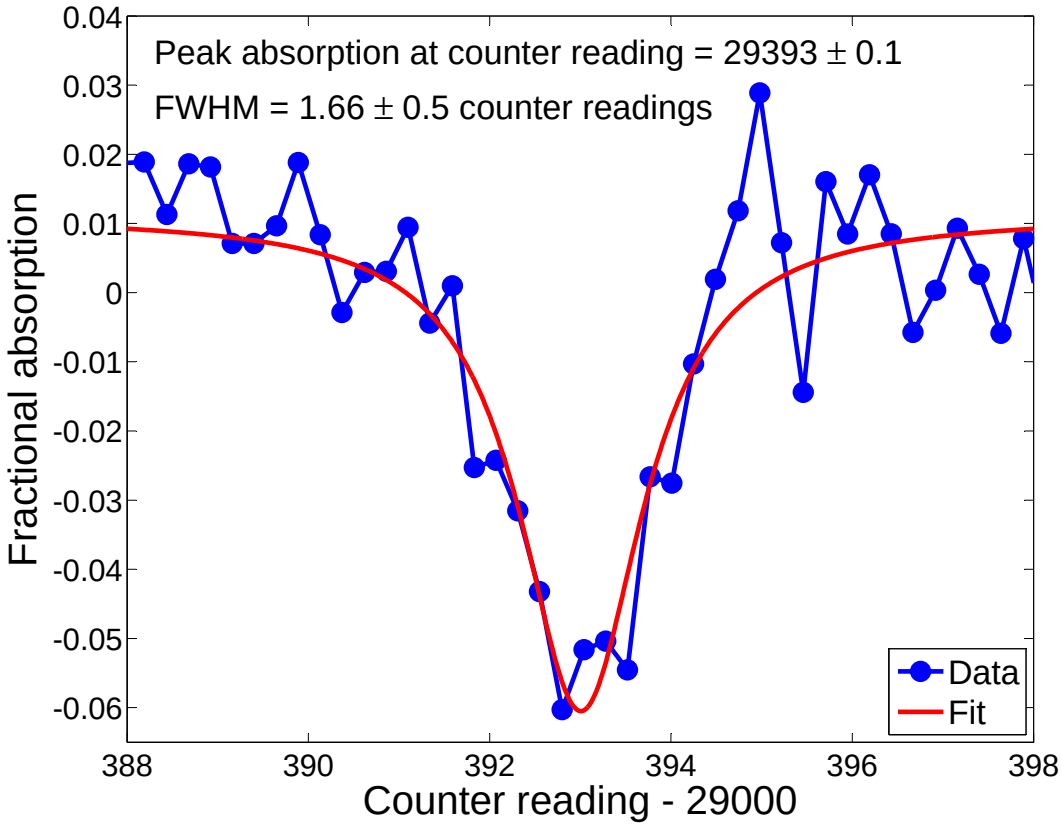

Figure B.3: The figure displays a typical dataset showing the Indium absorption line in units of counter reading. The counter reading at peak absorption corresponds to the Indium peak absorption wavelength of 410.175 nm.

the one after the cell. The absorption signal appeared as a dip in the signal when the laser linewidth was resonant with the absorption line. Fig. B.3 shows one such data set displaying the absorption line of Indium in units of counter reading. To obtain the counter reading corresponding to peak absorption, we minimize the χ^2 with the function,

$$f = -a\frac{\gamma/2}{(x - counter)^2 + (\gamma/2)^2} + offset \tag{B.5}$$

where $offset$ takes care of any overall offset in the signal from the baseline, a is

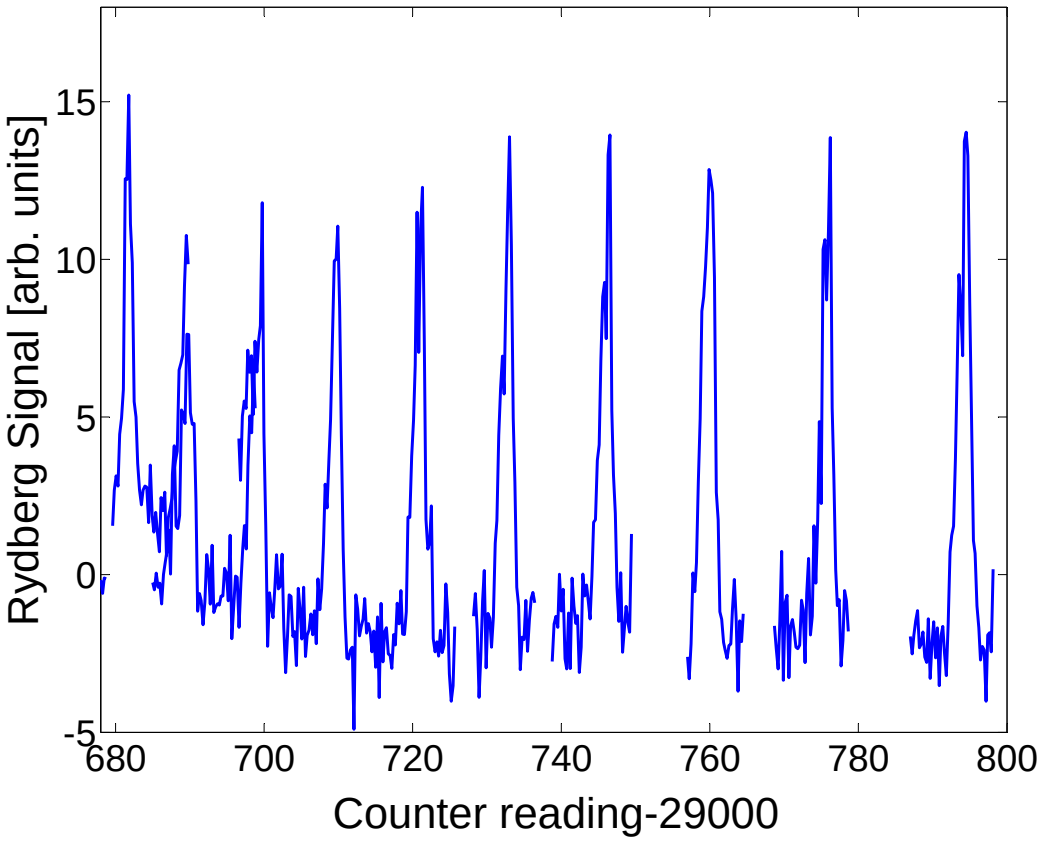

Figure B.4: The figure shows the location of the various Rydberg peaks in units of counter readings. (The x-axis is plotted as shown for greater resolution on the readings). The data of location of Rydberg peaks can be compared with known location of Rydberg peaks in wavelength units which can help calibrate the counter.

the measure of the absorption fraction, γ is the FWHM of the absorption signal and *counter* gives the exact counter reading corresponding to the resonant absorption wavelength of Indium. As shown in Fig. B.3, the peak absorption occurred at counter reading $= 29393 \pm 0.1$ which represents a wavelength of 410.175 nm.

In order to calibrate the counter, we needed some more data connecting the counter readings to known wavelengths. Hence, we decided to excite Rydberg atoms again at known wavelengths [85] using the pulsed dye laser. This method is described

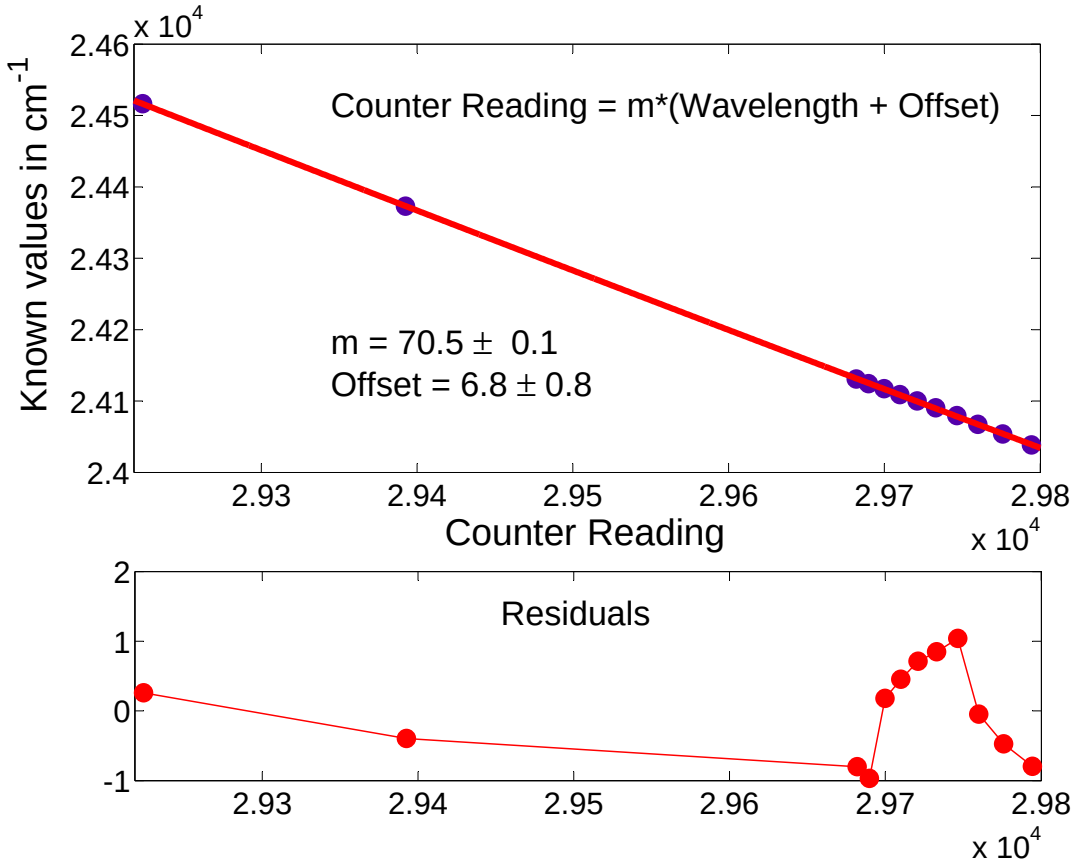

Figure B.5: The figure shows the calibration of the counter. By recording known absorption lines and Rydberg levels in units of counter readings, a comparison could be made between the known values in units of wavelength or wavenumber and counter reading. The data was then fit to a straight line equation to determine the parameters m and Offset which relate the counter readings to corresponding wavelengths. The figure also shows the residuals from the fit which are minimal confirming the goodness of fit.

in detail in [51]. We monitored the fluorescence signal from the MOT and every time we excited the atoms to a Rydberg level, the signal would decrease tremendously. The inverse of these dips in the fluorescence signals is shown in Fig. B.4. The MOT was maintained at a very low density $\sim 10^{15}\, m^{-3}$ to prevent broadening of the absorption lines due to collisions. We compared the location of the Rydberg peaks in units of counter reading with known wavelengths of the Rydberg levels. Equipped

with this information, along with the value of the counter reading corresponding to the Indium absorption line, we were able to obtain a good calibration of the counter reading. Fig. B.5 shows the counter reading to wavelength calibration for the pulsed dye laser. Hence, we obtained a better calibration of the counter reading as

$$CouterReading = 70.47 * (Wavelength(nm) + 6.81). \tag{B.6}$$

Appendix C

Offset lock

In order to study UNP expansion for long delays after photoionization, we needed to be able to scan the probe beam frequency by $\sim 500\,\mathrm{MHz}$. An arrangement of acousto-optic modulators could not give us that scan range without the loss of beam power. So we resorted to an offset lock mechanism which enabled us to scan the frequency of the probe beam over a large range with no beam power loss. The probe beam at 422 nm is generated by frequency doubling the 844 nm output of a diode laser. The lock system used the 922 nm output of the Ti:Sapph laser which is frequency doubled to generate the 461 nm light. The 461 nm light is locked to the atomic transition with the help of saturated absorption spectroscopy. The basic idea was to lock a Fabry-Perot cavity to the 922 nm light and then lock the 844 nm laser to the Fabry-Perot cavity. A schematic of the Fabry-Perot set-up is shown in Fig. C.1.

The mirrors on the Fabry-Perot cavity are partially reflecting with $98 \pm 1\%$ reflectance centered at 940 nm. The mirrors are concave with radius of curvature =

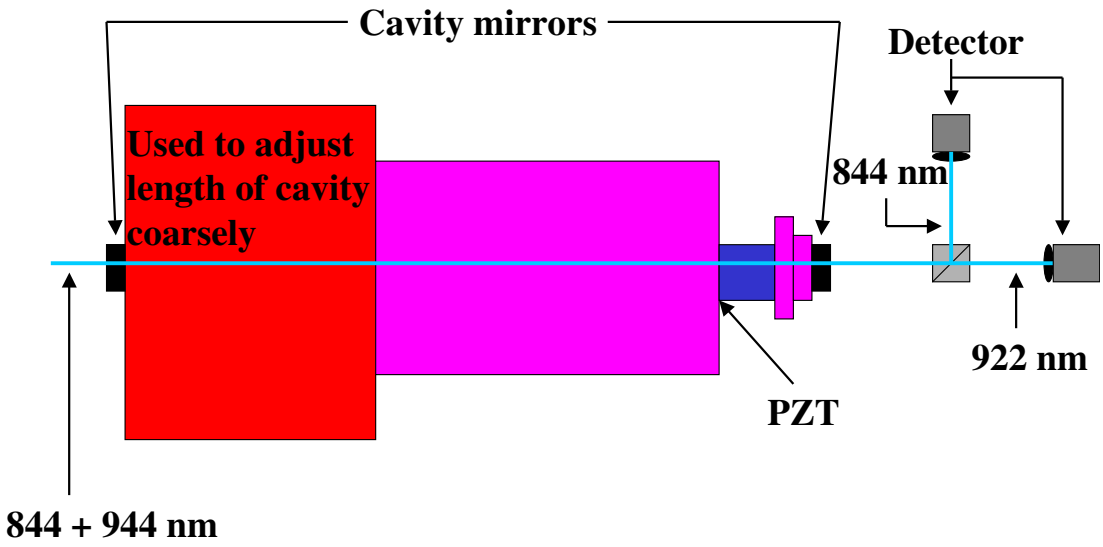

Figure C.1: The figure shows the Fabry-Perot cavity which is used to offset-lock the 844 nm laser to the 922 nm laser. The big red part of the cavity can be screwed in and out to make coarse adjustments to the length of the cavity. The cavity mirrors have 98% reflectance. A PZT is used to scan the cavity which helps lock the cavity and the lasers. The 844 nm and 922 nm light are overlapped perfectly and sent through the cavity. The two beams have different polarizations which facilitates separating them with the help of a polarizing beam splitter cube when they come out of the cavity.

0.15 m. The finesse of the cavity is,

$$\mathcal{F} = \frac{\pi}{2}\sqrt{\frac{4R}{(1-R)^2}} \tag{C.1}$$

For R = 0.98, $\mathcal{F} = 155.5$. The free spectral range (FSR) of the cavity is ~ 1 GHz.

Therefore, the $FWHM = FSR/\mathcal{F} = 6.4\,MHz$.

In order to bring the 422 nm light close to the Sr^+ resonant transition, we scan the 844 nm laser to excite three transitions in Rubidium. Rubidium conveniently has three transitions which are 425.5, 483 and 540.5 MHz away from the Strontium ion resonance. (The Rb line which is 425.5 MHz away from the Sr^+ has the highest absorption cross-section so we shall refer to it as the biggest line). We built a Rubidium saturated absorption spectroscopy setup to excite the Rb transitions. Using an AOM in a cats-eye setup, we established that when the laser was on resonance with the biggest Rb line, it was 200 MHz below the Strontium ion resonance. Then we used another AOM to shift the laser frequency up by 200 MHz to bring it on resonance with the Strontium ion. Hence, when we center the laser to the biggest Rb line, we are essentially bringing it on resonance with the Strontium ion transition.

The three Rb transitions are separated by 57.5 MHz each. When we scan the 844 nm laser, the three lines are visible on the oscilloscope at a frequency of $\sim$ 355480.6 GHz. Before we lock the 844 nm laser to the Fabry-Perot cavity, we bring it close to the Rubidium transitions. Then we lock the Fabry-Perot cavity to the 922 nm laser first and then lock the 844 nm laser to the Fabry-Perot cavity.

A brief explanation of how the offset-lock circuit works is given here. With the help of the PZT, as shown in Fig. C.1, the Fabry-Perot cavity is scanned by 10 V (peak-peak), centered around 0 V, at $\sim$ 200 Hz. We scan using a Sine wave instead of a triangular wave since the lock circuit was coming out of lock close to the sharp edge of the scan. As we scan the cavity, the photodetectors pick up a 922 nm and a

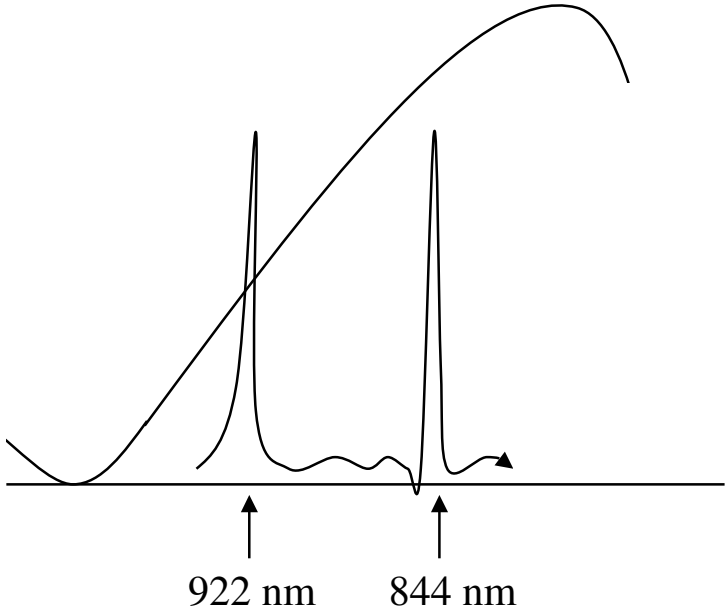

Figure C.2: As we scan the Fabry-Perot cavity, the 844 and 922 nm beams show peak transmission at different scan voltages. The scan is chosen to be a Sine wave to avoid any sudden voltage changes.

844 nm transmission signals at two different scan voltages, as shown in Fig. C.2. This scan voltage and the transmission peaks are input to the offset-lock circuits. The circuit to lock the Fabry-Perot cavity to the 922 nm laser is shown in Fig. C.4 and the circuit to lock the 844 nm laser to the Fabry-Perot cavity is shown in Fig. C.5. With the help of 'sample and hold' chips (LF398N), we can pick out the exact scan voltage at which the 844 and 922 nm beams show peak transmission. We lock the peak transmission of the 922 nm light at 0 V of the scan. As shown in Fig. C.3, we add the sample and hold (S/H) output from the two circuits and an external voltage which we can scan. With this, we can generate an error signal as we scan the 844 nm laser which can be integrated and sent to the 844 nm laser. This locks the 844 nm laser to the Fabry-Perot cavity. Now as we scan the external voltage, the 844 nm

sample and hold output would compensate for the change, to keep the laser locked, implying a change of the output frequency of the 844 nm laser which in turn will scan the probe beam.

After locking the laser, we scan the frequency of the 844 nm laser and observe the absorption signal from the Rb cell. This tell us exactly what offset voltage to the laser brings us on resonance with the biggest Rb absorption line. The scan also tell us the relation between unit change in voltage corresponding to a unit change in frequency. For example, suppose a 1 V change in the offset voltage causes a 60 MHz change in the second harmonic of the 844 nm laser and the center of the biggest Rb absorption line is at an offset voltage of 0 V. Then in order to scan $\pm 120\,MHz$ around the strontium ion resonance, we would scan the offset voltage from -2 to +2 V. This system of offset-lock gives us a total scan range of more than $500\,MHz$ which is sufficient to study UNP expansion.

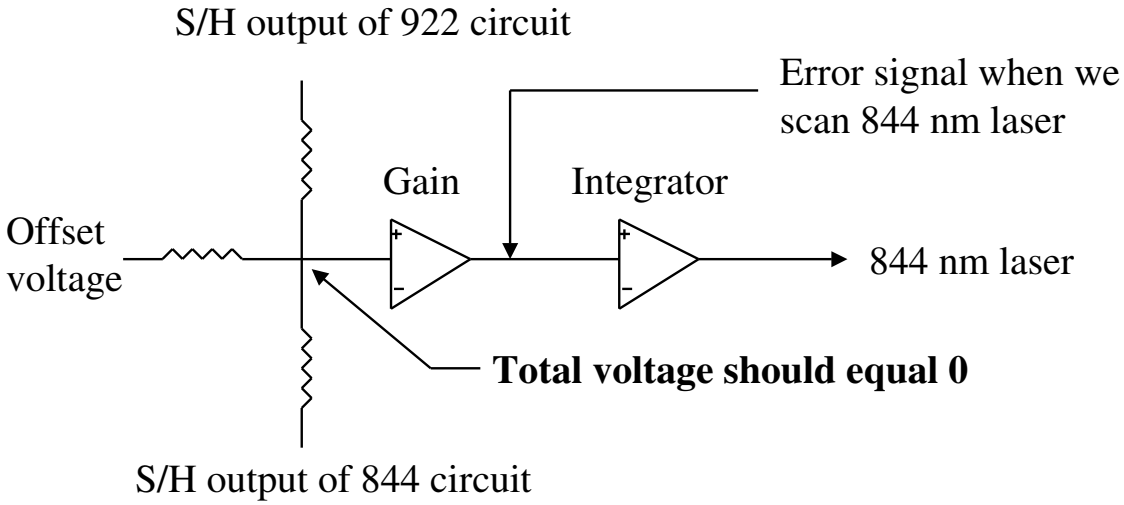

Figure C.3: The figure shows a schematic of the last steps to lock the 844 nm laser to the Fabry-Perot cavity. The sample and hold output of the 844 nm and 922 nm circuits and an external voltage are sent to a summing junction. The total voltage at this junction should be zero to enable the circuit to keep the 844 nm laser locked. When an external perturbation shifts the laser frequency away from the desired point, the summing junction is no longer at 0 V and the integrator integrates that voltage to provide a negative feedback to the 844 nm laser to compensate for the perturbation.

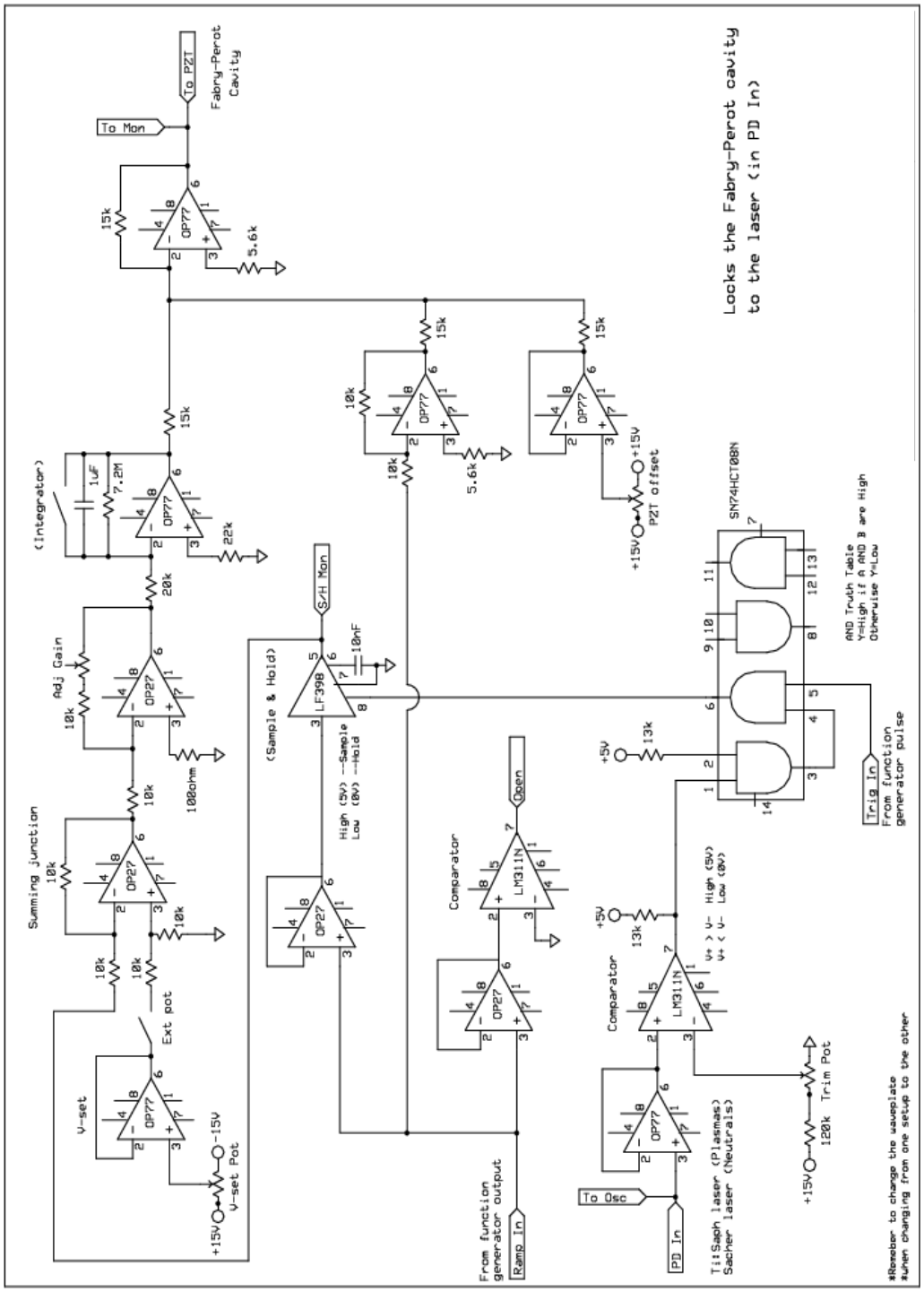

Figure C.4: The figure shows a schematic of the circuit used to lock the Fabry-Perot cavity to the 922 nm output of a Ti:Sapph laser.

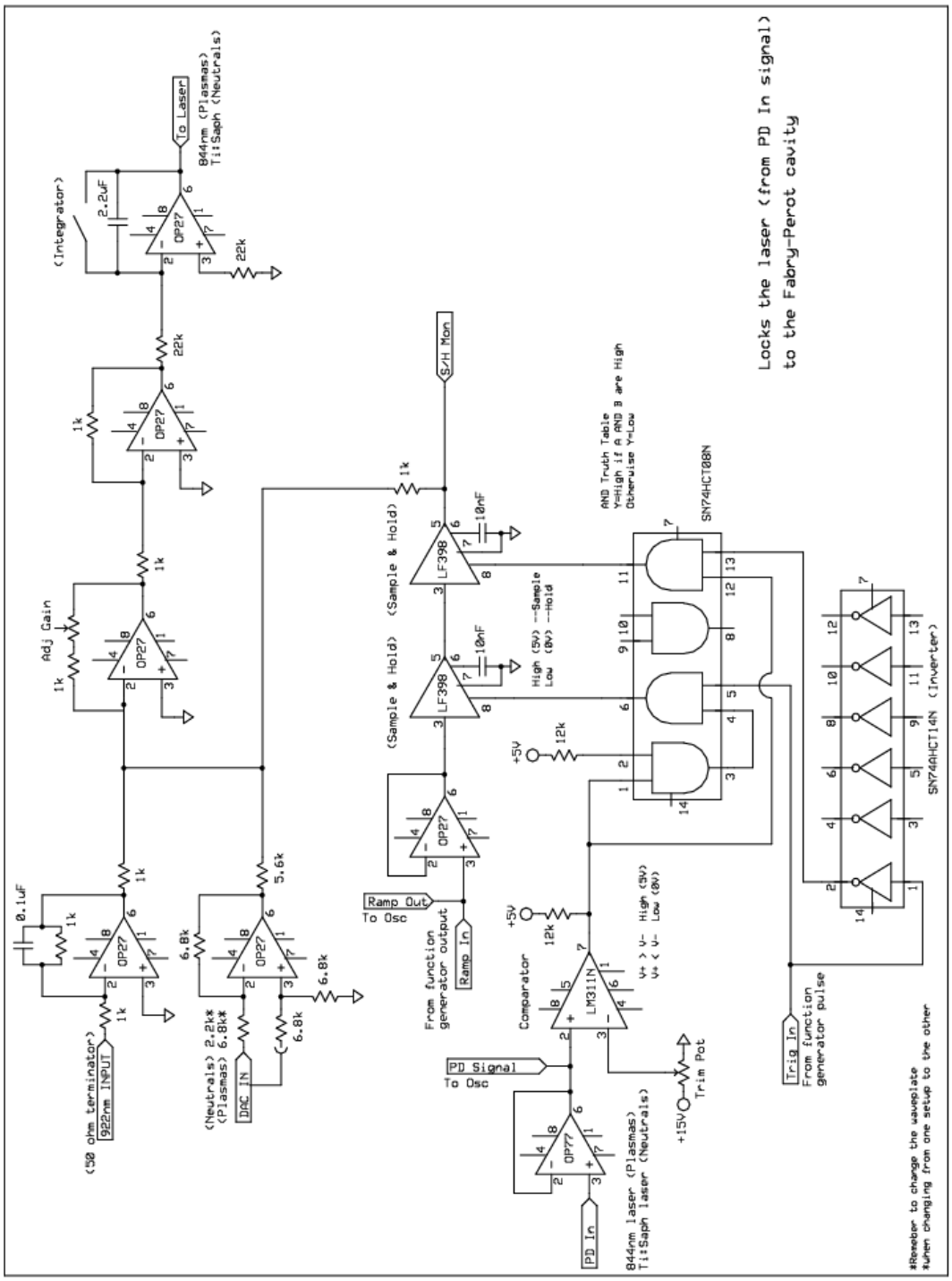

Figure C.5: The figure shows a schematic of the circuit used to lock the 844 nm output of a diode laser to the Fabry-Perot cavity which is locked to the 922 nm output of a Ti:Sapph laser.

Bibliography

[1] T. Pohl, T. Pattard, and J. M. Rost. "Coulomb crystallization in expanding laser-cooled neutral plasmas." *Phys. Rev. Lett.* **92**(15) 155003 (2004).

[2] H. M. Van Horn. "Dense Astrophysical Plasmas." *Science* **252** 384 (1991).

[3] M. Nantel, G. Ma, S. Gu, C. Y. Cote, J. Itatani, and D. Umstadter. "Pressure Ionization and Line Merging in Strongly Coupled Plasmas Produced by 100-fs Laser Pulses." *Phys. Rev. Lett.* **80**(20) 4442 (1998).

[4] E. Springate, N. Hay, J. W. G. Tisch, M. B. Mason, T. Ditmire, M. H. R. Hutchinson, and J. P. Marangos. "Explosion of atomic clusters irradiated by high-intensity laser pulses: Scaling of ion energies with cluster and laser parameters." *Phys. Rev. A* **61** 063201 (2000).

[5] B. A. Remington. "High energy density laboratory astrophysics." *Plasma Physics and Controlled Fusion* **47** (2005).

[6] U. Saalmann, C. Siedschlag, and J.M. Rost. "Mechanisms of cluster ionization in strong laser pulses." *J. Phys. B* **39** (2006).

[7] G. E. Morfill, H. M. Thomas, U. Konopka, and M. Zuzic. "The plasma condensation: Liquid and crystalline plasmas." *Phys. Plasmas* **6**(5) 1769 (1999).

[8] C. Hollenstein. "Review article: The physics and chemistry of dusty plasmas." *Plasma Physics and Controlled Fusion* **42** 93 (2000).

[9] T. B. Mitchell, J. J. Bollinger, X. -P. Huang, W. M. Itano, and D. H. E. Dubin. "Direct observations of the structural phases of crystallized ion plasmas." *Phys. Plasmas* **6**(5) 1751 (1999).

[10] T. C. Killian, S. Kulin, S. D. Bergeson, L. A. Orozco, C. Orzel, and S. L. Rolston. "Creation of an Ultracold Neutral Plasma." *Phys. Rev. Lett.* **83**(23) 4776 (1999).

[11] C. E. Simien, Y. C. Chen, P. Gupta, S. Laha, Y. N. Martinez, P. G. Mickelson, S. B. Nagel, and T. C. Killian. "Using Absorption Imaging to Study Ion Dynamics in an Ultracold Neutral Plasma." *Phys. Rev. Lett.* **92**(14) 143001 (2004).

[12] Y. C. Chen, C. E. Simien, S. Laha, P. Gupta, Y. N. Martinez, P. G. Mickelson, S. B. Nagel, and T. C. Killian. "Electron screening and kinetic energy oscillations in a strongly coupled plasma." *Phys. Rev. Lett.* **93** 265003 (2004).

[13] E. A. Cummings, J. E. Daily, D. S. Durfee, and S. D. Bergeson. "Ultracold neutral plasma expansion in two dimensions." *Phys. Plasmas* **12** 123501 (2005).

[14] E. A. Cummings, J. E. Daily, D. S. Durfee, and S. D. Bergeson. "Fluorescence measurements of expanding strongly-coupled neutral plasmas." *Phys. Rev. Lett* **95** 235001 (2005).

[15] M. P. Robinson, B. L. Tolra, M. W. Noel, T. F. Gallagher, and P. Pillet. "Spon-

taneous Evolution of Rydberg Atoms into an Ultracold Plasma." *Phys. Rev. Lett.* **85**(21) 4466 (2000).

[16] D. Feldbaum, N. V. Morrow, S. K. Dutta, and G. Raithel. "Coulomb Expansion of Laser-Excited Ion Plasmas." *Phys. Rev. Lett.* **89** 173004 (2004).

[17] S. D. Bergeson and R. L Spencer. "Neutral-plasma oscillations at zero temperature." *Phys. Rev. E* **67** 026414 (2003).

[18] S. Kulin, T. C. Killian, S. D. Bergeson, and S. L. Rolston. "Plasma Oscillations and Expansion of an Ultracold Neutral Plasma." *Phys. Rev. Lett.* **85**(2) 318 (2000).

[19] J. L. Roberts, C. D. Fertig, M. J. Lim, , and S. L. Rolston. "Electron Temperature of Ultracold Plasmas." *Phys. Rev. Lett.* **92** 253003 (2004).

[20] W. Li, M. W. Noel, M. P. Robinson, P. J. Tanner, T. F. Gallagher, D. Comparat, B. Laburthe Tolra, N. Vanhaecke, T. Vogt, N. Zahzam, P. Pillet, and D. A. Tate. "Evolution dynamics of a dense frozen Rydberg gas to plasma." *Phys. Rev. A* **70** 042713 (2004).

[21] Nicolas Vanhaecke, Daniel Comparat, Duncan A. Tate, and Pierre Pillet. "Ionization of Rydberg atoms embedded in an ultracold plasma." *Phys. Rev. A* **71** 013416 (2005).

[22] W. Li, P. J. Tanner, and T. F. Gallagher. "Dipole-dipole excitation and ionization in an ultracold gas of Rydberg atoms." *Phys. Rev. Lett.* **94** 173001 (2005).

[23] M. S. Murillo. "Using Fermi Statistics to Create Strongly Coupled Ion Plasmas in Atom Traps." *Phys. Rev. Lett.* **87**(11) 115003 (2001).

[24] D. O. Gericke and M. S. Murillo. "Disorder-induced heating of ultracold plasmas." *Contrib. Plasma Phys.* **43** 298 (2003).

[25] T. Pohl, T. Pattard, and J. M. Rost. "Infuence of electron-ion collisions on Coulomb crystallization of ultracold neutral plasmas." *J. Phys. B* **38** (2005).

[26] F. Robicheaux and J. D. Hanson. "Simulated Expansion of an ultra-cold, neutral plasma." *Phys. Plasmas* **10**(6) 2217 (2003).

[27] F. Robicheaux and J. D. Hanson. "Simulation of the Expansion of an Ultracold Neutral Plasma." *Phys. Rev. Lett.* **88**(5) 55002 (2002).

[28] S. G. Kuzmin and T. M. O'Neil. "Numerical Simulation of Ultracold Plasmas: How Rapid Intrinsic Heating Limits the Development of Correlation." *Phys. Rev. Lett.* **88**(6) 65003 (2002).

[29] T. Pohl and T. Pattard. "Strong-coupling effects in the relaxation dynamics of ultracold neutral plasmas." *J. Phys.: Conf. Ser.* **11** 223 (2005).

[30] Y. Hahn. "Relaxation of cold plasmas and threshold lowering effect." *Phys. Lett. E* **64** 046409 (2001).

[31] T. Pohl, T. Pattard, and J. M. Rost. "Relaxation to non-equilibrium in expanding ultrcold neutral plasmas." *Phys. Rev. Lett.* **94** 205003 (2005).

[32] S. G. Kuzmin and T. M. O'Neil. "Numerical Simulation of Ultracold Plasmas." *Phys. Plasmas* **9**(9) 3743 (2002).

[33] S. Mazevet, L. A. Collins, and J. D. Kress. "Evolution of Ultracold Neutral Plasmas." *Phys. Rev. Lett.* **88**(5) 55001 (2002).

[34] T. Pohl, T. Pattard, and J. M. Rost. "Plasma formation from ultracold rydberg gases." *Phys. Rev. A* **68** 010703 (2003).

[35] E. L. Clark, K. Krushelnick, M. Zepf, F. N. Beg, M. Tatarakis, A. Machacek, M. I. K. Santala, I. Watts, P. A. Norreys, and A. E. Dangor. "Energetic Heavy-Ion and Proton Generation from Ultraintense Laser-Plasma Interactions with Solids." *Phys. Rev. Lett.* **85**(8) 1654 (2000).

[36] R. A. Snavely, M. H. Key, S. P. Hatchett, T. E. Cowan, M. Roth, T. W. Phillips, M. A. Stoyer, E. A. Henry, T. C. Sangster, M. S. Singh, S. C. Wilks, A. MacKinnon, A. Offenberger, D. M. Pennington, K. Yasuike, A. B. Langdon, B. F. Lasinski, J. Johnson, M. D. Perry, and E. M. Campbell. "Intense High-Energy Proton Beams from Petawatt-Laser Irradiation of Solids." *Phys. Rev. Lett.* **85**(14) 2945–2948 (2000).

[37] S. P. Hatchett, C. G. Brown, T. E. Cowan, E. A. Henry, J. S. Johnson, M. H. Key, J. A. Koch, A. B. Langdon, B. F. Lasinski, R. W. Lee, A. J. Mackinnon, D. M. Pennington, M. D. Perry, T. W. Phillips, M. Roth, T. C. Sangster, M. S. Singh, R. A. Snavely, M. A. Stoyer, S. C. Wilks, and K. Yasuike. "Electron,

photon, and ion beams from the relativistic interaction of Petawatt laser pulses with solid targets." . volume 7, page 2076. AIP (2000).

[38] A. Maksimchuk, S. Gu, K. Flippo, D. Umstadter, and V. Yu. Bychenkov. "Forward Ion Acceleration in Thin Films Driven by a High-Intensity Laser." *Phys. Rev. Lett.* **84**(18) 4108 (2000).

[39] J. Badziak, E. Woryna, P. Parys, K. Yu. Platonov, S. Jabłoński, L. Ryć, A. B. Vankov, and J. Wołowski. "Fast Proton Generation from Ultrashort Laser Pulse Interaction with Double-Layer Foil Targets." *Phys. Rev. Lett.* **87**(21) 215001 (2001).

[40] A. J. Mackinnon, Y. Sentoku, P. K. Patel, D. W. Price, S. Hatchett, M. H. Key, C. Andersen, R. Snavely, and R. R. Freeman. "Enhancement of Proton Acceleration by Hot-Electron Recirculation in Thin Foils Irradiated by Ultraintense Laser Pulses." *Phys. Rev. Lett.* **88**(21) 215006 (2002).

[41] M. Hegelich, S. Karsch, G. Pretzler, D. Habs, K. Witte, W. Guenther, M. Allen, A. Blazevic, J. Fuchs, J. C. Gauthier, M. Geissel, P. Audebert, T. Cowan, and M. Roth. "MeV Ion Jets from Short-Pulse-Laser Interaction with Thin Foils." *Phys. Rev. Lett.* **89**(8) 085002 (2002).

[42] M. Allen, Y. Sentoku, P. Audebert, A. Blazevic, T. Cowan, J. Fuchs, J. C. Gauthie, M. Geissel, M. Hegelich, S. Karsch, E. Morse, P. K. Patel, and M. Roth.

"Proton spectra from ultraintense laserplasma interaction with thin foils: Experiments, theory, and simulation." *Phys. Plasmas* **10** 3283 (2003).

[43] M. Kaluza, J. Schreiber, M. I. K. Santala, G. D. Tsakiris, K. Eidmann, J. Meyer-Ter-Vehn, and K. J. Witte. "Influence of the Laser Prepulse on Proton acceleration in thin-foil experiments." *Phys. Rev. Lett.* **93**(4) 045003 (2004).

[44] J. Fuchs, Y. Sentoku, S. Karsch, J. Cobble, P. Audebert, A. Kemp, A. Nikroo, P. Antici, E. Brambrink, A. Blazevic, E. M. Campbell, J. C. Fernndez, J.C. Gauthier, M. Geissel, M. Hegelich, H. Ppin, H. Popescu, N. Renard-LeGalloudec, M. Roth, J. Schreiber, R. Stephens, , and T. E. Cowan. "Comparison of Laser Ion Acceleration from the Front and Rear Surfaces of Thin Foils." *Phys. Rev. Lett.* **94** 045004 (2005).

[45] L. Romagnani, J. Fuchs, M. Borghesi, P. Antici, P. Audebert, F. Ceccherini, T. Cowan, T. Grismayer, S. Kar, A. Macchi, P. Mora, G. Pretzler, A. Schiavi, T. Toncian, and O. Willi. "Dynamics of Electric Fields Driving the Laser Acceleration of Multi-MeV Protons." *Phys. Rev. Lett.* **95** 195001 (2005).

[46] T. Ditmire, J. W. G. Tisch, E. Springate, M. B. Mason, N. Hay, R. A. Smith, J. Marangos, and M. H. R. Hutchinson. "High-energy ions produced in explosions of superheated atomic clusters." *Nature* **386** 54 (1997).

[47] G. S. Sarkisov, V. Yu. Bychenkov, V. N. Novikov, V. T. Tikhonchuk, A. Maksimchuk, S.-Y. Chen, R. Wagner, G. Mourou, and D. Umstadter. "Self-focusing,

channel formation, and high-energy ion generation in interaction of an intense short laser pulse with a He jet." *Phys. Rev. E* **59**(6) 7042 (1999).

[48] K. Krushelnick, E. L. Clark, Z. Najmudin, M. Salvati, M. I. K. Santala, M. Tatarakis, A. E. Dangor, V. Malka, D. Neely, R. Allott, and C. Danson. "Multi-MeV Ion Production from High-Intensity Laser Interactions with Underdense Plasmas." *Phys. Rev. Lett.* **83**(4) 737 (1999).

[49] H. J. Metcalf and P. van der Straten. *Laser Cooling and Trapping.* Springer-Verlag New York, New York (1999).

[50] S. B. Nagel, C. E. Simien, S. Laha, P. Gupta, V. S. Ashoka, and T. C. Killian. "Magnetic Trapping of Metastable $^3P_2$ Atomic Strontium." *Phys. Rev. A* **67** 011401 (2003).

[51] Priya Gupta. *Pulsed Dye Laser For Excitation Of Strontium.* Master's Thesis, Rice University (2004).

[52] W. Mende, K. Bartschat, and M. Koch. "Near-threshold photoionization from the Sr I (5s5p) $^1\mathrm{Po}_1$ state." *J. Phys. B: At. Mol. Opt. Phys.* **28**(12) 2385 (1995).

[53] T. Amthor, M. Reetz-Lamour, S. Westermann, J. Denskat, and M. Weidemller. "Mechanical Effect of van der Waals Interactions Observed in Real Time in an Ultracold Rydberg Gas." *Phys. Rev. Lett.* **98** 023004 (2007).

[54] Sampad Laha. "Collective modes in strongly coupled plasmas." .

[55] S. Hamaguchi, R. T. Farouki, and D. H. E. Dubin. "Thermodynamics of stronlgy-coupled Yukawa systems near the one-component-plasma limit. I. Derivation of excess energy." *J. Chem. Phys.* **101**(11) 9876 (1994).

[56] T. Pohl, T. Pattard, and J. M. Rost. "Kinetic modeling and molecular dynamics simulation of ultracold neutral plasmas including ionic correlations." *Phys. Rev. A* **70**(3) 033416 (2004).

[57] R. T. Farouki and S. Hamaguchi. "Thermodynamics of strongly-coupled Yukawa systems near the one-component-plasma limit. II. Molecular dynamics simultations." *J. Chem. Phys.* **101**(11) 9885 (1994).

[58] J. C. Stewart and K. D. Pyatt. "Lowering of Ionization Potentials in Plasmas." *Astrophys. J.* **144** 1203 (1966).

[59] Y. Hahn. "Threshold lowering effects on an expanding cold plasma." *Phys. Lett. A* **293** 266 (2002).

[60] J. P. Hansen. "Statistical Mechanics of Dense Ionized Matter. I. Equilibrium Properties of the Classical One-Component Plasma." *Phys. Rev. A* **8** 3096 (1973).

[61] Thomas Pohl, (2007).

[62] G. Schmidt. *Physics of High Temperature Plasmas.* Academic Press, New York (1979).

[63] W. Graham, W. Fritsch, Y. Hahn, and J. A. Tanis, Editors. *NATO ASI Series B: Physics, Recombination of Atomic Ions*, volume 296. Plenum, New York (1992).

[64] M. J. Seaton. "Radiative Recombination of Hydrogenic Ions." *Mon. Not. R. Astron. Soc.* **119** 81 (1959).

[65] P. Mansbach and J. Keck. "Monte Carlo trajectory calculations of atomic excitation and ionization by thermal electrons." *Phys. Rev.* **181** 275 (1969).

[66] T. C. Killian, M. J. Lim, S. Kulin, R. Dumke, S. D. Bergeson, and S. L. Rolston. "Formation of Rydberg Atoms in an Expanding Ultracold Neutral Plasma." *Phys. Rev. Lett.* **86**(17) 3759 (2001).

[67] Y. Hahn. "Plasma density effects on the three-body recombination rate coefficients." *Phys. Lett. A* **231** 82 (1997).

[68] Jr. L. Spitzer. *Physics of Fully Ionized Gases.* Wiley, New York (1962).

[69] A. V. Gurevich, L. V. Pariskaya, and L. P. Pitaievskii. "Self-similar Motion of Rarefied Plasma." *Sov. Phys. JETP* **22** 449 (1966).

[70] A. V. Baitin and K. M. Kuzanyan. "A self-similar solution for expansion into a vacuum of a collisionless plasma bunch." *J. Plasma Phys.* **59**(1) 83 (1998).

[71] D. S. Dorozhkina and V. E. Semenov. "Exact solution of Vlasov equations for quasineutral expansion of plasma bunch into vacuum." *Phys. Rev. Lett.* **81**(13) 2691 (1998).

[72] P. Mora. "Collisionless expansion of a Gaussian plasma into a vacuum." *Phys. Plasmas* **12**(11) 112102 (2005).

[73] T. C. Killian, T. Pattard, T. Pohl, and J. M. Rost. "Ultracold Neutral Plasmas." *arXiv:physics/0612097* (2006).

[74] T. C. Killian, Y. C. Chen, P. Gupta, S. Laha, Y. N. Martinez, P. G. Mickelson, S. B. Nagel, A. D. Saenz, and C. E. Simien. "Absorption Imaging and Spectroscopy of Ultracold Neutral Plasmas." *J. Phys. B* **38** 351 (2005).

[75] Masaharu Mitsunaga, Makoto Yamashita, and Hironobu Inoue. "Absorption imaging of electromagnetically induced transparency in cold sodium atoms." *Phys. Rev. A* **62** 013817 (2000).

[76] A. E. Siegman. *Lasers.* University Science Books, Sausolito, California (1986).

[77] S. Laha, Y.C. Chen, P. Gupta, C.E. Simien, Y.N. Martinez, P.G. Mickelson, S.B. Nagel, and T.C. Killian. "Kinetic energy oscillations in annular regions of ultracold neutral plasmas." *Euro. Phys. J. D, in press.* **40** 51 (2006).

[78] M. T. Frey, X. Ling, B. G. Lindsay, K. A. Smith, and F. B. Dunning. "Use of the Stark effect to minimize residual electric fields in an experimental volume." *Rev. Sci. Instr.* **64** 3649 (1993).

[79] Ch. Sack and H. Schamel. "Plasma expansion into vacuum - A Hydrodynamic approach." *Phys. Rep.* **156** 311 (1987).

[80] V. F. Kovalev and V. Yu. Bychenkov. "Analytic Solutions to the Vlasov Equations for Expanding Plasmas." *Phys. Rev. Lett.* **90**(18) 185004 (2003).

[81] T. Grismayer and P. Mora. "Influence of a finite initial ion density gradient on plasma expansion into a vacuum." *Phys. Plasmas* **13**(3) 032103 (2006).

[82] A. N. Tkachev and S. I. Yakovlenko. "Relaxation of Rydberg states in an ultracold plasma." *Quantum Electronics* **31**(12) 1084 (2001).

[83] A. N. Tkachev and S. I. Yakovlenko. "Moderation of recombination in an ultracold laser-produced plasma." *Quantum Electronics* **30**(12) 1077 (2000).

[84] F. F. Chen. "Introduction to Plasma Physics." (1974).

[85] P. Esherick. "Bound, even-parity J=0 and J=2 spectra of Sr." *Phys. Rev. A* **15** 1920 (1977).